MEASUREMENT OF THE $Z/\gamma^*(\rightarrow e^+e^-)+\geq n$ JET PRODUCTION CROSS SECTIONS IN $\mathbf{p\bar{p}}$ COLLISIONS AT $\sqrt{\mathbf{s}} = \mathbf{1.96}$ TeV

BY

MARC BUEHLER
B.S. (University of Basel, Switzerland) 1992
M.S. (University of Heidelberg, Germany) 1997

THESIS

Submitted in partial fulfillment of the requirements
for the degree of Doctor of Philosophy in Physics
in the Graduate College of the
University of Illinois at Chicago, 2005

Chicago, Illinois

To Dasha

ACKNOWLEDGMENTS

First, I wish to thank my thesis advisor Nikos Varelas who guided and supported me throughout the years. Thanks to the other members of the UIC group at DØ - Mark Adams, Cecilia Gerber, and Elizaveta Shabalina - for their assistance. Special thanks to Alan Stone for his help.

I am also indebted to many people in the Higgs Group at DØ ; to the Higgs group conveners Gregorio Bernardi, and Avto Kharchilava; to Kazu Hanagaki who taught me to never surrender; to Jodi Wittlin who tried to convince me that Higgs bosons are red. I would especially like to thank Suyong Choi for his help and advice.

I was lucky to work on the trigger system alongside Adam, Burair, Josh K., Miroslav, and Terry T.

Of course, this work would not have been possible without the help and support from the hard working DØ Collaboration (see Appendix A).

On a more personal note, I would like to thank the friends who kept me sane over the course of these years; Reinhard, the fastest postdoc at DØ , and Bob H. who showed me the artsy side of Chicago; Juan and Kyle for being such good friends; Paul and Randal for stimulating discussions about particle physics and beyond; Aneta and Richard for helping me find my way through the jungle of UIC thesis regulations; and Jui for her perfect assistance as UIC graduate adviser.

I could not have survived without support from the UIC “gang”. Thanks Gustavo, James,

ACKNOWLEDGMENTS (Continued)

and Tim for some unforgettable moments. Special thanks to Mario for introducing me to the insanely fine art of Espresso.

Mom and Dad, thank you for your patience and support while I was pursuing my studies far away from home. Thanks to Anja for being a great sister.

Finally, I would like to thank Dasha for her love. This dissertation would not have been possible without her encouragement.

MB

TABLE OF CONTENTS

TABLE OF CONTENTS (Continued)

CHAPTER **PAGE**

TABLE OF CONTENTS (Continued)

CHAPTER **PAGE**

LIST OF TABLES

TABLE **PAGE**

LIST OF TABLES (Continued)

TABLE **PAGE**

LIST OF TABLES (Continued)

LIST OF FIGURES

LIST OF FIGURES (Continued)

LIST OF FIGURES (Continued)

FIGURE **PAGE**

LIST OF FIGURES (Continued)

LIST OF FIGURES (Continued)

FIGURE **PAGE**

LIST OF FIGURES (Continued)

LIST OF FIGURES (Continued)

LIST OF FIGURES (Continued)

FIGURE **PAGE**

LIST OF ABBREVIATIONS

AA	Alternative Algorithm
BR	Branching Ratio
CC	Central Calorimeter
CellNN	Cell Nearest Neighbor
CDF	Collider Detector at Fermilab
CERN	European Organization for Nuclear Research
CFT	Central Fiber Tracker
CH(F)	Coarse Hadronic (Fraction)
CIA	Control, Input/Output, Address
CKKW	Catani, Krauss, Kuhn, Webber
COOR	Central Coordination Process
CPLD	Complex Programmable Logic Device
CPS	Central Preshower
CPU	Central Processing Unit
CTEQ	Coordinated Theoretical-Experimental Project on QCD

LIST OF ABBREVIATIONS (Continued)

D0GSTAR	D0 GEANT Simulation of the Total Apparatus Response
DAQ	Data Acquisition
DEC	Digital Equipment Corporation
DGLAP	Dokshitzer-Gribov-Lipatov-Altarelli-Parisi
DIS	Deep Inelastic Scattering
DMA	Direct Memory Access
DPM	Dual Port Memory
DRAM	Dynamic Random Access Memory
DSW	Data SWitch
EC	End Calorimeter
EM	Electro Magnetic
EMF	Electro Magnetic Fraction
FAMUS	Forward Angle Muon System
FIC	Fiber Input Converter
FH	Fine Hadronic
FIFO	First In, First Out
FNAL	Fermi National Accelerator Laboratory
FPGA	Field Programmable Gate Array

LIST OF ABBREVIATIONS (Continued)

FPS	Forward PreShower
FSR	Final State Radiation
GEANT	GEometry ANd Tracking
GWS	Glashow, Weinberg, Salam
HotF	Hot Fraction
HTF	Histogramming Track Finder
ICD	Inter Cryostat Detector
ICR	Inter Cryostat Region
ISR	Initial State Radiation
IDE	Integrated Drive Electronics
I/O	Input/Output
ISA	Industry Standard Architecture
JES	Jet Energy Scale
L1	Level 1
L1Cal	Level 1 Calorimeter
L1CTT	Level 1 Central Track Trigger
L1Muon	Level 1 Muon
L2	Level 2

LIST OF ABBREVIATIONS (Continued)

L2Cal	Level 2 Calorimeter
L2CTT	Level 2 Central Track Trigger
L2GBL	Level 2 Global
L2MUC	Level 2 Muon Central
L2MUF	Level 2 Muon Forward
L2Muon	Level 2 Muon
L2PS	Level 2 PreShower
L2STT	Level 2 Silicon Track Trigger
L3	Level 3
L3DAQ	Level 3 Data Acquisition
LBN	Luminosity Block Number
Linac	Linear Accelerator
LL	Leading Logarithmic
LLA	Leading Log Approximation
MB	Minimum Bias
MBT	Magic Bus Transceiver
MBus	Magic Bus
MC	Monte Carlo

LIST OF ABBREVIATIONS (Continued)

MCFM	Monte Carlo for FeMtobarn processes
MDT	Mini Drift Tube
MG	Massless Gap
NLO	Next-to-Leading Order
PCI	Peripheral Component Interconnect
PDF	Parton Distribution Function
PDT	Proportional Drift Tube
PIO	Programmed Input Output
PLD	Programmable Logic Device
PV	Primary Vertex
RF	Radio Frequency
RISC	Reduced Instruction Set Computing
ROM	Read Only Memory
QCD	Quantum Chromo Dynamics
QED	Quantum Electro Dynamics
QFT	Quantum Field Theory
SBC	Single Board Computer
SCL(init)	Serial Command Link (Initialize)

LIST OF ABBREVIATIONS (Continued)

Scone	Simple Cone
SIMM	Single In-line Memory Module
SLIC	Second Level Input Computer
SM	Standard Model
SMT	Silicon Microstrip Tracker
SROM	Serial Read Only Memory
TCC	Trigger Control Computer
TDR	Technical Design Report
TFW	Trigger FrameWork
TOT	Total Energy
VBD	VME Buffer Driver
VITA	VMEbus International Trade Association
VLPC	Visible Light Photon Counter
VME	VERSA Module Eurocard
WAMUS	Wide Angle Muon System

SUMMARY

A study of events with Z/γ^* bosons and hadronic jets produced at the Tevatron in $p\bar{p}$ collisions at a center of mass energy of 1.96 TeV is presented. The data consist of approximately 14,000 $Z/\gamma^* \rightarrow e^+e^-$ decay candidates from 343 pb^{-1} of integrated luminosity collected with the DØ detector. Cross sections and jet production properties have been measured for $Z/\gamma^* + \geq 0$ to 5 jet events. This measurement represents a significant improvement over previous measurements at the Tevatron, and it is the first at this center of mass energy with the DØ detector. The results are in good agreement with QCD predictions.

CHAPTER 1

INTRODUCTION

Since the discovery of the Z boson by the European Organization for Nuclear Research (CERN) in 1983 (1; 2), the study of electroweak gauge bosons in association with jets has been of increasing importance. The measurement of the $Z+\geq n$ jet cross sections at Tevatron energies is important for studying perturbative quantum chromodynamics (QCD) calculations and exploring untested regions of phase space with low background final states. Furthermore, the associated production of Z bosons with jets is a major background to many interesting physics processes. In particular, searches in the channel where a Higgs boson is being produced in association with a Z boson rely on a detailed understanding of $Z + 2$ jet production.

Chapter 2 of this dissertation provides a short overview of the theoretical framework within which this analysis was performed. A description of the experimental apparatus, including the Fermilab chain of accelerators, and the DØ detector with its data acquisition system is given in Chapters 3 and 4. Chapter 5 describes the methods to reconstruct physics objects from raw detector data. The Monte Carlo (MC) event generators are illustrated in Chapter 6. Data and MC samples, including comparisons between data and MC, are described in Chapter 7. Chapters 8 and 9 outline all steps that lead to the measurements of the inclusive $Z/\gamma^*(\rightarrow e^+e^-)$ and $Z/\gamma^*(\rightarrow e^+e^-)+\geq n$ jet cross sections. Sources for systematic uncertainties are discussed in Chapter 10. A summary of the results is presented in Chapter 11.

Throughout this dissertation (unless stated otherwise), $\hbar = c = 1$ is used.

CHAPTER 2

THEORY

2.1 The Standard Model

The *Standard Model* (SM) of Particle Physics is the current theory of elementary particles along with the interactions that act between them (except gravity). The SM is a quantum theory of fields (QFT), which arises from combining quantum mechanics with special relativity. The SM includes most of the current understanding of the laws of physics, and has been verified experimentally to a high level of accuracy.

Nevertheless, the theory is incomplete. The SM contains many free parameters that cannot be derived from first principles. The Higgs boson, which is considered to be the last remaining piece to the SM, has not been experimentally detected yet. Furthermore, gravity is not included in the SM.

The following sections give an overview of the SM (3; 4; 5; 6; 7; 8).

2.1.1 Quarks and Leptons

In the SM the fundamental particles that make up ordinary matter are divided into two groups: *quarks* and *leptons* (Figure 1). Both quarks and leptons are *fermions* since they are spin-$\frac{1}{2}$ particles, and therefore obey Fermi-Dirac statistics. As indicated in Figure 1, quarks and leptons are each arranged in three generations, containing particles of similar properties but differing in mass. For each particle there exists an associated anti-particle.

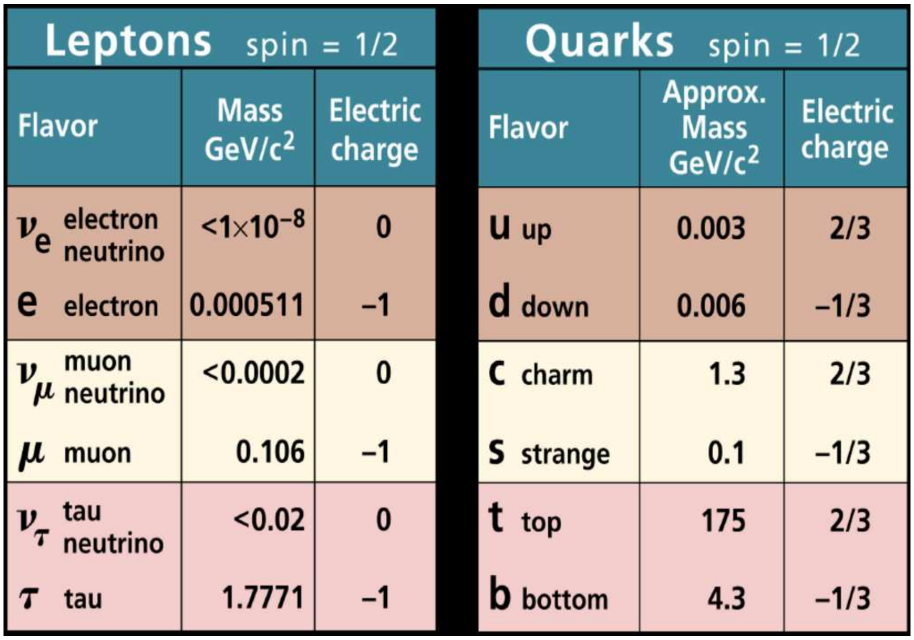

Leptons spin = 1/2

Flavor		Mass GeV/c^2	Electric charge
ν_e	electron neutrino	<1×10^{-8}	0
e	electron	0.000511	–1
ν_μ	muon neutrino	<0.0002	0
μ	muon	0.106	–1
ν_τ	tau neutrino	<0.02	0
τ	tau	1.7771	–1

Quarks spin = 1/2

Flavor		Approx. Mass GeV/c^2	Electric charge
u	up	0.003	2/3
d	down	0.006	–1/3
c	charm	1.3	2/3
s	strange	0.1	–1/3
t	top	175	2/3
b	bottom	4.3	–1/3

Figure 1. Properties of fermion particles: quarks and leptons. Spin is given in units of $\hbar$, electric charge is given in units of the absolute value of the electron charge.

There are six different flavors of quarks, labeled (in order of increasing mass) *up*, *down*, *strange*, *charm*, *bottom*, and *top*. Quarks are never observed as single particles (see Chapter 2.1.2.3), and they carry fractional electrical charges[1] of $+\frac{2}{3}$ or -$\frac{1}{3}$. Quarks form bound states called *hadrons* by either combining three quarks into *baryons*, or by pairing a quark with an antiquark into *mesons*. Protons (made up of two up-quarks and one down-quark) and neutrons (made up of two down-quarks and one up-quark) are the most common examples of baryons.

---

[1] All charges are given in units of the absolute value of the electron charge, 1.602×10^{-19} Coulombs.

Pions ($\pi^{0,\pm}$) and Kaons ($K^{\pm}$, K^0, $\bar{K}^0$) are the most common types of mesons.

There are three different flavors of charged leptons carrying a charge of -1: *electron* (e^-), *muon* (μ^-), and *tau* (τ^-). While electrons exist in all atoms, muons and taus can only be observed in energetic processes like cosmic ray showers, or in high energy particle collisions. There are three neutral leptons, called *neutrinos* (ν), each corresponding to a charged lepton: ν_e, ν_μ, and ν_τ. Neutrinos interact extraordinarily weakly with matter, and their masses are negligibly small.

2.1.2 Interactions

One of the most fundamental insights in theoretical physics is that interactions are dictated by symmetry principles. In QFT, interactions manifest themselves by imposing symmetry conditions on the quantum fields representing the respective interactions. Using the framework of Lagrangian field theory, the Lagrangian of the theory is required to be invariant under a group of local phase changes (*local gauge invariance*). A local phase depends on space and time in a completely arbitrary way. In order to ensure gauge invariance of such a Lagrangian, gauge fields are introduced. These gauge fields lead to spin-1 bosons that are the mediators of the interactions (except gravity).

Four types of interactions are currently known (in order of decreasing strength): strong, electromagnetic, weak, and gravitational. Figure 2 summarizes the basic properties of the four interactions. The following is a brief summary of the interactions that have been incorporated into the SM.

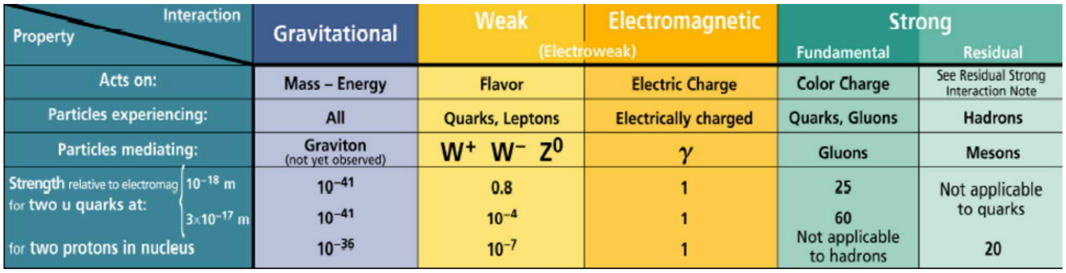

Interaction / Property	Gravitational	Weak	Electromagnetic	Strong	
		(Electroweak)		Fundamental	Residual
Acts on:	Mass – Energy	Flavor	Electric Charge	Color Charge	See Residual Strong Interaction Note
Particles experiencing:	All	Quarks, Leptons	Electrically charged	Quarks, Gluons	Hadrons
Particles mediating:	Graviton (not yet observed)	W^+ W^- Z^0	γ	Gluons	Mesons
Strength relative to electromag for two u quarks at: 10^{-18} m	10^{-41}	0.8	1	25	Not applicable to quarks
3×10^{-17} m	10^{-41}	10^{-4}	1	60	
for two protons in nucleus	10^{-36}	10^{-7}	1	Not applicable to hadrons	20

Figure 2. Fundamental forces and their properties.

2.1.2.1 Electromagnetic Interaction

Historically, the electromagnetic interaction was the first to be formulated in the framework of a calculable (*renormalizable*) QFT by Tomonaga, Feynman, and Schwinger in the 1940s (Nobel Prize in 1965). *Quantum Electrodynamics* (QED) describes the electromagnetic interaction by requiring gauge invariance under U(1) group transformations. U(1) denotes a group of unitary one-dimensional matrices, describing space-time dependent rotations in a complex plane. The requirement of gauge invariance gives rise to the photon field and the *photons* as the corresponding mediator of the electromagnetic interaction. Because the photon is massless the interaction has infinite range. The photon couples to all particles that carry electrical charge, like quarks and charged leptons. The strength of the interaction is proportional to the magnitude of the dimensionless *fine structure coupling constant*:

$$\alpha_{EM} = \frac{e^2}{4\pi} \approx \frac{1}{137}. \tag{2.1}$$

2.1.2.2 Weak Interaction

The weak interaction is most prominent in *beta decays* and associated radioactivity:

$$n \rightarrow p + e^- + \bar{\nu}_e \tag{2.2}$$

$$p \rightarrow n + e^+ + \nu_e. \tag{2.3}$$

The range of the interaction is short due to the high mass of the mediating gauge bosons ($W^\pm$, Z^0) (9):

$$m_{W^\pm} = 80.425 \pm 0.038\ GeV \tag{2.4}$$

$$m_{Z^0} = 91.1876 \pm 0.0021\ GeV. \tag{2.5}$$

A QFT combining the electromagnetic with the weak interaction was first developed by Glashow, Weinberg, and Salam (*GWS theory*, Noble Prize in 1979). Later 't Hooft and Veltman were able to prove that the theory is renormalizable (Nobel Prize in 1999). Electroweak theory combines a U(1) group with an SU(2) group, and requires invariance under SU(2)⊗U(1) transformations. SU(n) describes groups of special[1] unitary $n \times n$ matrices. Local gauge invariance under SU(2) group transformations introduces three massless spin-1 gauge bosons W^+, W^-,

---

[1] The determinant of the matrices must be 1.

and W^0. Adding the U(1) group introduces another gauge boson called B^0. The W^0 and B^0 mix quantum mechanically to give rise to the experimentally observed photon (γ) and Z^0:

$$\gamma = W^0 \sin\theta_W + B^0 \cos\theta_W \tag{2.6}$$

$$Z^0 = W^0 \cos\theta_W - B^0 \sin\theta_W . \tag{2.7}$$

where θ_W is called the *weak mixing angle* or *Weinberg angle.* As opposed to QED, the underlying group of the electroweak theory is *non-Abelian* since not all the generators of the group commute with each other.

Up to this point the electroweak theory is very simple and elegant. Yet it is incomplete, since all particles of the theory are massless. Additionally, mass terms cannot be introduced into the Lagrangian describing the system, since this would destroy the local gauge invariance of the Lagrangian. This problem is resolved by the *Higgs mechanism*, which introduces *spontaneous symmetry breaking* of the Higgs scalar field potential, thereby giving mass to the gauge bosons (W and Z) and the quarks and leptons.

2.1.2.3 Strong Interaction

Quantum Chromo Dynamics (QCD) is the QFT describing the strong interaction. It is based on an SU(3) gauge field, which leads to 8 mediating massless gauge bosons called *gluons.* Quarks carry a new type of “charge” called *color.* Each (anti)quark can carry a (anti)red, (anti)green, or (anti)blue color charge. Gluons carry a combination of a color and anticolor charge. As carriers of the color charge, gluons can couple to each other. This derives from the non-Abelian character of the gauge theory. Quarks and gluons are collectively referred to as *partons*.

One interesting feature of QCD is that the strength of the strong coupling increases with decreasing energy scale, i.e. at low energies and long distances the interaction becomes too strong to be treated within the framework of perturbation theory. This leads to *confinement*, which assumes that all objects carrying color can never be found as free particles in nature and that they are confined into color-neutral composite hadrons. The quarks that combine into baryons or mesons are referred to as *valence quarks*, and they constantly interact with each other by exchanging gluons. Since gluons can couple to each other, they can emit more gluons that can further split into virtual quark-antiquark pairs called *sea quarks*.

Experimentally quarks and gluons are observed as *jets* of color-neutral hadrons. This means that if a single parton emerges from a particle collision, gluons will be radiated which subsequently produce quark-antiquark pairs to form a *parton shower*. Ultimately the partons combine into a jet of hadrons moving in the direction close to that of the original parton. This final step is called *hadronization*.

The strong coupling constant, α_s, can be expressed to leading-log[1] in Q^2 by:

$$\alpha_s(Q^2) = \frac{12\pi}{(11c - 2n_f)\log(\frac{Q^2}{\Lambda^2})}, \tag{2.8}$$

---

[1] The term "leading-log" is used to indicate an all-orders calculation in which only the leading logarithm terms are retained.

where Q expresses the magnitude of the momentum transferred in the interaction, n_f indicates the number of quark flavors (6 in the SM), and c is the number of quark colors (3 in the SM). Λ is the QCD scale parameter, defined as:

$$\Lambda^2 = \mu_R^2 \exp \frac{-12\pi}{(11c - 2n_f)\alpha_s(\mu_R^2)}. \tag{2.9}$$

The parameter μ_R introduces an arbitrary renormalization scale to regulate divergences in the perturbative calculation of α_s. Equation 2.8 shows that the strength of the strong coupling decreases with increasing momentum transfer Q^2. Therefore, quarks and gluons are *asymptotically free* when probed at high energies. Theoretical work on asymptotic freedom by Gross, Politzer, and Wilczek was rewarded with the 2004 Nobel Prize. On the other hand, as Q^2 approaches Λ, the coupling becomes large and perturbative calculations are no longer possible.

2.2 The Measurement of the $Z/\gamma^*(\rightarrow e^+e^-) + \geq n$ Jet Cross Sections

In QCD, at high energies and large momentum transfers, interactions between hadrons are due to the hard parton-level scattering (*hard-scattering*) of the hadron constituents (i.e., quarks and gluons). For example, in the case of $p\bar{p}$ collisions, the hard-scattering process can involve quark-antiquark scattering into a lepton pair, l^+l^- (Figure 3). The cross section for such a process is given in Equation 2.10. In general, cross sections represent an effective size of a "target" measured in units of area (1 barn = 10^{-24} cm^2), presented to a probe.

$$\sigma(p(P_1)+\bar{p}(P_2) \rightarrow l^+l^-)+X) = \int \mathrm{d}x_1 \int \mathrm{d}x_2 \sum_f f_{q/p}(x_1) f_{\bar{q}/\bar{p}}(x_2) \cdot \hat{\sigma}(q(x_1P_1)+\bar{q}(x_2P_2)) \rightarrow l^+l^-). \tag{2.10}$$

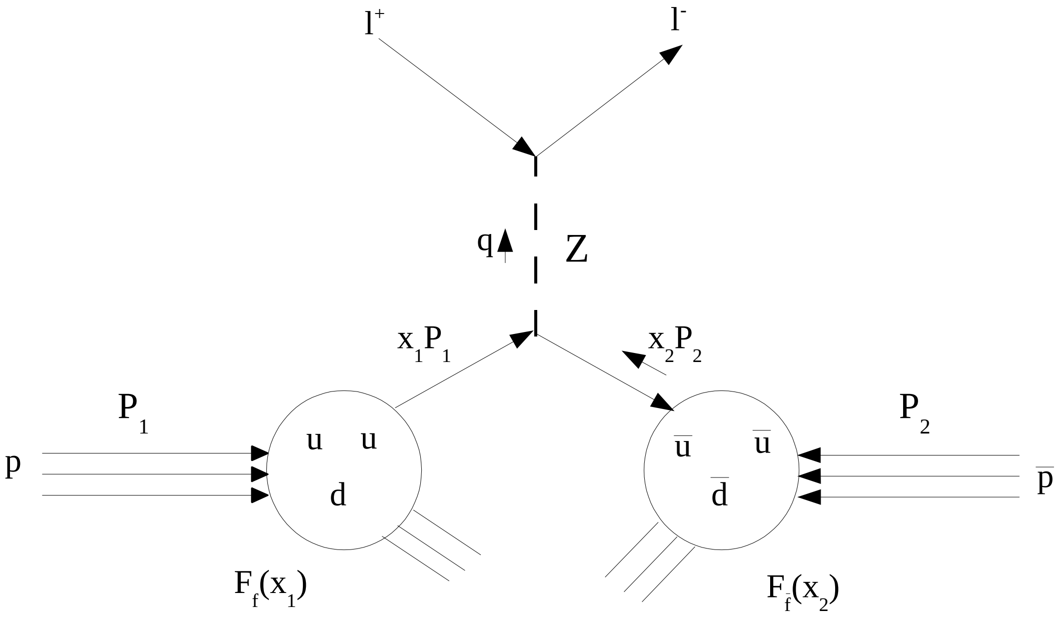

Figure 3. Schematic view of lepton pair production in $p\bar{p}$ collisions.

Here P_1 and P_2 are the proton (p) and anti-proton ($\bar{p}$) momentum, respectively. $f_{q/p}(x_1)$ and $f_{\bar{q}/\bar{p}}(x_2)$ are *parton distribution functions* (PDFs), which give the probability for a parton q ($\bar{q}$) to carry a fraction x_1 (x_2) of the proton's (antiproton's) total momentum. $\hat{\sigma}(q(x_1P_1) + \bar{q}(x_2P_2)) \rightarrow l^+l^-)$ is the hard-scattering *partonic cross section.* Equation 2.10 separates (*factorizes*) short distance effects, as described by the partonic cross section, from long distance effects, as described by the PDFs. The boundary between these two contributions is defined by the *factorization scale*, μ_F, which isolates non-perturbative cross section contributions from the calculable perturbative part[1].

The PDFs are specific to an initial hadron, i.e. a proton PDF is different from that of a pion. Since PDFs measure properties that cannot be calculated perturbatively, they can only be derived from experiments, based on measurements from *deep inelastic scattering* (DIS), direct photon, and $p\bar{p}$ experiments. PDFs depend on x and Q^2. Given a PDF at a specific momentum scale, the evolution to any other momentum scale can be determined with the *Dokshitzer-Gribov-Lipatov-Altarelli-Parisi* (DGLAP) equations (10; 11; 12). Since any given experiment can only cover a limited range of x and Q^2 values, results from different measurements are combined into *global QCD fits.* The PDFs used for this analysis are based on global fits provided by the CTEQ collaboration (Coordinated Theoretical-Experimental Project on QCD) (13).

Figure 4 depicts a graphical representation (*Feynman diagram*) of the hard scattering process for $q\bar{q} \to Z \to e^+e^-$. The leading order (LO) partonic cross section describing $q\bar{q} \to Z$ is:

$$\hat{\sigma}_{LO}(q\bar{q} \to Z) = \pi \frac{G_F}{\sqrt{2}}(1 - 4|Q_q|x_W + 8Q_q^2 x_W^2)M_Z^2 \delta(\hat{s} - M_Z^2), \tag{2.11}$$

---

[1] μ_R is the scale that enters α_s, μ_F enters the PDF, and Q is the hard scale of the interaction.

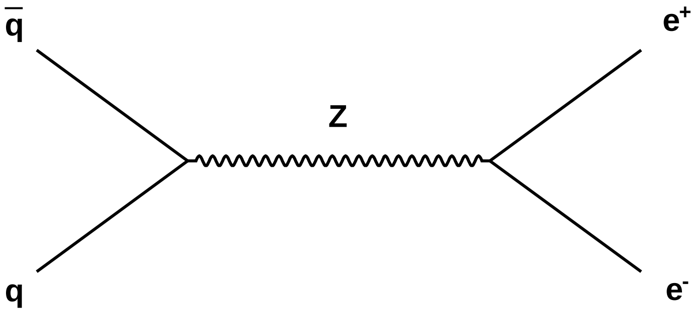

Figure 4. Feynman diagram for Z production via $q\bar{q} \to Z \to e^+e^-$.

where Q_q is the charge of the quark, and $x_W \equiv \sin^2\theta_W = 1 - M_W^2/M_Z^2$. G_F is the *Fermi Constant*, defined as $\frac{G_F}{\sqrt{2}} \equiv \frac{4\pi\alpha}{8M_W^2(1-M_W^2/M_Z^2)}$.

The *branching ratio* which gives the probability for $Z \to e^+e^-$ is:

$$BR(Z \to e^+e^-) = \frac{1 - 4\sin^2\theta_W + 8\sin^4\theta_W}{21 - 40\sin^2\theta_W + \frac{160}{3}\sin^4\theta_W} = 0.0344. \tag{2.12}$$

Combining Equation 2.11 and Equation 2.12 gives the full expression for the $\sigma(q\bar{q} \to Z \to e^+e^-)$ process.

Physical quantities in QCD are generally expressed as perturbative expansions in the strong coupling constant by separating processes at different orders of α_s. Figure 5 and Figure 6 show LO processes for Z/γ^* generation with an additional parton in the final state. The decay of the Z/γ^* gauge bosons into pairs of electrons (e^-) and positrons (e^+) provides an efficient way to identify the final state with low background contamination.

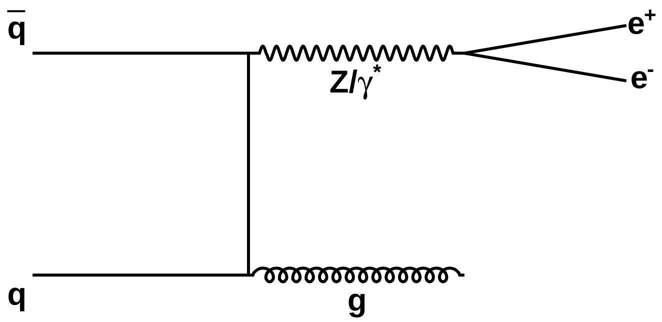

Figure 5. Feynman diagram for Z/γ^* production in association with a parton via $q\bar{q} \rightarrow Z/\gamma^* g$.

The production of Z/γ^* gauge bosons in association with jets provides a good opportunity to test perturbative QCD predictions at large momentum transfers. This analysis studies Z/γ^* gauge boson production and tests the reliability of perturbative QCD predictions over a range of jet energies and jet multiplicities. The results are compared to next-to-leading order (NLO) calculations and event simulations which include some higher order corrections to the leading-order (LO) processes.

This analysis also provides a contribution to the study of background processes that are relevant for Higgs boson searches (14; 15). One of the dominant Higgs production modes at the Tevatron involves the generation of a Higgs boson in association with a Z boson (Figure 7). The study of jet properties and cross sections for processes that generate similar final state particles (Figure 8) results in a more precise distinction between a possible Higgs signal and QCD background.

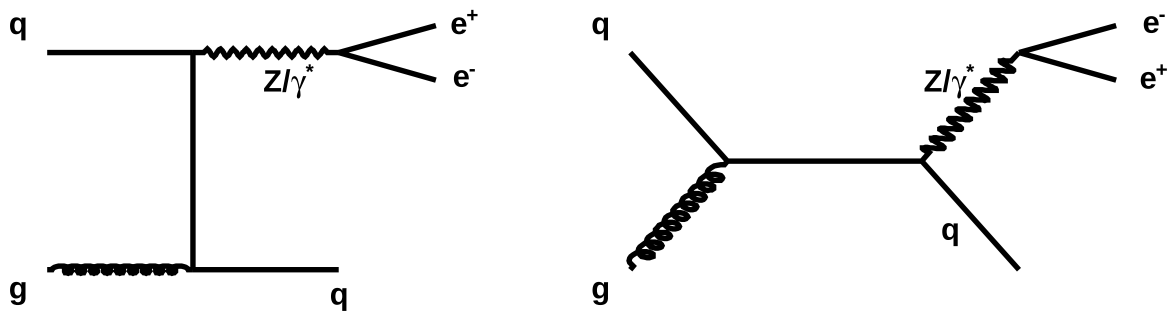

Figure 6. Feynman diagrams for Z/γ^* production in association with a parton via $qg \rightarrow Z/\gamma^* q$.

This measurement offers a significant improvement over earlier measurements at the Tevatron. The previous CDF measurement (16), performed at a center of mass energy of 1.8 TeV with ≈100 pb^{-1} of luminosity, only covered jet multiplicities up to four jets. The measurement presented in this analysis was performed at a higher center of mass energy (1.96 TeV), with ≈340 pb^{-1} of luminosity, and includes jet multiplicities up to five jets. This is the first measurement at this center of mass energy.

The analysis was performed with the DØ detector at the Fermilab proton-antiproton Tevatron collider. The following chapter gives an overview of the experimental apparatus that was used for this analysis.

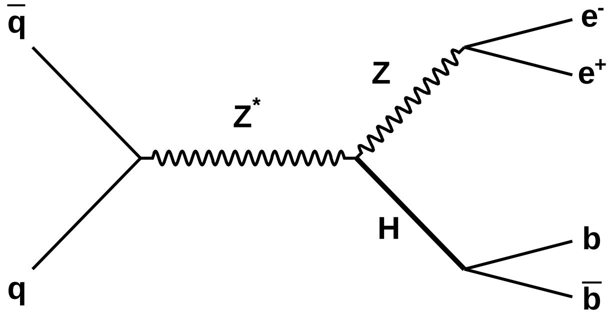

Figure 7. SM Higgs boson production in association with a Z boson via $q\bar{q} \rightarrow HZ$ (*Higgsstrahlung*).

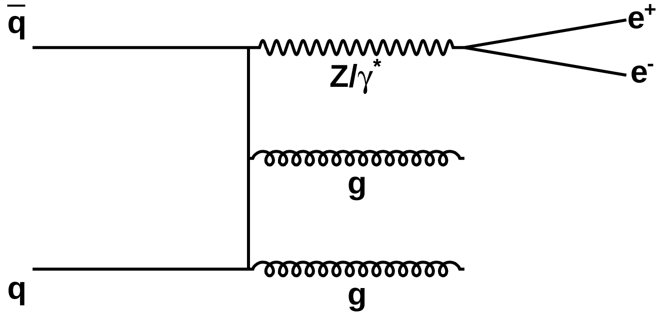

Figure 8. Feynman diagram for Z/γ^* production in association with two gluons via $q\bar{q} \rightarrow Z/\gamma^* gg$.

CHAPTER 3

EXPERIMENTAL APPARATUS

The Fermi National Accelerator Laboratory (FNAL, or Fermilab) currently operates the world's highest energy proton-antiproton collider, the *Tevatron*. In this chapter the chain of accelerators that is necessary to achieve a center-of-mass collision energy of 1.96 TeV is described. An overview of the DØ detector which is built around one of the interaction regions where protons and antiprotons collide is given.

The data used in this analysis were recorded with the DØ detector during the data taking period known as Run II, which officially began in March 2001.

3.1 The Fermilab Accelerators

The Tevatron is the final stage in a sequence of seven accelerators (17; 18; 19). A Cockcroft-Walton *pre-accelerator*, a linear accelerator (*Linac*) and a synchrotron (*Booster*) provide a source of 8 GeV protons. The antiproton *Debuncher* and *Accumulator* are two components of the *Antiproton Source*. The *Main Injector* serves as the final boosting stage before injecting protons and antiprotons into the Tevatron. It also provides the necessary source of energetic protons which are needed in the Antiproton Source.

Figure 9 gives an overview of the Fermilab accelerator complex.

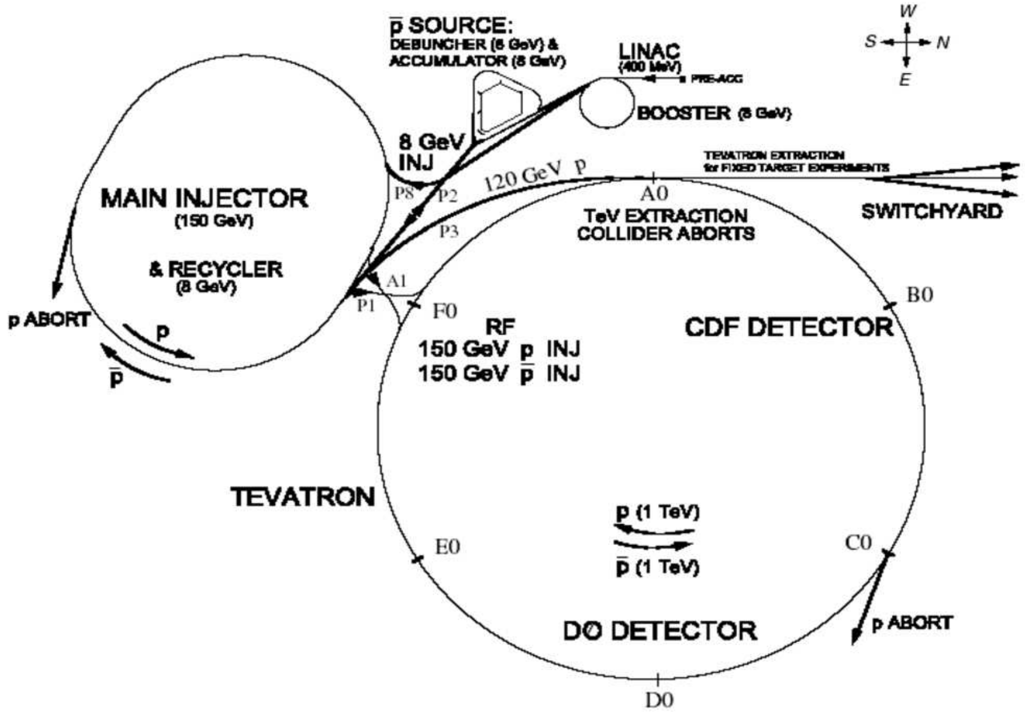

Figure 9. Schematic view of the Fermilab accelerator chain.

3.1.1 The Pre-accelerator

The purpose of the pre-accelerator is to produce negatively charged hydrogen ions (H^-) with an energy of 750 keV, which are then transferred into the Linac.

Hydrogen gas (H_2) enters a magnetron surface-plasma source (Figure 10). Due to the electric field between the anode (negatively charged) and cathode (positively charged), the electrons are stripped away from the hydrogen atoms to create a plasma. The positively charged hydrogen ions then strike the surface of the cathode to collect extra electrons and thereby form negatively charged hydrogen ions. The H^- ions are extracted through the anode aperture with an electric field of 18 kV applied by the extractor plate (Figure 10).

A commercial Cockcroft-Walton Generator produces a 750 kV potential differential by charging capacitors in parallel from an AC voltage source and discharging them in series, via diodes [1]. The Cockcroft-Walton Generator is used to further accelerate the H^- ions to an energy of 750 keV.

After exiting the Cockcroft-Walton device the H^- ions travel through a transfer line. Before entering into the Linac the continuous stream of H^- ions passes through a single gap radio frequency (RF) cavity which bunches the beam at the RF frequency of the Linac (201.24 MHz).

---

[1] The maximum voltage is limited by how much the air can "stand off" before sparking.

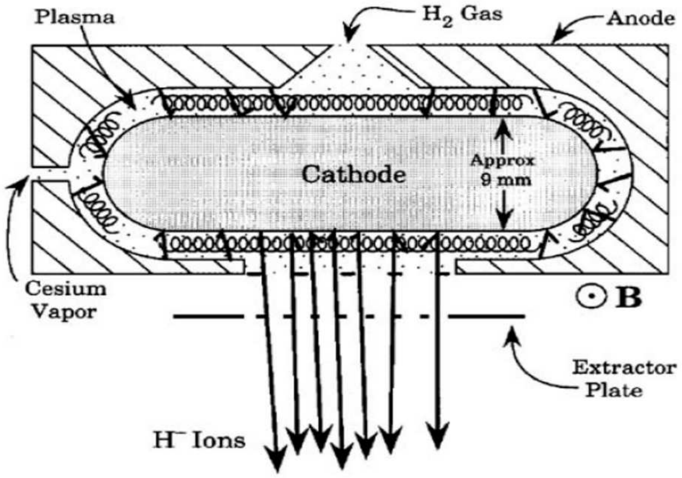

Figure 10. Schematic view of magnetron operation for the hydrogen ion source.

3.1.2 The Linac

The Linac receives bunches of 750 keV H^- ions from the pre-accelerator and accelerates them further to an energy of 400 MeV using RF cavities (Figure 11). The RF cavities are contained within a collection of steel tanks which are holding a sequence of drift tubes separated from each other by gaps. In order to accelerate H^- ions, the cavities are designed in such a way that particles traveling in the gaps experience an acceleration, while particles traveling in the drift tubes are shielded from the RF.

After passing through the Linac, bunches of 400 MeV H^- ions are transferred into the Booster.

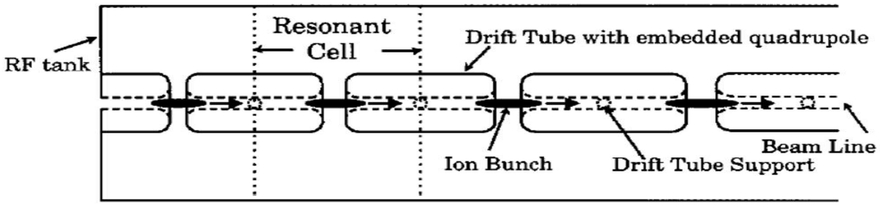

Figure 11. Schematic of Linac RF cavity.

3.1.3 The Booster

The Booster is the first synchrotron in the chain of accelerators. It consists of a sequence of dipole and quadrupole magnets and 17 RF cavities arranged in a circle with a diameter of 151 m. The Booster accelerates protons to an energy of 8 GeV.

It is easier to merge negatively charged H^- ions coming from the Linac with protons (H^+ ions) circulating in the Booster due to their opposite charge. Therefore the two beams are merged with the help of dipole magnets, and the electrons are stripped from the H^- ions by letting the combined beam pass through a carbon foil.

Once the Booster is filled with proton bunches, the RF cavities provide an acceleration up to 8 GeV. At the same time the field strength in the dipole magnets is adjusted accordingly in order to maintain a constant radius for the circulating particles. Once the protons have reached an energy of 8 GeV they are transferred into the Main Injector.

3.1.4 The Main Injector

The Main Injector is a circular synchrotron with a diameter of 1 km. It can accelerate both protons (coming from the Booster) and antiprotons (coming from the Antiproton Source) from 8 GeV to 150 GeV before injecting them into the Tevatron. It also delivers 120 GeV protons to the Antiproton Source.

3.1.5 The Antiproton Source

The Antiproton Source consists of three major components: the *Target Station*, the *Debuncher*, and the *Accumulator*. In the first step the Target Station receives 120 GeV protons from the Main Injector and diverts them onto a Nickel Target. This produces a shower of secondary particles (including antiprotons) at many different angles and with a large spread in particle momentum. A Lithium lens and bending magnets are used to focus the beam and remove positively charged particles (Figure 12). A process called *stochastic cooling* is used in both the Debuncher and Accumulator in order to reduce the spread in momentum and position of the antiprotons and thereby “cooling” them.

Both the Debuncher and Accumulator are located in a rounded-triangle shaped tunnel with a circumference of about 51 m. Antiprotons coming from the Target Station are transferred into the Debuncher where the momentum spread of the particles is reduced. It is technically very challenging to accumulate a large quantity of antiprotons. On average, for every 1 million protons that hit the Nickel target, only about 20 antiprotons can be gathered. Therefore the Accumulator stores antiprotons until a sufficient amount has been generated that can be trans-

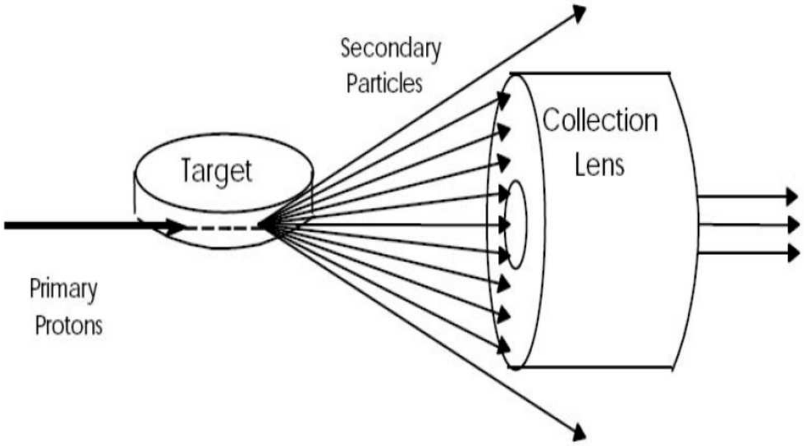

Figure 12. Simplified drawing of anti-proton production with nickel target and lithium lens.

ferred into the Main Injector. The Accumulator must be capable of storing antiprotons over many hours.

3.1.6 The Tevatron

The Tevatron is the final stage in the sequence of proton and antiproton acceleration. It has a diameter of 2 km and uses superconducting magnets which operate at liquid helium temperature providing magnetic fields of up to 4 Tesla. Protons and antiprotons are accelerated to 980 GeV, leading to a center-of-mass collision energy of 1.96 TeV.

Protons and antiprotons travel in groups of particles (*bunches*) in opposite directions while sharing the same beam pipe. A full revolution (*turn*) takes ≈21 μs. The Tevatron injects 36 bunches of both protons and antiprotons for each store. A three fold symmetry is imposed by separating the 36 bunches into three superbunches. Overall, this leads to a time structure where bunches of protons and antiprotons (*live bunch crossings* or *zero bias events*) collide at 1.7 MHz (20).

3.2 Luminosity and Cross Section

Luminosity $\mathcal{L}$ is a measure of the particle flux per unit area and per unit time ($\mathrm{cm}^{-2}\mathrm{s}^{-1}$). In a collider experiment such as DØ, the luminosity gives an indication of how many proton-antiproton crossings occur in a given time and area. The luminosity is determined by measuring the rate of inelastic proton-antiproton scatterings for each bunch crossing, using scintillator arrays located near the beam pipe. These measurements are normalized to the expected (from previous measurements at lower $\sqrt{s}$) inelastic cross sections (21; 22).

The cross section σ is a measure of the interaction probability per unit flux. Cross sections are usually expressed in *barns*, where 1 barn $= 10^{-24}$ cm^2.

The number of times a given process occurs, N, is proportional to $\mathcal{L}$ and σ:

$$N = \sigma \cdot \int \mathcal{L}\ dt, \tag{3.1}$$

where $\int \mathcal{L}\ dt$ is called *integrated luminosity.* Figure 13 shows the integrated luminosity profile of the Tevatron, covering the data taking period from April 2002 through June 2005. A total integrated luminosity of 343 pb^{-1} was used for the result presented in this analysis.

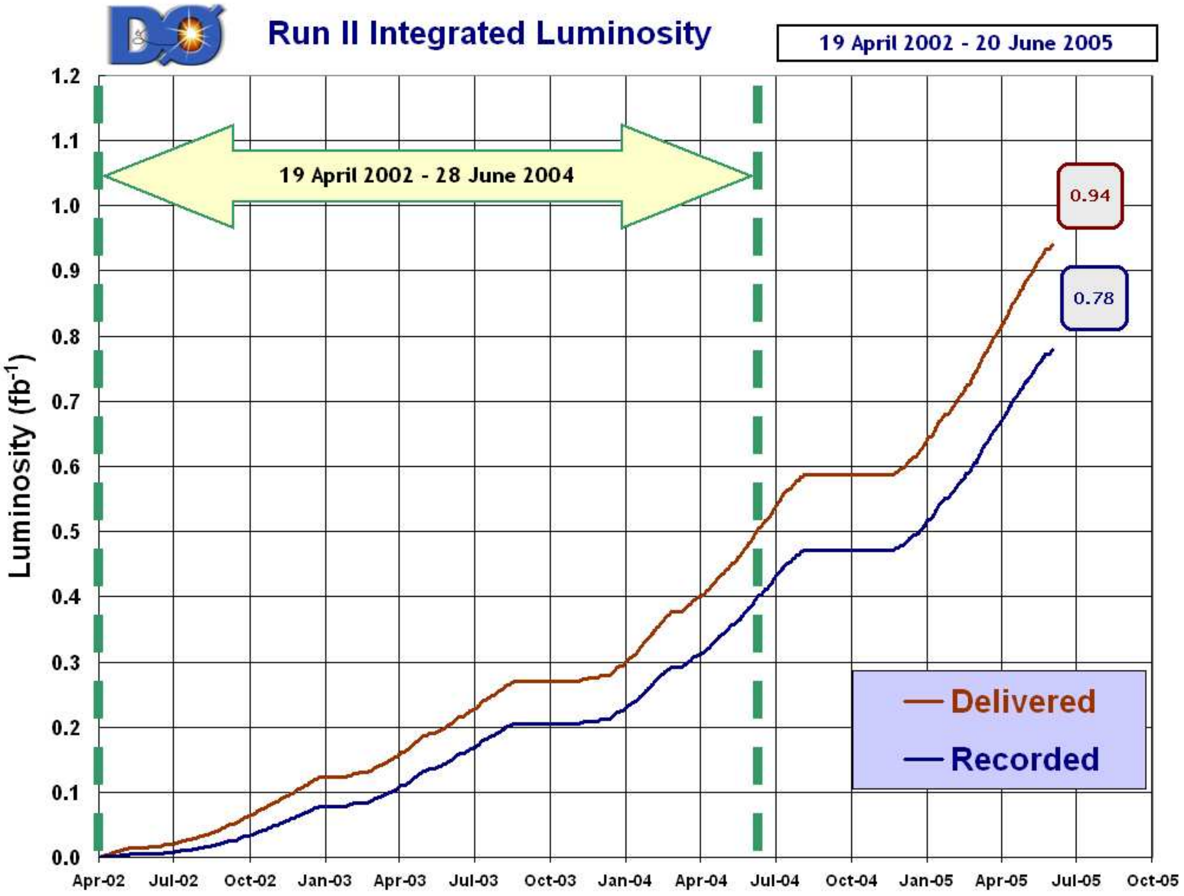

Figure 13. Tevatron integrated luminosity delivered to DØ (April 2002 - June 2005). The arrow indicates the period during which the data for this analysis were recorded.

3.3 The DØ Detector

The DØ detector (23; 24) has a magnetic central-tracking system, consisting of a silicon microstrip tracker (SMT) and a central fiber tracker (CFT), both located within a 2 Tesla superconducting solenoidal magnet (Figure 14). Central and forward preshower detectors are located outside of the superconducting coil. A liquid-argon/uranium calorimeter has a central section (CC) covering pseudorapidities $|\eta|$ up to ≈ 1, and two end calorimeters (EC) extending coverage to $|\eta| \approx 4$, all three housed in separate cryostats. A muon system resides beyond the calorimetry, and consists of a layer of tracking detectors and scintillation trigger counters before 1.8 Tesla toroids, followed by two more similar layers after the toroids. Luminosity is measured using plastic scintillator arrays located in front of the EC cryostats. The three-tiered trigger and data acquisition systems are designed to accommodate the high luminosities of Run II.

Although a full description of the DØ detector is given in this chapter, the elements that are most relevant for the analysis presented in this dissertation are the calorimeter (Chapter 3.3.4) and tracking system (Chapter 3.3.2).

3.3.1 Coordinate Systems

The coordinate system used for the DØ detector is right-handed. It has the positive z-axis aligned with the direction in which the protons travel, and the positive y-axis pointing upwards.

In most cases cylindrical coordinates are used (z, Φ, θ). Φ is the azimuthal angle in the plane perpendicular to the beam (z-axis), where Φ=0 coincides with the positive x-axis. θ is the polar angle relative to the positive z-axis.

Since the colliding protons and antiprotons can exhibit a significant net boost along the

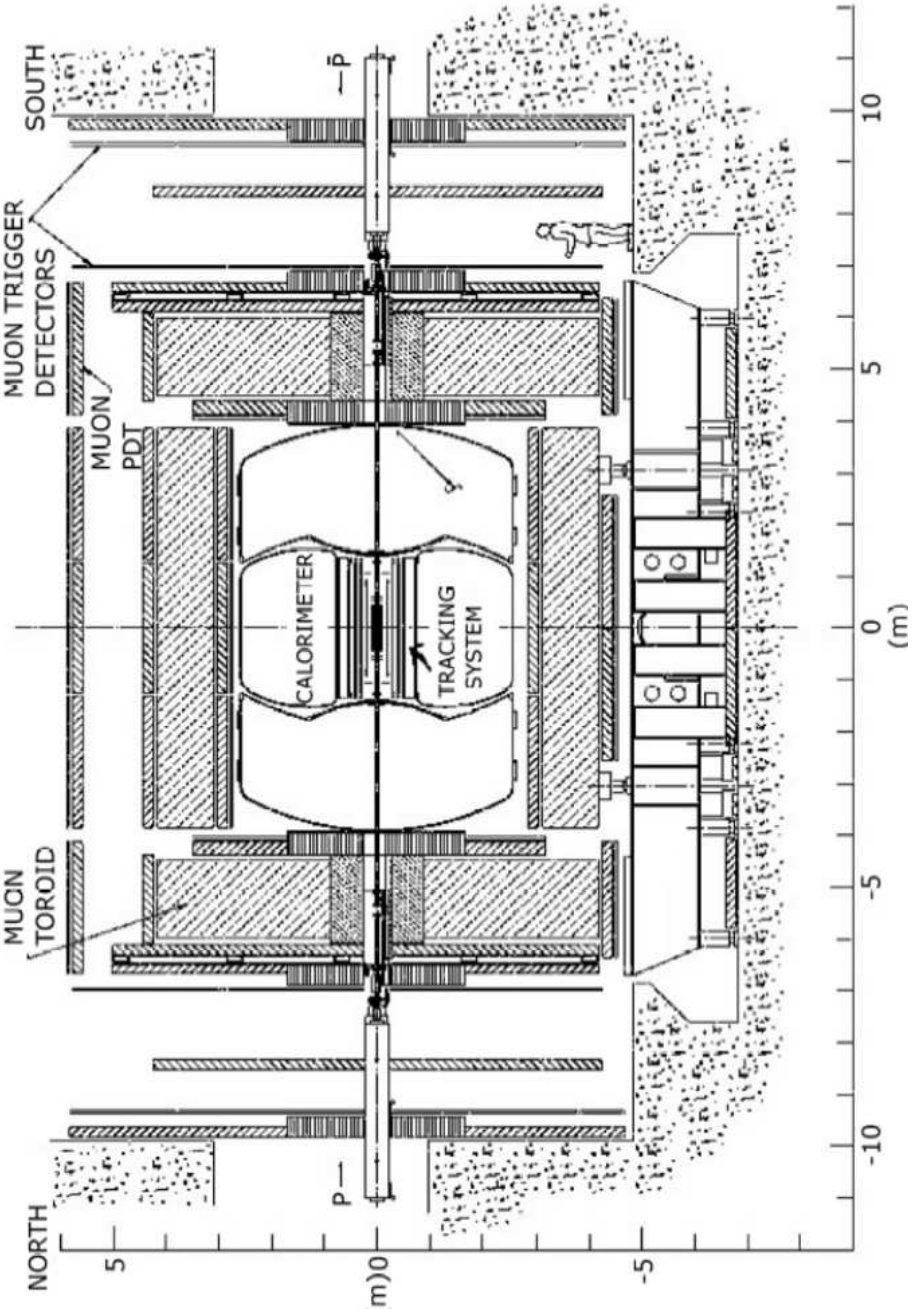

Figure 14. Schematic view of the Run II DØ detector.

z-axis, it is suitable to choose a polar angle quantity that is invariant under relativistic transformations. Therefore it is often more convenient to use pseudorapidity η instead of the polar angle θ:

$$\eta = -ln \cdot \left[tan\frac{\theta}{2}\right] \tag{3.2}$$

The pseudorapidity approximates the true rapidity,

$$y = \frac{1}{2} \cdot ln\left[\frac{E + p_z}{E - p_z}\right] \tag{3.3}$$

in the limit of $m \ll E$ (where m is the invariant mass $m^2 = E^2 - p^2$). The term "forward" is used to describe regions at $|\eta| > 1.1$.

In many cases some of the products of a proton-antiproton collisions escape along the beam pipe, which makes it difficult to measure momentum components along the z-axis accurately. Therefore it is more convenient to use the momentum vector projected onto a plane perpendicular to the beam axis (*transverse momentum*):

$$p_T = p \cdot sin\theta. \tag{3.4}$$

In a similar fashion *transverse energy* is defined as

$$E_T = E \cdot sin\theta. \tag{3.5}$$

Unless stated otherwise, the four-momentum vectors for objects observed in the calorimeter are calculated using calorimeter energies.

3.3.2 Central Tracking System

The central tracking system measures the position and momentum of tracks resulting from the paths of charged particles. It is also essential in measuring the position of the primary interaction vertex with high accuracy, which subsequently allows good measurement of lepton p_T, jet E_T and missing transverse energy ($\not\!\!E_T$). It can also detect the presence of b-quarks through the measurement of displaced vertices.

The Central Tracking System consists of the silicon microstrip tracker (SMT), the central fiber tracker (CFT) and the superconducting solenoid (Figure 15). Combining information from both SMT and CFT, the primary vertex resolution is approximately 35 μm along the beamline. Jets originating from the decay of b-quarks can be measured with an impact parameter resolution of less than 15 μm in the $r - \Phi$ plane.

3.3.2.1 Silicon Microstrip Tracker

In order to be able to detect the paths of charged particles emerging from a proton-antiproton collision, the SMT (25) uses wafers of silicon with a thickness of 300 μm. When a charged particle passes through a positive-negative ($p - n$) junction in silicon, it produces electron-hole pairs that can be separated by an applied voltage. The charge which is collected can then be stored in capacitors and later read-out and digitized. The SMT contains approximately 800,000 individual channels. Figure 16 shows the design of a basic silicon detector unit (*ladder*).

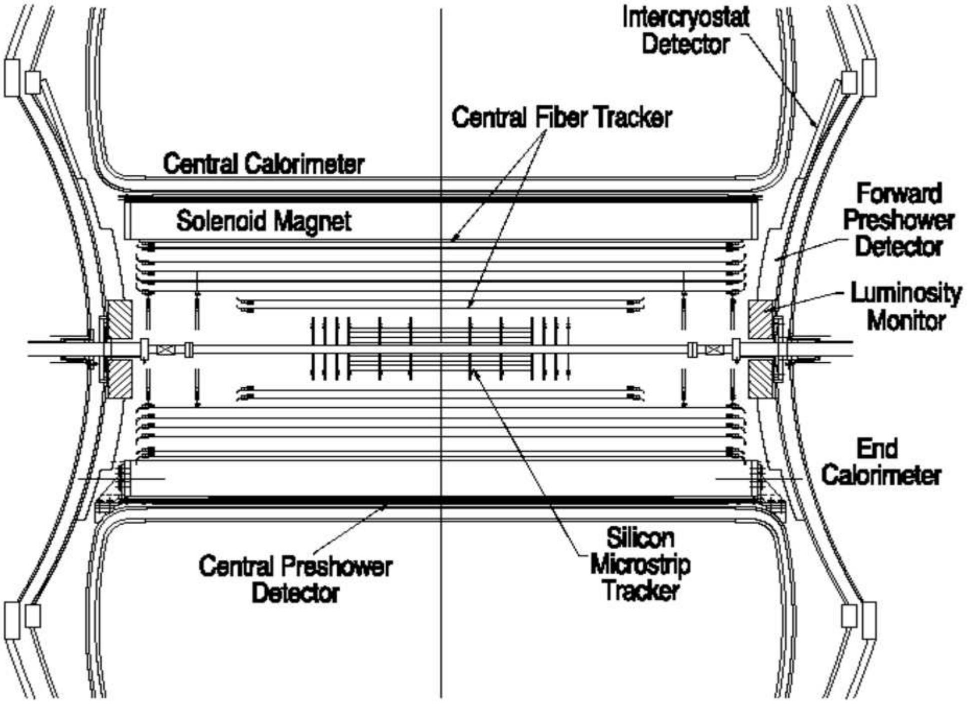

Figure 15. The DØ central tracking system with solenoid, preshower detectors, luminosity monitor, and calorimeter.

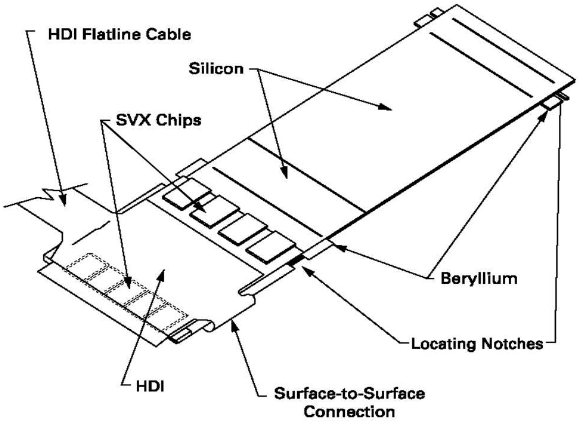

Figure 16. Double-sided ladder design, n-side.

The SMT is designed in such a way that tracks of charged particles are perpendicular to detector material over a large range of η values. The structure of the device is mostly dictated by the fact that the interaction region is spread out with respect to the center of the detector ($\sigma \approx 25$ cm). This lead to a design of barrel modules combined with disks in the center and larger disks in the forward region (Figure 17). The SMT has six barrels along the z-axis, each containing four detector layers with a maximal outer radius of 10.5 cm. There are twelve small diameter double-sided “F” disks and four large diameter single-sided “H” disks to cover the far forward region ($|\eta| < 3$). The F-disks are at $|z| = 12.5$, 38.2, 43.1 and 53.1 cm. The centers of the H-disks are located at $|z| = 100.4$, 121.0 cm.

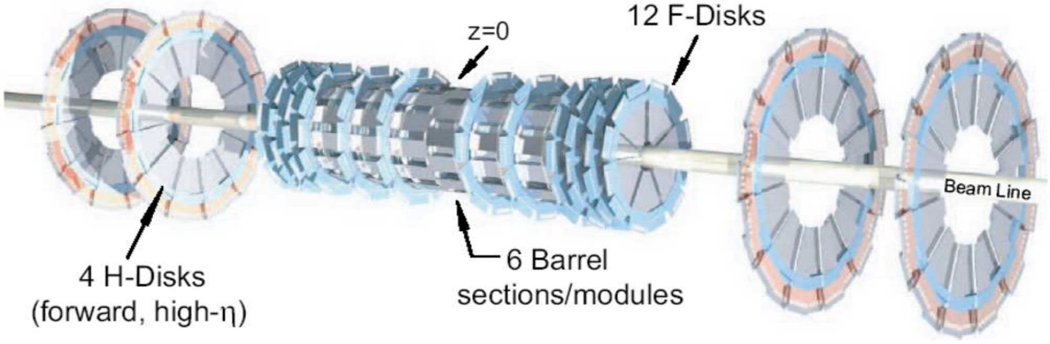

Figure 17. SMT disk and barrel design.

3.3.2.2 Central Fiber Tracker

The Central Fiber Tracker (CFT) (26) is located in between the SMT and the edge of the solenoid magnet. The purpose of the CFT is to improve the detection of charged particle tracks within $|\eta| < 2$. It consists of approximately 70,000 scintillating fibers mounted on eight concentric support cylinders with inner and outer radii of 20 and 52 cm, respectively. Each cylinder carries two layers of fibers running parallel to the beampipe (*axial layers*), and two layers of fibers oriented at small angles of $\pm 3^\circ$ (*stereo layers*) (Figure 18). The scintillating fibers have a diameter of 835 μm and are composed of a scintillating core surrounded by a layer with a high index of refraction, which leads to total internal refraction.

Charged particles passing through a scintillating fiber excite the molecules in the fiber which subsequently release photons in the yellow-green part of the visible light spectrum as they relax

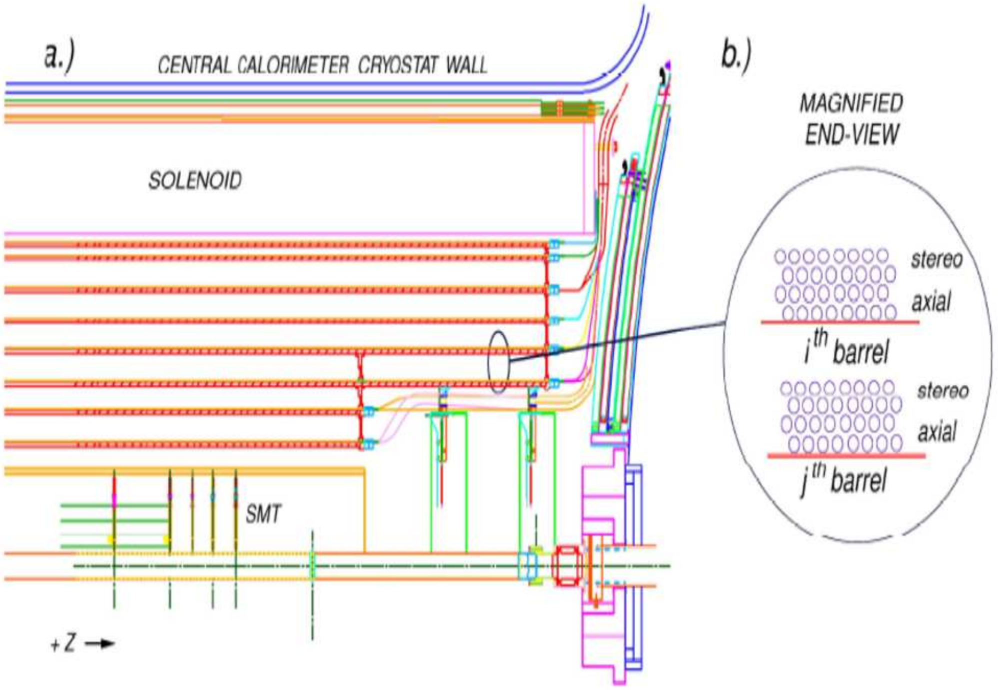

Figure 18. a) Location of the Central Fiber Tracker (CFT). b) Closeup view of axial and stereo layers.

to their ground states. Clear fiber waveguides carry the scintillation light to visible light photon counters (VLPCs) that convert the light into electrical signals. The VLPCs are silicon avalanche photodetectors that operate at liquid helium temperature in order to reduce the background due to electronic noise.

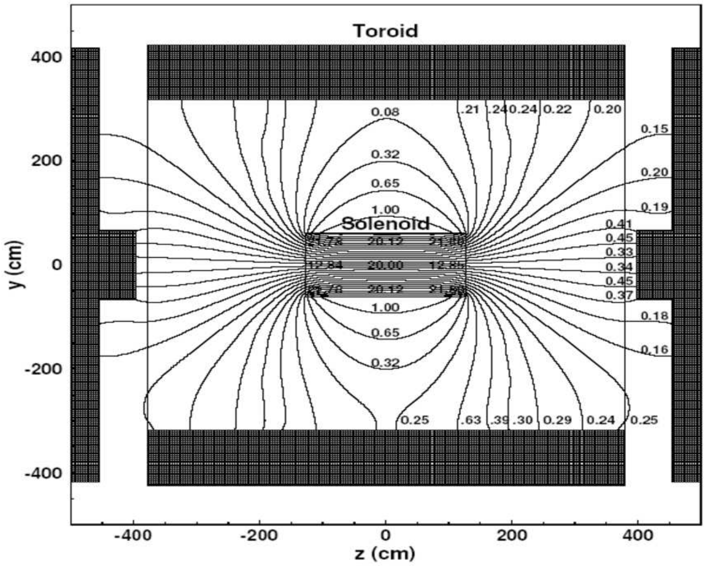

Figure 19. $y - z$ view of the DØ magnetic field with both the toroid and solenoid magnets at full current. Numbers are in kG (10 kG = 1 T).

3.3.2.3 Solenoidal Magnet

The superconducting solenoidal magnet significantly improves the capabilities of the DØ detector since it allows measuring the momentum of charged tracks. The location and physical size of the magnet are constrained by the available space between the inner tracking system and the vacuum vessel of the central calorimeter. The magnet has a length of 2.73 m and a diameter of 1.42 m and provides uniform field of 2 T (20 kG) over most of the region covered by the inner tracking system (Figure 19). Figure 20 shows a perspective view of the solenoid inside the central calorimeter with its chimney and control dewar.

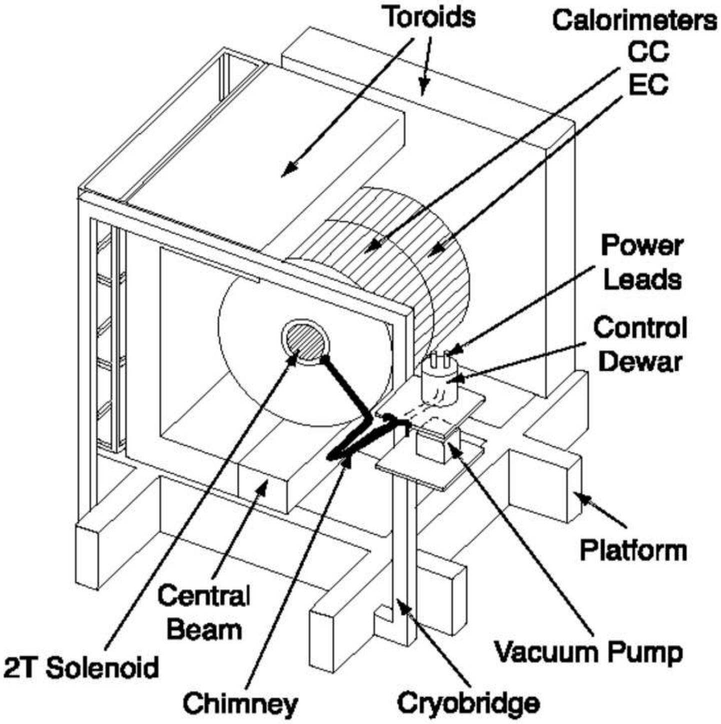

Figure 20. Perspective view of the solenoid inside the central calorimeter.

3.3.3 Preshower Detectors

The preshower detectors (27; 28) are designed to improve the identification of electrons and photons, and to correct for their upstream energy losses during offline event reconstruction. Due to their fast response time, the preshower detectors can also be used for Level 1 triggering (see Chapter 4.1).

Scintillators are used to detect both position and energy of charged particles. In contrast to the scintillators used in the CFT, preshower scintillators are triangular shaped (Figure 21). This arranges scintillator layers without creating any dead space and thereby improves the accuracy of position measurements. The center of each scintillator carries a wavelength-shifting fiber which collects the light created by passing charged particles. The light is transmitted via clear fibers to VLPCs for readout.

3.3.3.1 Central Preshower Detector

The Central Preshower Detector (CPS) is located in the 5 cm gap between the solenoid and the central calorimeter, covering the region $|\eta| < 1.3$ (Figure 15). It consists of a layer of lead radiator which has a thickness corresponding to approximately one radiation-length (X_0), followed by three layers of triangular scintillator strips. The scintillating layers are arranged in an axial-u-v geometry, with a u stereo angle of 23.8° and a v stereo angle of 24.0°. Each layer has a total number of 2,560 readout channels.

3.3.3.2 Forward Preshower Detector

The two Forward Preshower Detectors (FPS) are attached to the faces of the end calorimeters and cover a region of $1.5 < |\eta| < 2.5$ (Figure 15). Each detector consists of an upstream

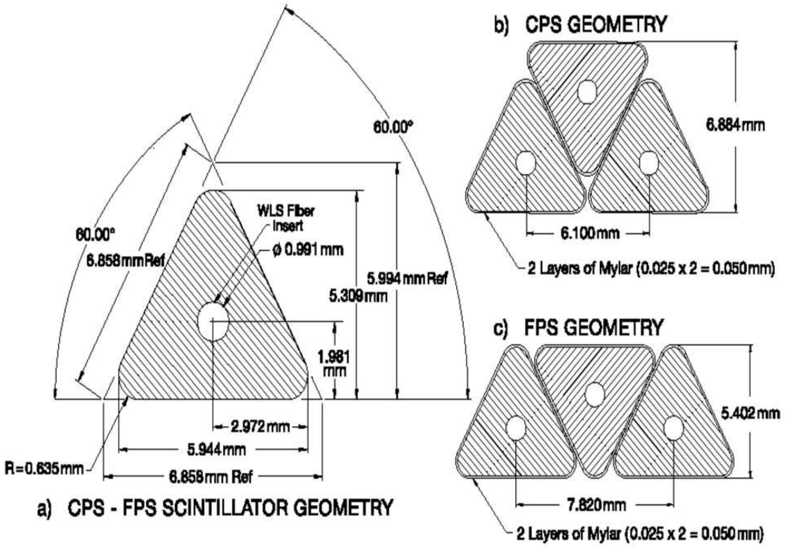

Figure 21. Cross section and layout geometry of CPS and FPS scintillator strips.

double layer of scintillator strips (minimum ionizing particle layers, or MIP layers), followed by a lead-stainless-steel absorber layer, and another double layer of scintillator strips behind it (shower layers).

3.3.4 Calorimeter

The main purpose of the calorimeter system is to measure the position and energy deposits from electrons, photons, and jets. In addition, by imposing transverse energy balance in an event, it can also detect the presence of neutrinos.

The calorimeter system consists of a central calorimeter (CC) covering $|\eta| < 1.2$ and two end calorimeters (EC), covering $1.3 < |\eta| < 4.5$ (Figure 22). Each of the calorimeters has an electromagnetic section, followed by fine and coarse hadronic sections (FH and CH respectively). Since liquid argon is used as the active medium, all calorimeters are contained within cryostats. Different types of materials are used for absorber plates:

- 3 mm (4 mm) plates of depleted uranium for the CC (EC) electromagnetic sections.
- 6 mm plates of uranium-nobium (2%) for the fine hadronic sections.
- 46.5 mm plates of copper (stainless steel) for the CC (EC) coarse hadronic sections.

A typical calorimeter cell is shown in (Figure 23). Each cell consists of a grounded absorber plate and a signal board maintained at a positive high voltage of typically 2 kV. The 2.3 mm gap between the absorber plate and signal board is filled with liquid argon. The calorimeter cells are arranged to form pseudo-projective towers (Figure 24).

In order to measure the energy of electromagnetically interacting objects, the calorimeter takes advantage of the electromagnetic shower process. For example, an incoming high-energy electron will emit Bremsstrahlung photons when passing through the dense absorber material. The emitted photons will subsequently decay into electron-positron pairs. The shower will continue until low energy photons start interacting via Compton and photoelectric effect and the electrons/positrons via ionization. At each stage of the electromagnetic shower, charged particles are ionizing the liquid argon. The high voltage between the absorber plates and signal boards is then used to collect the ionization charges to measure the energy in the shower. Typical transverse sizes of electromagnetic showers are in the range of 1-2 cm.

Hadronic showers are induced by the interaction between hadronic particles and the nuclei of the absorber material via the strong nuclear force. Secondary hadronic particles then further

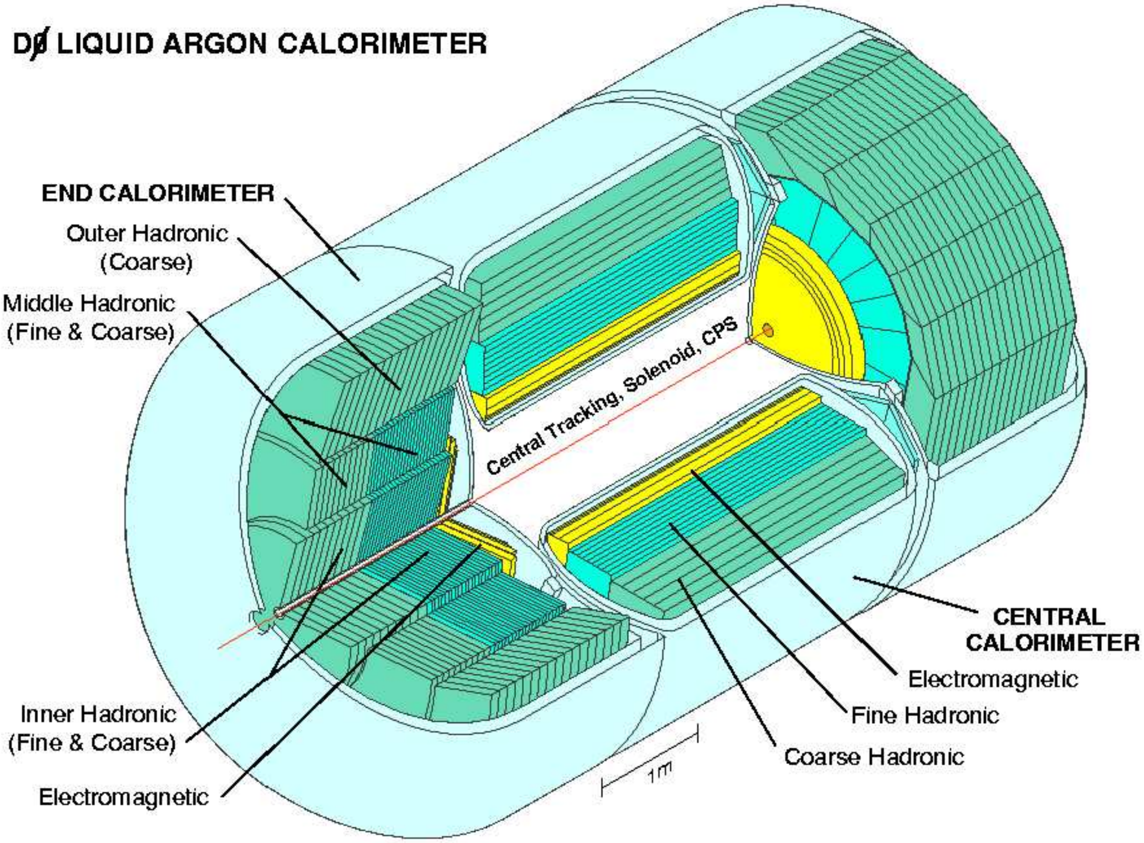

Figure 22. Isometric view of the central and two end calorimeters.

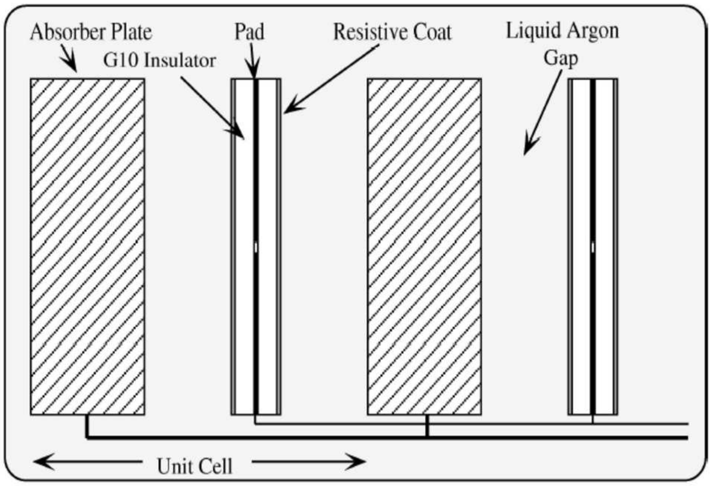

Figure 23. Schematic view of two calorimeter cells.

interact via inelastic nucleus collisions till their energy falls below a threshold. Typical transverse sizes of hadronic showers are of the order of 10 cm.

The space in between the central and end calorimeters ($1.1 < |\eta| < 1.4$) is referred to as the intercryostat region (ICR). In order to be able to measure the energies of particles that pass through this gap in the calorimeter coverage, additional detectors are used. Calorimeter cells called massless gaps (MG) are installed before the first layer of uranium inside of the central and end cryostats. Additionally, a ring of scintillator tiles mounted to the exterior surface of the end cryostats comprises the intercryostat detector (ICD).

Figure 25 shows the different calorimeter detection layers for a given η value (29).

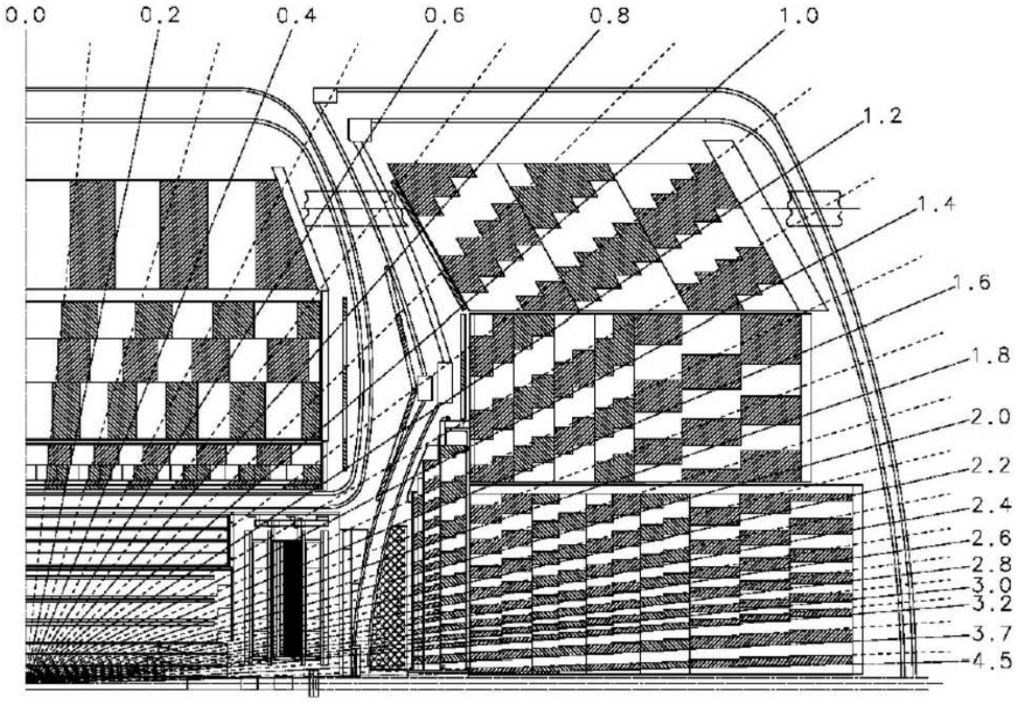

Figure 24. Schematic view showing the calorimeter segmentation pattern. The shading pattern indicates cells for signal readout. The radial lines show the detector pseudo-rapidity intervals.

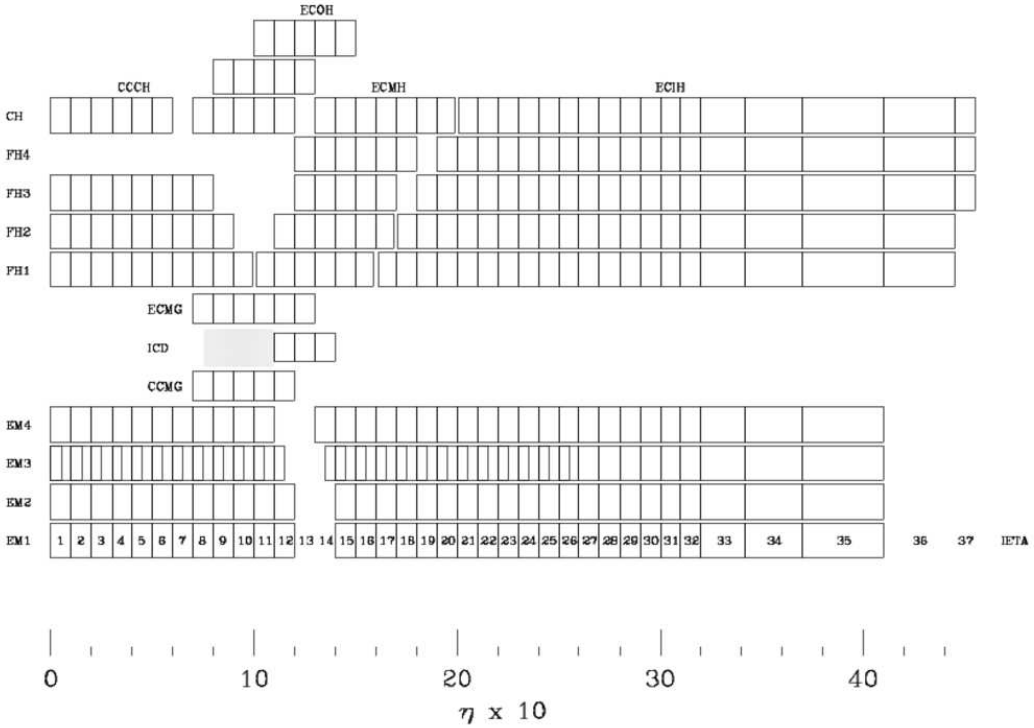

Figure 25. Schematic view of different calorimeter detection layers vs η.

3.3.5 Muon System

Due to their large mass and long lifetime, muons pass through the calorimeter by depositing only a small amount of energy (≈ 2.5 GeV) via ionization. Therefore, the outermost subdetector is dedicated to the detection of muons (Figure 26). The muon system is separated into central and forward detectors. A 1.9 T iron toroid magnet is used for muon momentum measurements.

Proportional Drift Tubes (PDT), Mini Drift Tubes (MDT), and scintillators are the main detection elements used in the muon system. Drift tubes collect the ionization charges created by muons passing through a gas mixture onto high voltage wires. Correlating the arrival times of ionization charges from different drift tubes with the beam crossing time, allows to extrapolate the path of muons as they pass through the detector. Scintillators are mainly used for their good timing resolution (≈ 4 ns) which allows to trigger on muons.

The central muon system (30) covers the region of $|\eta| < 1.0$ and is referred to as the Wide Angle Muon System (WAMUS). It consists of three PDT layers, with the first layer (A layer) in between the toroid magnet and the calorimeter, and two more layers (B and C layers) after the toroid magnet. Additional layers of scintillators before the A layer and covering the outside of the muon system allow to reject cosmic rays by using spatial and precise timing measurements

. The forward muon system (31) covers the region of $1.0 < |\eta| < 2.0$ and is referred to as the Forward Angle Muon System (FAMUS). It consists of three MDT layers and scintillators, with the first layer (A layer) before the toroid magnet, and two more layers (B and C layers) after the toroid magnet.

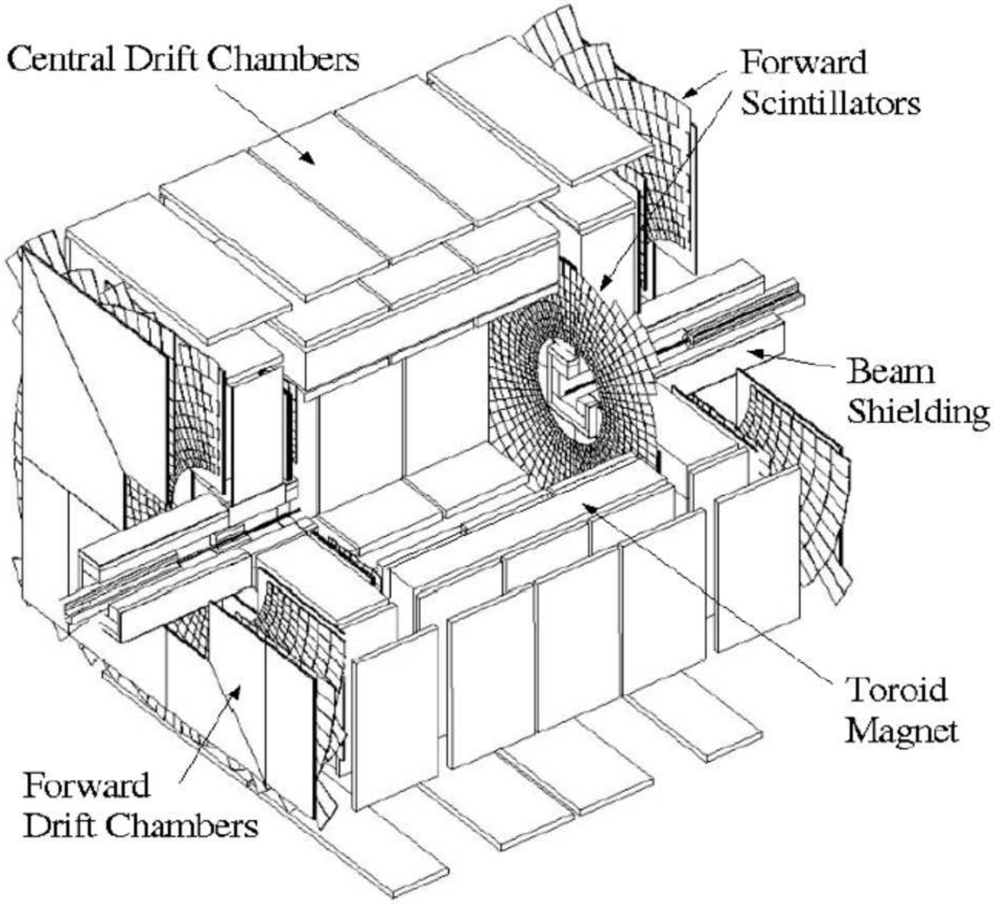

Figure 26. The DØ muon system.

CHAPTER 4

THE DØ TRIGGER AND DATA ACQUISITION SYSTEMS

DØ uses a three level trigger system (32; 33) to handle proton-antiproton collision rates of 1.7 MHz. Each succeeding level of triggering processes fewer events, with more sophisticated trigger algorithms. At the first stage, the Level 1 (L1) system uses a hardware trigger to reduce the event rate to $\approx$ 1.5 kHz. At the next stage, the Level 2 (L2) system further reduces the event rate to $\approx$ 800 Hz. L2 uses hardware engines associated with specific detector subsystems and a single global processor for the final L2 trigger decision. In the last step, the Level 3 (L3) system which consists of a farm of microprocessors reduces the event rate to $\approx$ 50 Hz. Only those events that pass all three trigger levels are stored for further offline reconstruction and analysis.

Figure 27 illustrates how the trigger system is integrated with the read-out of data. The overall coordination and control of DØ triggering is handled by the COOR software package. COOR interacts directly with the trigger framework for L1 and L2 triggers and with the data acquisition supervising system for the L3 triggers. A given event that passes L1 and L2 trigger requirements is fully digitized and transferred to L3 for further examination.

4.1 The Level 1 Trigger

The L1 trigger system uses information from the tracking, preshower, calorimeter, and muon subdetectors to provide an event rate reduction by a factor of $\approx$ 1000. Field programmable

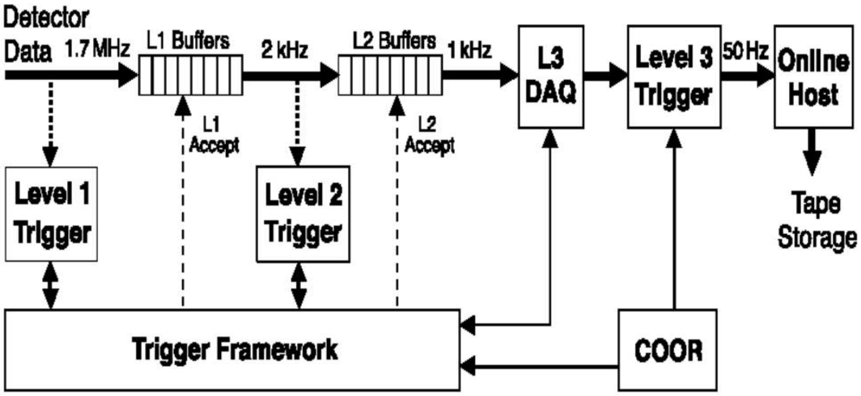

Figure 27. Overview of the DØ trigger and data acquisition systems.

gate arrays (FPGAs) check whether a given event satisfies the L1 trigger conditions. If at least one trigger condition is satisfied, the event information is digitized and buffered to await a L2 decision. L1 trigger decisions are made within a 3.5 μs time window.

4.1.1 The Level 1 Trigger Framework

The L1 trigger framework (TFW) gathers information from each of the L1 subsystems and decides whether a given event is to be buffered for further examination. Up to 128 L1-specific triggers can be implemented in a *trigger list*. The "OR" of all triggers in the trigger list determines whether or not a given beam crossing has a valid trigger. Different triggers can be implemented by COOR via commands interpreted in the trigger control computer (TCC). The L1 TFW also manages the prescaling ratios which are used to reduce the rate of certain triggers. A large number of scalars is provided by the L1 TFW to monitor trigger rates and deadtimes.

4.1.2 The Level 1 Calorimeter Trigger

For trigger purposes the calorimeter is segmented into 1280 trigger towers of $\Delta\eta \times \Delta\Phi = 0.2 \times 0.2$. Level 1 calorimeter (L1CAL) trigger decisions are based on the amount of transverse energy deposited in the electromagnetic layers (EM) and electromagnetic plus fine hadronic layers (TOT) of the trigger towers. L1CAL trigger conditions require that a specific number of EM or TOT trigger towers be above a certain transverse energy threshold. In addition L1CAL can also impose thresholds on the total sum of transverse energy and the missing transverse energy in a given event.

4.1.3 The Level 1 Central Track Trigger

The Level 1 Central Track Trigger (L1CTT) uses information from the CFT and CPS subdetectors in the central region ($|\eta| <$1.7), and information from the CFT and FPS subdetectors in the forward region (1.4$< |\eta| <$2.5). Possible track candidates are identified by FPGAs using hit patterns in the axial layers of the CFT and matching energy deposits in the preshower detectors (Figure 28). The p_T of a track candidate can be estimated by the azimuthal bend of the CFT hits. L1CTT track candidates are assigned into p_T bins according to their transverse momenta: 1.5-3 GeV; 3-5 GeV; 5-10 GeV; or above 10 GeV. Trigger conditions can be specified by a certain number of tracks above a p_T threshold, with or without the requirement of a CPS cluster match to the track.

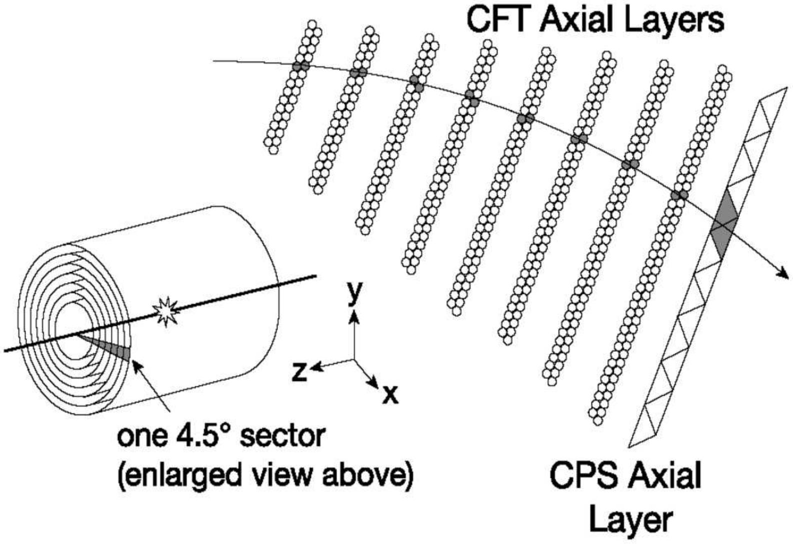

Figure 28. A hypothetical L1CTT track with hits in eight CFT axial doublet layers and the CPS axial layer.

4.1.4 <u>The Level 1 Muon Trigger</u>

The Level 1 Muon Trigger (L1Muon) uses information from the muon wire chambers, muon scintillators, and L1CTT tracks. L1Muon trigger logic is implemented in FPGAs and trigger conditions require a combination of criteria based on p_T thresholds, geographical region, track quality, and multiplicity.

4.2 <u>The Level 2 Trigger</u>

The L2 trigger system was designed to reduce the L1 event rate by a factor of <10. It receives inputs from both the L1 system and the detector subsystems (Figure 29). L2 operates in two stages. In the first stage, subdetector-specific preprocessors form physics objects such as electrons, jets, or tracks. Individual preprocessors for the tracking, preshower, calorimeter, and muon subdetectors run in parallel and are located in separate crates. L2 preprocessor physics objects are then used at the second stage by a global processor. The L2 global processor (L2GBL) makes the final L2 trigger decision by imposing selection criteria on the preprocessor physics objects, including correlations between objects from multiple detector subsystems.

The two-stage L2 architecture (*stochastic pipeline*) was designed to make trigger decisions within a ≈ 100 μs time window (see Appendix B for a more detailed description of the L2 trigger system hardware). Events passing L2 trigger requirements are flagged for full detector readout and further refined analysis at the L3 triggering stage.

4.2.1 The Level 2 Calorimeter Preprocessor

The Level 2 calorimeter preprocessor (L2Cal) receives the full list of 2560 EM and TOT trigger towers from L1CAL.

L2 Jet Algorithm: The L2 jet algorithm forms jet objects by clustering 5×5 groups of TOT trigger towers centered around seed towers. A jet seed tower is any TOT trigger tower with $E_T \geq 2$ GeV. The list of seed towers for the L2 jet algorithm is E_T-ordered. TOT E_T values are calculated relative to the center of the detector ($z = 0$ cm). For overlapping L2 jet candidates, the lower E_T cluster is dropped if $\Delta\Phi$ and $\Delta\eta$ between the centers of two adjacent clusters is less than 4 trigger towers. Figure 30 shows an example for a L2 jet overlap. A final list of E_T-ordered L2 jets is sent to L2GBL. The following summarizes all L2 jet output variables that are sent to L2GBL:

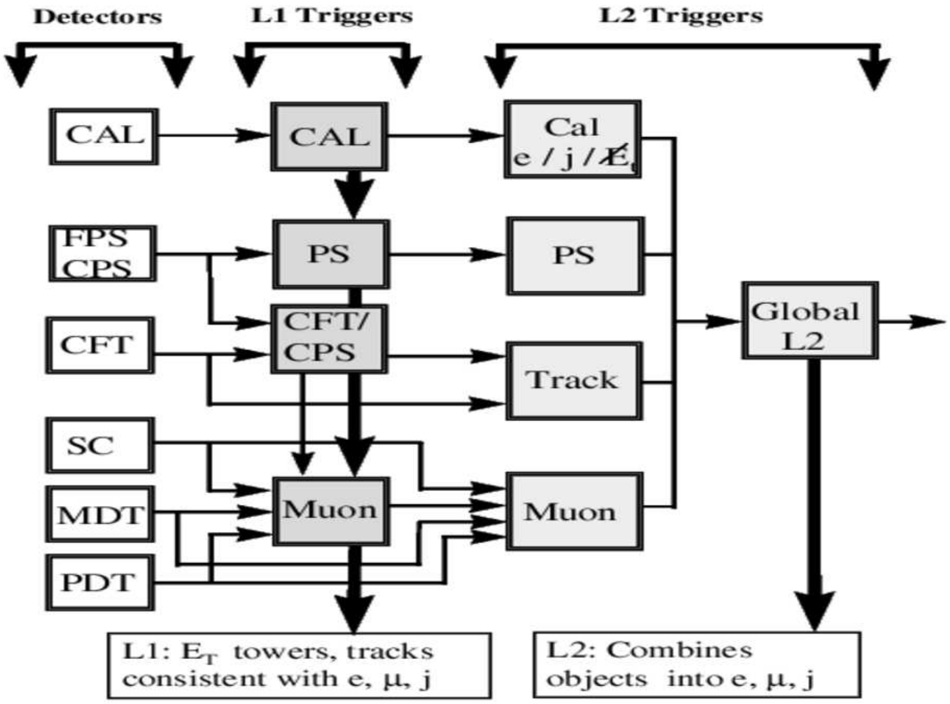

Figure 29. Schematic view of subdetectors with L1 and L2 trigger elements. Horizontal arrows indicate the direction of dataflow.

- η_{jet} is the TOT E_T weighted pseudorapidity of the jet cluster:

$$\eta = \frac{\sum_i \eta_i \times E_{T,i}}{\sum_i E_{T,i}}, \tag{4.1}$$

  where i runs over all TOT trigger towers in the 5×5 jet cluster.

- Φ_{jet} is the TOT E_T weighted azimuthal angle of the jet cluster:

$$\Phi = \frac{\sum_i \Phi_i \times E_{T,i}}{\sum_i E_{T,i}}, \tag{4.2}$$

  where i runs over all TOT trigger towers in the 5×5 jet cluster.

- E_T^{jet} is the transverse energy of the jet cluster based on the scalar E_T sum of all TOT trigger towers in the 5×5 jet cluster.
- η_{center} is the integer pseudorapidity of the center of the jet cluster.
- Φ_{center} is the integer azimuthal angle of the center of the jet cluster.
- η_{lead} is the integer pseudorapidity of the leading-E_T trigger tower in the jet cluster.
- Φ_{lead} is the integer azimuthal angle of the leading-E_T trigger tower in the jet cluster.

Additional monitoring flags are also sent.

L2 EM Algorithm: The L2 electron/photon algorithm forms EM objects by clustering the transverse energies of EM seed towers with their largest E_T neighbors. An EM seed tower is any EM trigger tower with $E_T \geq 1$ GeV. The list of seed towers for the L2 EM algorithm is E_T-ordered. EM E_T values are calculated relative to the center of the detector ($z = 0$

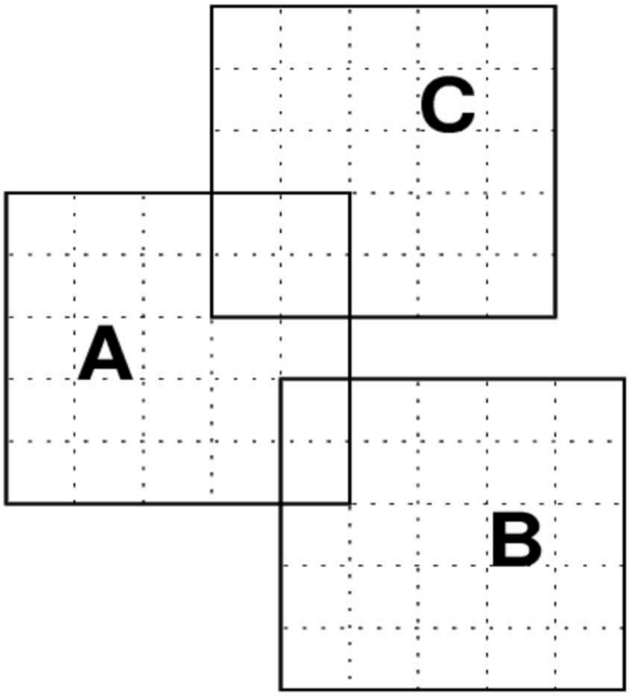

Figure 30. L2 jet overlap example. If each of the three 5 × 5 clusters satisfies the minimum cluster E_T cut, the algorithm will retain cluster 'B' and the maximum of clusters 'A' and 'B'.

cm). An E_T-ordered list of all L2 EM objects and parameters is sent to L2GBL. The following summarizes all L2 EM output variables that are sent to L2GBL:

- η_{elec} is the EM E_T weighted pseudorapidity of the EM cluster.
- Φ_{elec} is the EM E_T weighted polar angle of the EM cluster.
- E_T^{elec} is the transverse energy of the EM cluster based on the sum of the scalar EM E_T of the seed and neighboring trigger towers.
- *EM Fraction* is defined as follows:

  $$EMFraction = \frac{E_T^{EM}(seed) + E_T^{EM}(neighbor)}{E_T^{TOT}(seed) + E_T^{TOT}(neighbor)}, \tag{4.3}$$

  where $E_T^{EM}(seed)$ ($E_T^{EM}(neighbor)$) is the EM E_T of the seed (neighbor) trigger tower, and $E_T^{TOT}(seed)$ ($E_T^{TOT}(neighbor)$) is the TOT E_T of the seed (neighbor) trigger tower.
- *Isolation* is defined as follows:

  $$Isolation = 1 - \frac{E_T^{EM}(seed) + E_T^{EM}(neighbor)}{E_T^{TOT}(3 \times 3)}, \tag{4.4}$$

  where $E_T^{TOT}(3 \times 3)$ is the sum of E_T^{TOT} of 3×3 trigger towers centered on the seed trigger tower.
- $\eta_{leading}$ is the integer pseudorapidity of the seed trigger tower in the EM cluster.
- $\Phi_{leading}$ is the integer azimuthal angle of the seed trigger tower in the EM cluster.

- $\eta_{neighbor}$ is the integer pseudorapidity of the neighboring trigger tower in the EM cluster.
- $\Phi_{neighbor}$ is the integer azimuthal angle of the neighboring trigger tower in the EM cluster.

Additional monitoring flags are also sent.

4.2.2 The Level 2 Muon Preprocessors

The Level 2 Muon system (L2Muon) consists of two components: a preprocessor for the central muon region (L2 Muon Central, or L2MUC) and a preprocessor for the forward muon region (L2 Muon Forward, or L2MUF). L2Muon receives inputs from L1 (L1Muon) and the muon subdetector drift chambers and scintillators. Inputs to L2Muon are first received by *Second Level Input Computers* (SLICs) where most of the processing is done. A list of muon candidates with each containing information about η, ϕ, p_T, sign, and timing is sent to L2GBL for further processing.

4.2.3 The Level 2 Preshower Preprocessor

The Level 2 preshower preprocessor (L2PS) receives CPS and FPS information through L1CTT. CPS and FPS are treated as independent systems at the L2 stage. CPS axial clusters are combined into quadrants in azimuth before they are transmitted to L2PS. CPS stereo clusters are sent directly to L2PS. In addition, axial clusters are flagged by L1 as electrons when there is a CFT track associated with a cluster, or photons when there is no CFT track.

The L2PS algorithm derives η and ϕ coordinates for clusters that match in three layers based on CPS cluster centroids. The η and ϕ coordinates are binned to match the geometry of calorimeter trigger towers ($\eta \times \phi = 0.2 \times 0.2$). A window of width 0.05 is drawn around each calorimeter trigger tower, and any preshower hit in this η, ϕ region is designated as a calorimeter match.

Similar functionality is provided for FPS.

4.2.4 The Level 2 Tracking Preprocessor

The Level 2 tracking preprocessor uses information from L1CTT and the SMT to form lists of L2 track candidates that can be used by L2GBL for triggering. It triggers on vertices that are displaced from the primary interaction vertex. Displaced vertices are characteristic of long-lived particles such as B-Mesons, and can therefore be used to identify heavy-flavored quarks.

The L2 tracking preprocessor can be operated in two different modes. In the first mode of operation (L2 Central Track Trigger, or L2CTT), it further refines tracking information coming from L1CTT. In the second mode of operation (L2 Silicon Track Trigger, or L2STT), it combines L1CTT and SMT information. Figure 31 shows the conceptual design of L2STT (24) which uses hit information from the first and last layer of the CFT to define a *road*, and then extrapolates that road into the SMT to find additional hits in the axial strips of the SMT silicon ladders.

4.2.5 The Level 2 Global Processor

The Level 2 global processor (L2GBL) receives lists of trigger objects that are generated by all of the L2 preprocessors (L2Cal, L2MUC, L2MUF, L2PS, L2CTT, L2STT). It creates

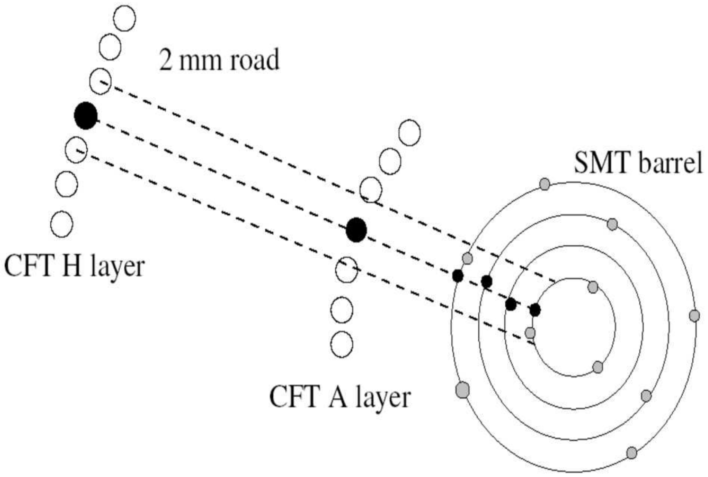

Figure 31. The definition of roads based on L1 tracks and SMT hit selection in L2STT.

global trigger objects by either using the trigger objects generated by the preprocessors or by combining trigger object information from different preprocessors. For example, spacial correlations between track candidates and EM objects in the calorimeter can be used to select a cleaner sample of electron candidates. L2GBL makes the final L2 trigger decision by imposing cuts on global trigger objects that are defined by trigger list information which is parsed from TCC.

4.3 The Level 3 Trigger and Data Acquisition

The L1 and L2 trigger systems do not use the full detector readout for their trigger decisions. The event rate needs to be reduced to less than 1 kHz, so that the Level 3 (L3) trigger system can take advantage of the full detector readout. L3 then further reduces the event rate to $\approx$ 50 Hz. The average event size is $\approx$ 200 kBytes.

The L3 trigger system is based on sophisticated reconstruction algorithms that resemble the algorithms for offline event processing (see Chapter 5) as closely as possible, given restrictions due to available processing power.

The L3 data acquisition system (L3DAQ) is based on a single Cisco 6509 Ethernet switch that transfers data at a rate of <250 Mbyte/s. Detector data are transferred from commodity VME single-board computers (SBCs), via the Ethernet switch to individual L3 farm nodes. A supervisor process running on a separate CPU provides the interface between the main DØ run control system (COOR) and L3DAQ.

After passing L3 trigger requirements, the data are buffered to local disks and finally transferred to a permanent storage facility.

CHAPTER 5

OFFLINE EVENT RECONSTRUCTION

This chapter describes how candidate electrons, jets, tracks, and vertices are *reconstructed* from the raw detector data. A collection of complex software algorithms written in C++ called *d0reco* (34) is used for this reconstruction process. As described in the previous chapter, a stream of digital readout signals from the subdetectors is recorded for each event that passes all three levels of triggering. Powerful PC computing farms are deployed to analyze the data and reconstruct candidates of physical objects (electrons, jets, tracks, etc.) that can then be used in the final analysis.

5.1 Track Reconstruction

In order to reconstruct track candidates, two different types of algorithms are used. The *Alternative Algorithm* (AA) (35) which uses a road-following method, and the *Histogramming Track Finder* (HTF) (36) which relies on a histogramming method.

The AA method starts from any combination of three hits in the SMT barrels or disks. Moving outwards, towards the CFT, the AA method then extrapolates the sequence of hits to the next SMT or CFT layer. If a hit is found within a search window, a χ^2 test is performed. If the χ^2 value is below a certain threshold, the newly found hit is associated with the track candidate. If no hit is found, a *miss* is recorded. Construction of track candidates ends when the last layer of the CFT is reached, or when three misses are recorded.

The HTF method takes advantage of the fact that the trajectory of a charged particle moving perpendicular to a homogeneous magnetic field can be characterized by three parameters: ρ, d_0, and Φ, where ρ is the radius of curvature, d_0 is the distance of closest approach with respect to (0,0) (*impact parameter*), and Φ is the direction of the track at the point of closest approach to (0,0). For track candidates with small impact parameters, every pair of hits in (x,y) coordinate space that belongs to the same track corresponds to a single point in (ρ, Φ) parameter space. Therefore, by examining every pair of hits and filling a 2-dimensional (ρ, Φ) histogram, a peak in the histogram would correspond to a track candidate.

Both track reconstruction algorithms generate lists of track candidates. A final list of tracks is generated after eliminating duplicates. The tracks in the final list are sorted by the number of hits, fewest misses, and lowest χ^2 value. The best track is automatically kept, and the rest of the tracks are examined based on these parameters. Figure 32 shows an example of hits and reconstructed tracks (37).

5.2 Primary Vertex Reconstruction

The primary vertex (PV) is the location of the proton-antiproton hard scatter collision. It is important to identify the position of the PV with high accuracy, since it is an essential ingredient for reconstructing jets, electrons and missing transverse energy. It is also important to select an algorithm (38) which distinguishes between the hard scatter vertex and the vertices from additional *minimum bias*[1] interactions.

---

[1] Additional $p\bar{p}$ interactions per crossing.

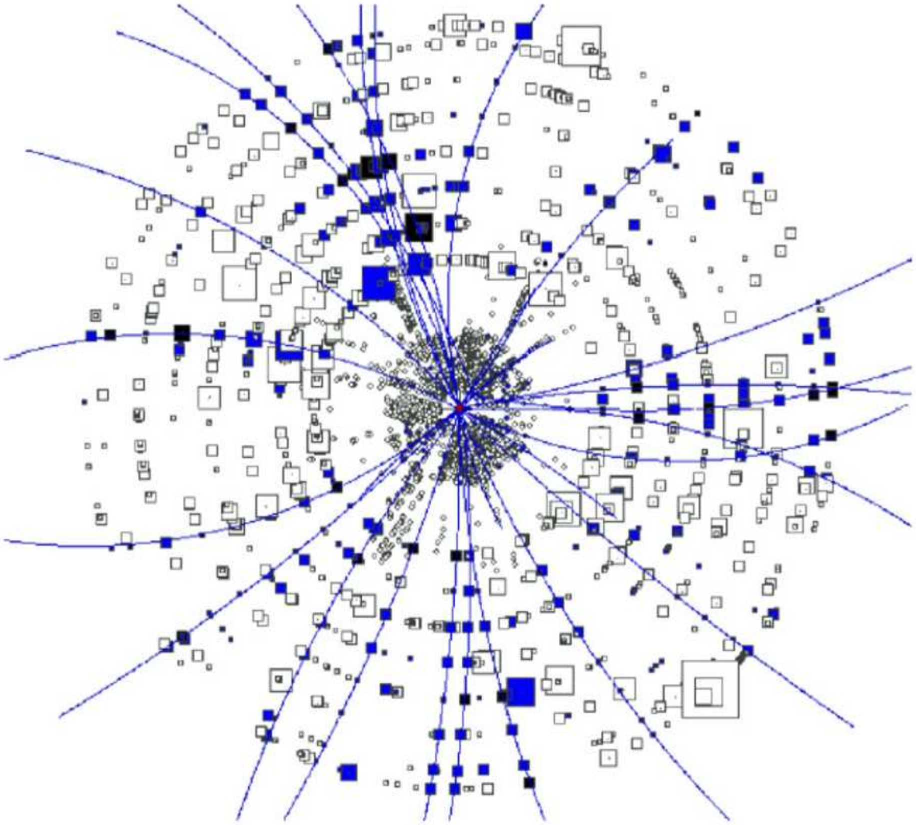

Figure 32. Axial view (looking down the beam-pipe) of a recorded event showing hits and reconstructed tracks. Number of CFT hits are represented by squares, and SMT hits are represented by circles. Hits are colored solid if they are associated with a reconstructed track (solid lines). The curvature of the reconstructed tracks is due to the solenoidal magnetic field, which is pointing out of the page.

Based on the list of reconstructed tracks (see Section 5.1), a list of vertices is generated by extrapolating the tracks back to the z-axis. Clusters of vertices are then formed by selecting vertices within 2 cm of each other along the z-axis. In each vertex cluster, the vertex to which the highest number of tracks point is stored in a list of "selected" vertices. For every selected vertex, nearby tracks are used to compute the probability that the vertex does not come from a MB interaction. The computation of this probability is based on the assumption that tracks coming from MB interactions will have a smaller transverse momentum compared to tracks coming from the hard scatter. Finally, the vertex with the smallest MB probability is chosen as the PV.

5.3 Electromagnetic Object Reconstruction and Identification

Electromagnetic candidate objects (EM objects), such as electrons and photons, are initially identified based on calorimeter information. Since photons do not leave signals in the tracking system, a track matched to the energy deposit in the calorimeter provides a tool to distinguish electrons from photons.

EM object reconstruction begins with the formation of initial calorimeter clusters. Different algorithms can be used to find those initial clusters:

- Simple-Cone tower clustering algorithm ("Scone Method")
- Cell Nearest Neighbor clustering algorithm ("CellNN Method")
- Track extrapolation clustering algorithm ("Road Method").

In this analysis, objects reconstructed with the simple cone algorithm are used.

5.3.1 Simple-Cone Clustering Algorithm

The simple-cone algorithm (39) clusters calorimeter cells based on precision readout data around seeds with E_T >1.5 GeV in a cone of radius $\Delta R = \sqrt{\Delta\eta^2 + \Delta\phi^2} < 0.2$. Additionally, for each cell the ratio of the energy in the EM layers to the total energy (based on CPS, EM, and FH layers) is required to be above 0.9. Next, all clusters satisfying the above criteria are tested for *isolation*:

$$Isolation = \frac{E_{tot}(R < 0.4) - E_{EM}(R < 0.2)}{E_{EM}(R < 0.2)}, \tag{5.1}$$

where $E_{EM}(R < 0.2)$ is the EM energy within a cone of radius $R < 0.2$ (based on EM layers), and $E_{tot}(R < 0.4)$ is the total energy within a cone of radius $R < 0.4$ (based on EM, FH, and CH layers). All initial EM clusters are required to have an isolation of less than 0.2. The isolation parameter gives a measure of how deep and narrow a given cluster is. EM objects tend to deposit most of their energy in a narrow region of the EM layers, while hadrons deposit their energies in the hadronic layers in a much wider radius.

5.3.2 Electromagnetic Object Identification Parameters

Various parameters are calculated for every EM cluster that is formed by the simple-cone algorithm. This gives flexibility when defining EM objects at the analysis stage.

ID: All EM clusters are assigned an ID of 10. If in addition a cluster has a track loosely matched (in η and Φ) to it, it is assigned an ID of ±11 ("+" for electrons, "−" for positrons).

Isolation: An isolation cut of 0.2 is already applied at the reconstruction stage (see Section 5.3.1).

Electromagnetic Fraction: The electromagnetic fraction (EM fraction) discriminates between EM and hadronic calorimeter energy deposits. It takes advantage of the fact that EM showers are almost entirely contained within the EM layers of the calorimeters. EM fraction is defined as:

$$EMfraction = \frac{E_{EM}(R < 0.2)}{E_{tot}(R < 0.2)}, \tag{5.2}$$

where $E_{EM}(R < 0.2)$ is the EM energy within a cone of radius $R < 0.2$ (based on EM layers), and $E_{tot}(R < 0.2)$ is the total energy within a cone of radius $R < 0.2$ (based on EM, FH, and CH layers).

H-Matrix: The H-Matrix distinguishes between EM and hadronic energy deposits, by analyzing the longitudinal and transverse shape of the showers. Based on MC generated electrons, a covariance matrix (M) is defined using a set of seven discriminant variables :

$$M_{ij} = \frac{1}{N}\sum_{n=1}^{N} \; (x_i^n - \langle\; x_i \;\rangle) \; (x_j^n - \langle\; x_j \;\rangle), \tag{5.3}$$

where x_i^n is the value of variable i for electron n, and $\langle\; x_i \;\rangle$ is the mean value of variable i. The seven variables that are used are listed below:

- Shower energy fraction in 1^{st}, 2^{nd}, 3^{rd}, and 4^{th} EM layer of the calorimeter.

- Cluster size in $r - \Phi$ based on the 3^{rd} EM layer of the calorimeter[1].
- Total shower energy.
- Primary vertex position.

The H matrix is defined as the inverse of the covariance matrix M:

$$H \equiv M^{-1}. \tag{5.4}$$

Using the H matrix a χ^2-like variable is calculated that gives a measure of the likelihood that a given shower k is consistent with an EM object shower:

$$\chi^2 = \sum_{ij} \, (x_i^k - \langle \, x_i \, \rangle) \, H_{ij} \, (x_j^k - \langle \, x_j \, \rangle). \tag{5.5}$$

Track Matching: Requiring that a track is associated with a calorimeter EM cluster is a powerful discriminant between electrons and photons. In this analysis *global tracks* are used for tracking confirmation, i.e. tracks based on information from both the CFT and SMT subdetectors. Using calorimeter and tracking information, the following χ^2 variable is calculated:

$$\chi^2 = \left(\frac{\Delta\Phi}{\sigma_\Phi}\right)^2 + \left(\frac{\Delta z}{\sigma_z}\right)^2 + \left(\frac{E_T/p_T - 1}{\sigma_{E_T/p_T}}\right)^2, \tag{5.6}$$

where in Equation 5.6:

---

[1] EM showers typically deposit the bulk of their energy in the 3^{rd} EM layer.

- $\Delta\Phi$ (Δz) is the difference in Φ (z) between the EM cluster position in the 3^{rd} EM calorimeter layer and the extrapolation of the track to the same layer.
- σ_Φ, σ_z, and σ_{E_T/p_T} are the root-mean-squares of the experimental measurements of each quantity.
- E_T/p_T is the ratio of the transverse energy of the EM calorimeter cluster and the transverse momentum of the track.

A track is matched to an EM cluster by requiring that the track matching χ^2 probability is $P(\chi^2) > 10^{-2}$.

5.4 Jet Reconstruction and Identification

Individual quarks and gluons cannot be detected directly due to color confinement. Instead, collimated streams of hadrons (*jets*) are observed in the detector. In this section the techniques that are used to reconstruct and identify jets are discussed.

5.4.1 Jet Cone Algorithm

The *Run II Midpoint Jet Cone Algorithm* is used to reconstruct jets for this analysis (40; 41). The general idea is to define a cone in $\eta \times \Phi$ space, and to group together particles whose trajectories lie within that cone. After choosing an initial trial axis for a cone, the energy-weighted centroid is calculated based on contributions from all particles within the cone. Using the new cone axis, this process is iterated until a “stable” position is found, where the centroid of the energy depositions within the cone is aligned with the geometric axis of the cone.

Input into the algorithm can be based on calorimeter towers, in case the jet reconstruction is performed at the detector level in data or MC. Hadrons (partons) can be used as input at the particle (parton) level in MC.

The following is a description of the Run II Midpoint Jet Cone Algorithm:

1. Only *seed particles* with $p_T^{seed} > 0.5$ GeV are considered for jet reconstruction.
2. Cones are formed based on 4-vector variables (*E-scheme*):

$$p = (E, \mathbf{p}) = \sum_i (E^i, p_x^i, p_y^i, p_z^i,), \tag{5.7}$$

$$p_T = \sqrt{(p_x)^2 + (p_y)^2}, \tag{5.8}$$

$$y = \frac{1}{2} \ln \frac{E + p_z}{E - p_z}, \tag{5.9}$$

$$\Phi = \tan^{-1} \frac{p_y}{p_x} \tag{5.10}$$

   where p is the energy-momentum 4-vector of the cone, and the sum runs over all particles i within a cone of radius 0.5. p, y, and Φ define the centroid for a given cone. Each stable cone is added to a list of *proto-jets*. Only proto-jets with $p_T > 8.0$ GeV are considered.

3. Midpoints between any combination of two proto-jets are also used as seeds and iterated until stable cones are found. This is done to remove sensitivity to soft radiation (Figure 33).
4. The proto-jets are checked for overlapping regions. In order to avoid double counting of energy, a merging/splitting algorithm is applied. Two proto-jets are *merged* if the shared

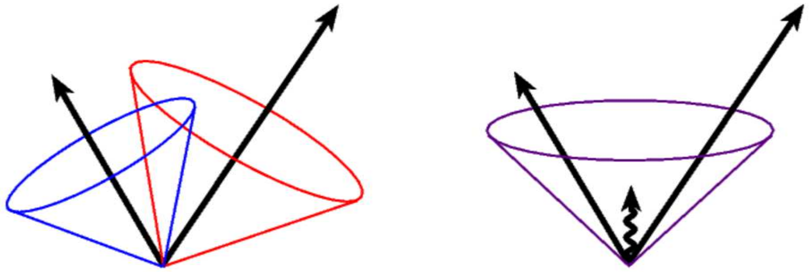

Figure 33. Illustration showing how the presence of soft radiation between two jets may cause a merging of the jets (right) that would not occur in the absence of the soft radiation (left).

energy between them is greater than half of the lower p_T proto-jet. Otherwise, the two proto-jets are *split* and the tower energies are assigned to the closest proto-jet.

5.4.2 Jet Identification Parameters

A set of quality cuts is applied to every reconstructed jet in order to reduce fake jets from calorimeter noise.

EM Fraction (EMF): Hadronic shower formation tends to deposit a significant energy fraction in the hadronic layers of the calorimeter, whereas EM objects mostly shower in the EM layers. Therefore, a cut on the fraction of transverse energy in the EM layers distinguishes jets from EM objects.

Coarse Hadronic Fraction (CHF): Coarse hadronic fraction is the fraction of transverse momentum of a jet that is deposited in the coarse hadronic layers of the calorimeter.

Hot Fraction (HotF): Hot Fraction is the ratio of transverse energy in the most energetic tower to that of the next most energetic tower in the jet. If a significant amount of the total jet energy is originating from a single calorimeter tower, it is likely that the tower is generating artificially high read-out signals due to detector problems (*hot tower*). A cut on the Hot Fraction parameter eliminates jets originating from hot towers.

N90: N90 is the number of towers making up 90% of the jet energy. A cut on the N90 parameter eliminates jets originating from hot towers as well.

L1 Confirmation: L1 confirmation was introduced in order to deal with precision readout noise problems. The jet energy at the L1 trigger tower level is compared with the jet energy derived from the jet cone algorithm, which is based on calorimeter cell precision readout:

$$L1conf = \frac{\sum_{trigger} E_T^i}{p_T^{jet} \cdot (1 - CHF)} \tag{5.11}$$

where $\sum_{trigger} E_T^i$ is the sum of transverse TOT trigger tower energies (with respect to the center of the detector) within $\Delta R < 0.5$ of the reconstructed jet, p_T^{jet} is the transverse momentum of the reconstructed jet (with respect to the reconstructed primary vertex), and CHF is the Coarse Hadronic Fraction of the reconstructed jet.

5.4.3 Jet Energy Scale

The jet energy scale (JES) calibrates the reconstructed energy of the jets to the energy of the jets at the particle (or hadron) level, i.e. before the particles of the jet enter the detector (42). Depending on the jet p_T and jet η, the JES applies a calibration factor to obtain the particle level jet energy ($E_{jet}^{particle}$) from the measured jet energy ($E_{jet}^{calorimeter}$) according to the following relation:

$$E_{jet}^{particle} = \frac{E_{jet}^{calorimeter} - E_{offset}}{R_{jet} \cdot R_{cone}} \tag{5.12}$$

where E_{offset} is the *offset energy* within a jet, R_{jet} is the *jet response* correction, and R_{cone} is the *out of cone showering* correction.

Offset Energy: Energy contributions that are not related to the physics processes that are responsible for creating a jet are subtracted from the measured jet energy. The offset energy term contains contributions from multiple interactions, underlying event energy, electronic noise, uranium noise, and pile-up from previous bunch crossings.

Jet Response: This contribution measures the calorimeter response of the hadronic particles and the amount of energy within a jet that is lost due to uninstrumented regions and dead material in the calorimeter.

Out of Cone Showering: This parameter corrects for energy losses (gains) due to calorimeter showering effects from particles located inside (outside) of the particle jet.

Figure 34 shows the overall jet energy scale corrections as a function of jet E and η.

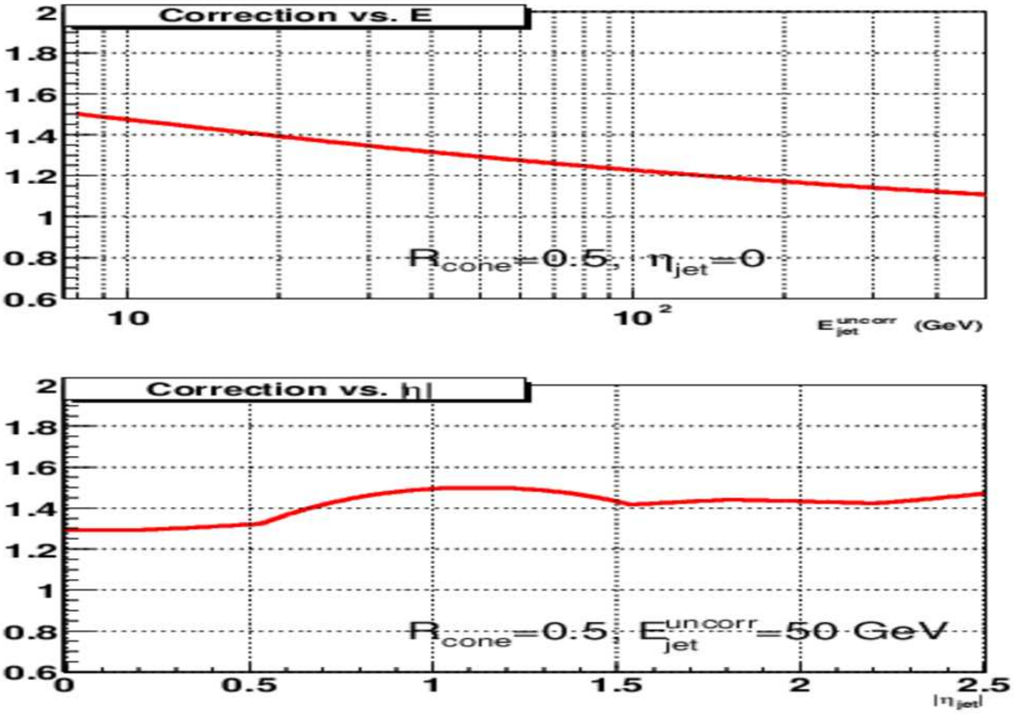

Figure 34. The jet energy scale correction factor measured for jets in data as a function of E (top) and η (bottom).

CHAPTER 6

MONTE CARLO EVENT SIMULATION

Event generator programs are an essential tool in particle physics with the goal to simulate nature as accurately as possible (43; 44). In particle physics, event generators aim to include all stages of interactions that occur at high energy collisions including the initial creation of partons in hadronic collisions (*parton level*), followed by parton showering from initial and final state partons and subsequent hadronization (*particle* or *hadron level*), and simulations of all detector elements (*detector level*). The output of MC simulations can be used to test theoretical predictions, to estimate efficiencies and acceptances, to study background processes, and to correct data for detector effects so that direct comparisons to theoretical predictions can be made.

This chapter gives a description of the MC simulation tools and techniques that were used in this analysis.

6.1 The PYTHIA Event Generator

PYTHIA is a general purpose MC event generator (45) which describes many physical aspects of a typical high-energy event:

1. The initial beam particles, such as protons and antiprotons, are characterized by PDFs.

2. One parton from each initial particle radiates through a *Bremsstrahlung*-like process, such as $q \to qg$, to initiate a sequence of branchings which build up an initial-state "shower" (*Initial State Radiation*, or ISR).
3. Two partons participate in the *hard process* which produces a number of outgoing particles. PYTHIA is optimized for hard processes that have two particles in the initial and final states, such as $q\bar{q} \to Z/\gamma^* \to e^+e^-$ ($2 \to 2$ *process*).
4. Final state particles can also radiate to initiate a final-state shower (*Final State Radiation*, or FSR).
5. Initial and final-state color coherence effects are incorporated via the Angular Ordering approximation.
6. The remaining partons (*spectators*) in the two incoming hadrons may interact.
7. Beam remnant interactions are taken into account.
8. Outgoing quarks and gluons form color neutral hadrons following the string hadronization model.
9. Many of the produced hadrons are unstable and decay further.

In order to describe inclusive $Z/\gamma^* \to e^+e^-$ events, an inclusive PYTHIA sample based on the $q\bar{q} \to Z/\gamma^* \to e^+e^-$ LO hard process is used. ISR and FSR parton showering provides QCD corrections to LO. Based on the DGLAP splitting equations, which give the probability for a parton to radiate, or branch, the final state parton shower is evolved from the scale Q down to a cut-off scale Q_0 where it terminates. At this scale, α_s becomes large and perturbation theory breaks down. At that stage the colored partons are converted into colorless hadrons by the hadronization process. PYTHIA uses a phenomenological model known as the *String Model* to describe this process. As a color-confined quark-antiquark pair moves out in opposite directions, the color field between them collapses into a string-like configuration, where each string has a uniform energy per unit length, and the potential energy in the string increases as the quarks move apart. Once the potential becomes energetically favorable another $q\bar{q}$ pair is pulled from the vacuum, and the string split into two. This process continues until only on mass-shell hadrons remain.

6.2 Combining Matrix Elements with Showering

PYTHIA produces multijet events by incorporating 2→2 hard processes with parton showering that is subsequently interfaced with the string hadronization model. Since parton showers are only approximations of soft parton radiation in the limits of low p_T and small emission angles (*soft* and *collinear limits*), final states with several high p_T and well separated jets are not properly described. Such final states occur frequently at the Tevatron due to the large momentum transfer, Q^2. In order to give a more accurate description of such processes, matrix element generators are combined with parton shower simulations by dividing phase space into two regions, separated by a p_T *matching threshold*. In the high p_T region, jet production relies on matrix elements; the low p_T region is described by the parton showering simulation. Exact bookkeeping is necessary when combining the two regions in order to avoid the double counting of parton configurations (46; 47).

6.2.1 Combining ALPGEN with PYTHIA

In order to describe inclusive $Z/\gamma^* \rightarrow e^+e^- + \geq n$ jet events ($n \geq 1$), the tree-level matrix element generator ALPGEN (48; 49) is used. ALPGEN was designed to simulate specific SM processes in hadronic collisions, emphasizing large jet multiplicities in the final state. ALPGEN calculates parton level final states to lowest order in perturbation theory. The ALPGEN output is interfaced with PYTHIA for showering and hadronization.

6.2.2 Combining MADGRAPH with PYTHIA

MADGRAPH (50) is a tree-level matrix element generator, and it is based on specifying initial and final state particles for any tree level SM process. It creates a list of all relevant Feynman diagrams and calculates the corresponding matrix elements. The program is able to calculate matrix elements for any SM process. The only limitation is processing power[1]. The MADGRAPH output is interfaced with PYTHIA for showering and hadronization.

The matching between MADGRAPH and PYTHIA to avoid double counting when combining different multiplicity final states is done following a modified CKKW prescription (51; 52; 53). These samples are referred to as *CKKW samples*.

6.3 The MCFM Monte Carlo Simulation

MCFM (*Monte Carlo for FeMtobarn processes*) (54; 55; 56) can calculate parton level cross sections for $Z/\gamma^*(\rightarrow e^+e^-)$ at NLO in α_s for up to two partons in the final state.

---

[1] At present MADGRAPH is limited to 10,000 diagrams per subprocess, corresponding to $W+$ 5 jets.

6.4 The DØ Detector Simulation

After all final state particles are generated, detector effects can be simulated with a simulation package called D0GSTAR (*D0 GEANT Simulation of the Total Apparatus Response*) (57). D0GSTAR is based on the CERN package GEANT (*GEometry ANd Tracking*) (58) which simulates the passage of particles through matter. Effects such as ionization, showering, and the magnetic field interaction in the DØ detector are modeled. The output of this simulation has the same format as the real data recorded by the detector. The full event reconstruction applied to real data can also be applied to the simulation output for direct comparisons.

CHAPTER 7

DATA AND MONTE CARLO SAMPLES

This chapter gives a description of the data and MC samples in Sections 7.1 and 7.2. Event selection criteria are discussed in Section 7.3. Section 7.4 compares basic properties of electrons and jets between data and MC.

7.1 Data Sample

The data sample used for this analysis was collected between April 2002 and June 2004 and contains approximately 876 million events. The raw data are processed with the p14 version of the DØ reconstruction software. A calorimeter noise suppression algorithm (T42 (59)) is applied. In order to create a final data sample of manageable size, pre-selection or *skimming* criteria are used:

EM1TRK skimming Each event in the data set is required to have at least one EM object with ID = 10 or ±11, $p_T > 8$ GeV, and a track with $p_T > 5$ GeV within $\Delta\phi = 0.1$ of the EM object. These requirements reduce the size of the data sample to approximately 57 million events.

Root-tuple creation The reconstructed data are reformatted into an object oriented ntuple format (*root-tuple*) using the ATHENA (60) software package (version p16-br-03). At this stage, JES corrections (version 5.3) are applied.

Root-tuple skimming The root-tuple data are further skimmed by requiring at least one EM object with EM fraction > 0.9, Isolation< 0.15, H-Matrix(7)< 12.0, $|\eta_{det}| < 1.1$ and a track match[1] in each event. The final analysis root-tuple contains 2.4 million events.

Data flagged as unusable by data-quality experts are excluded from the analysis. SMT, CFT, calorimeter, and luminosity subsystems of the detector are required to be fully operational. Additionally, all data taking periods with limited L1CAL trigger coverage ($|\eta| < 0.8$) are excluded (61).

Events for the analysis are selected based on the requirement that the trigger system identified at least one EM object (*single electron triggers*). Only *unprescaled* single electron triggers were used. When the trigger conditions implemented in the trigger list were not providing the required reduction in event rate, *prescaling factors* were applied. For example, if a prescaling factor of 3 is applied to a given L1 trigger, then only one out of three proton-antiproton bunch crossings is considered for evaluation by the trigger system.

The data taking period for this analysis can be divided into two periods during which different lists of single EM triggers were implemented. The following is the prioritized order of trigger combinations for trigger lists before *global_CMT-12* (runs ≤ 178732, "pre-v12 dataset")[2] (62):

- EM_HI_SH or EM_HI_2EM5_SH

---

[1] χ^2 probability for best track using the distance in η/Φ and E/p

[2] The statement "Trigger A or Trigger B" refers to the fact that a given event is accepted if Trigger A and Trigger B are unprescaled, and the trigger requirements for either Trigger A or Trigger B are met.

- EM_HI_SH
- EM_HI
- EM_MX_SH
- EM_MX,

The trigger combinations for trigger list *global_CMT-12* (runs ≥ 178722, "v12 dataset") are:

- E1_SHT20 or E2_SHT20 or E3_SHT20 or E1_SH30
- E1_SHT20 or E2_SHT20 or E1_SH30
- E1_SHT20 or E1_SH30
- E1_SHT20,

Table I contains details of the individual triggers.

A total integrated luminosity of 343 pb^{-1} was available for this analysis after trigger selection and exclusion of unusable data due to bad quality.

7.2 Monte Carlo Samples

7.2.1 PYTHIA and ALPGEN Samples

The MC samples used for data comparisons and acceptance estimations are summarized in Table II. For studies regarding the inclusive $Z/\gamma^* \to e^+e^-$ cross section, a PYTHIA $Z/\gamma^* \to e^+e^-$ inclusive sample is used. For higher jet multiplicities, events are generated with ALPGEN and then passed through PYTHIA for parton showering and hadronization.

The electron energy resolution measured in data is not correctly modeled by the MC simu-

Trigger	L1	L2	L3
EM_HI_SH	CEM(1,10)	EM(1,12)	ELE_LOOSE_SH_T(1,20)
EM_HI_2EM5_SH	CEM(2,5)	EM(1,12)	ELE_LOOSE_SH_T(1,20)
EM_HI	CEM(1,10)	EM(1,12)	ELE_LOOSE(1,30)
EM_MX_SH	CEM(1,15)	none	ELE_LOOSE_SH_T(1,20)
EM_MX	CEM(1,15)	none	ELE_LOOSE(1,30)
E1_SHT20	CEM(1,11)	none	ELE_NLV_SHT(1,20)
E2_SHT20	CEM(2,6)	none	ELE_NLV_SHT(1,20)
E3_SHT20	CEM(1,9)CEM(2,3)	none	ELE_NLV_SHT(1,20)
E1_SH30	CEM(1,11)	none	ELE_NLV_SH(1,30)

L1 Triggers

CEM(1,10)	one EM trigger tower with $E_T > 10$ GeV
CEM(2,5)	two EM trigger towers with $E_T > 5$ GeV
CEM(1,15)	one EM trigger tower with $E_T > 15$ GeV
CEM(1,11)	one EM trigger tower with $E_T > 11$ GeV
CEM(2,6)	two EM trigger towers with $E_T > 6$ GeV
CEM(1,9)CEM(2,3)	one EM trigger tower with $E_T > 9$ GeV, another EM trigger tower with $E_T > 3$ GeV

L2 Triggers

EM(1,12)	one EM candidate with $E_T > 12$ GeV (not present for runs before 169524)

L3 Triggers

ELE_LOOSE_SH_T(1,20)	one electron with $\lvert\eta\rvert < 3.0$ and $E_T > 20$ GeV passing loose requirements including shower shape cuts
ELE_LOOSE(1,30)	one electron with $\lvert\eta\rvert < 3.0$ and $E_T > 30$ GeV passing loose requirements
ELE_NLV_SHT(1,20)	one electron with $\lvert\eta\rvert < 3.6$ and $E_T > 20$ GeV passing tight shower shape cuts
ELE_NLV_SH(1,30)	one electron with $\lvert\eta\rvert < 3.6$ and $E_T > 30$ GeV passing loose shower shape cuts

TABLE I

SINGLE EM TRIGGERS USED IN THIS ANALYSIS.

Process	Generators	Size
$Z/\gamma^* \rightarrow e^+e^-$	PYTHIA	400k
$Z/\gamma^* j \rightarrow e^+e^- j$	ALPGEN + PYTHIA	150k
$Z/\gamma^* jj \rightarrow e^+e^- jj$	ALPGEN + PYTHIA	180k
$Z/\gamma^* jjj \rightarrow e^+e^- jjj$	ALPGEN + PYTHIA	15k

TABLE II

LIST OF MONTE CARLO SAMPLES

lation. Additional energy smearing is applied to the MC electrons to account for the difference. p_x, p_y, p_z and energy of the electrons are multiplied by $c \cdot \text{Gauss}(1, f)$, where Gauss(1,$f$) is the additional smearing parameter which is chosen from a Gaussian distribution with mean 1 and width f, and c is an overall calibration factor. The following values for the smearing parameters are used (63):

- f = 0.045
- c = 1.003,

We also adjust the jet energy resolution in MC to match the jet resolution in data (64). The parameterization of the jet energy resolution is given by:

$$\frac{\sigma(p_T)}{p_T} = \sqrt{\frac{N^2}{p_T^2} + \frac{S^2}{p_T} + C^2}, \tag{7.1}$$

where the constants C, S, and N represent the gain fluctuations, sampling fluctuations, and noise contributions respectively. Table III summarizes all coefficients for different detector

Coefficient	$\lvert\eta_{det}\rvert < 0.5$	$0.5 < \lvert\eta_{det}\rvert < 1.0$	$1.0 < \lvert\eta_{det}\rvert < 1.5$	$\lvert\eta_{det}\rvert > 1.5$
N_{data}	5.05	$9.06 \cdot 10^{-9}$	2.24	6.42
S_{data}	0.753	1.2	0.924	$4.5 \cdot 10^{-10}$
C_{data}	0.0893	0.087	0.135	0.0974
N_{MC}	4.26	4.61	3.08	4.83
S_{MC}	0.658	0.621	0.816	$5.13 \cdot 10^{-7}$
C_{MC}	0.0436	0.0578	0.0729	0.0735

TABLE III

JET ENERGY RESOLUTION PARAMETERS (DATA AND MC).

regions. Figure 35 and Figure 36 show the jet p_T resolutions for different η_{det} regions in data and MC, respectively.

Using the p_T and η_{det} of the MC jets, the data and MC resolutions are calculated. If the data resolution is better than the MC resolution for a given jet, no additional smearing is applied. If the jet resolution in MC is worse than in data, the MC jet energy resolution is adjusted by applying a multiplicative smearing factor (Equation 7.2) to the 4-vector components of each jet.

$$\text{Smearing Factor} = \text{Gauss}\left(1, \sqrt{\left(\frac{\sigma(p_T)}{p_T}\right)^2_{data} - \left(\frac{\sigma(p_T)}{p_T}\right)^2_{MC}}\right) \tag{7.2}$$

7.2.2 CKKW Samples

Table IV summarizes the CKKW samples used in the analysis. The samples use a matching threshold of $p_T > 15$ GeV (51). Partons are generated with $|\eta| < 2.5$. The Z boson has a generated mass between 75 GeV and 105 GeV. The matrix element generation with MADGRAPH

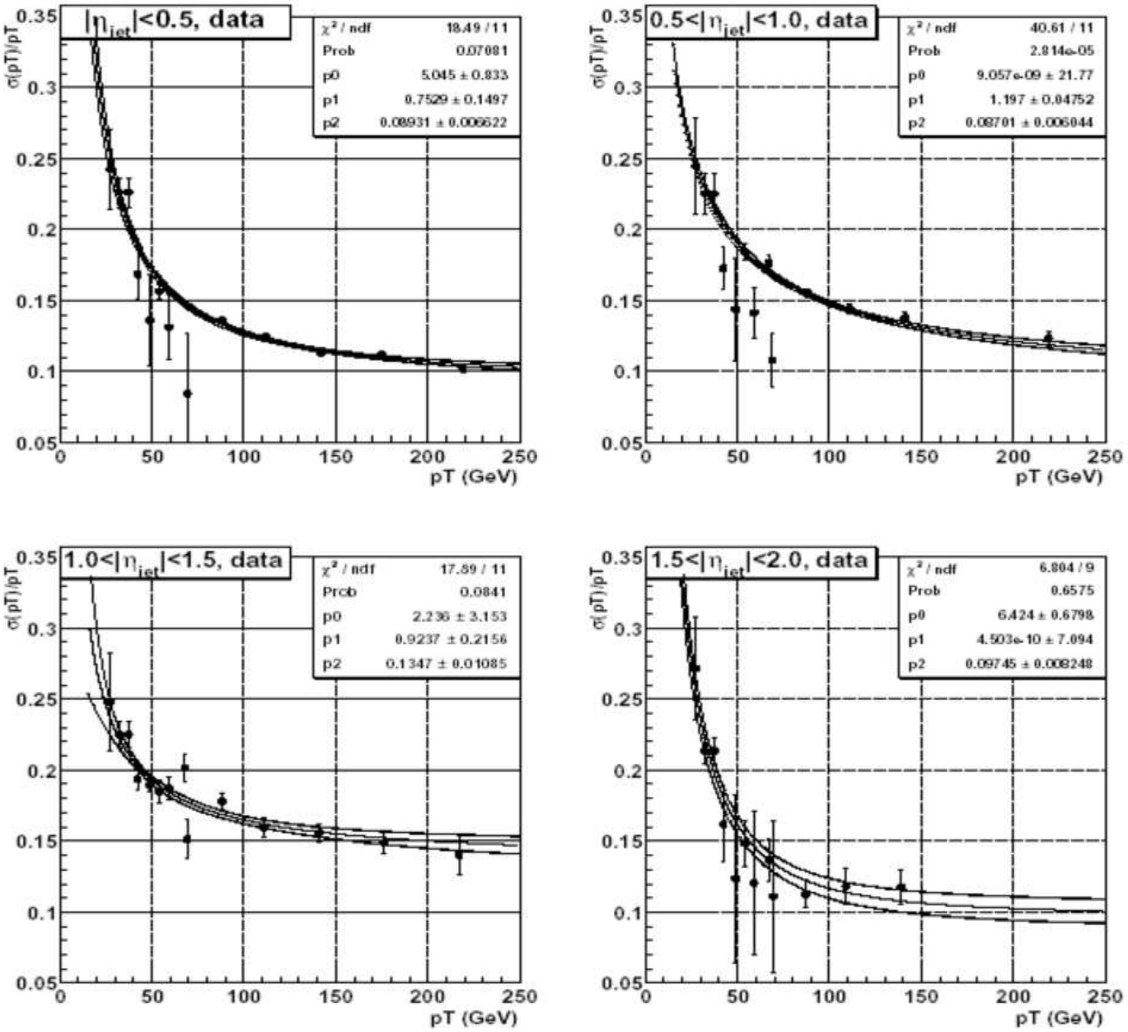

Figure 35. Jet p_T resolutions for different η_{det} regions in data (JES 5.0 with T42).

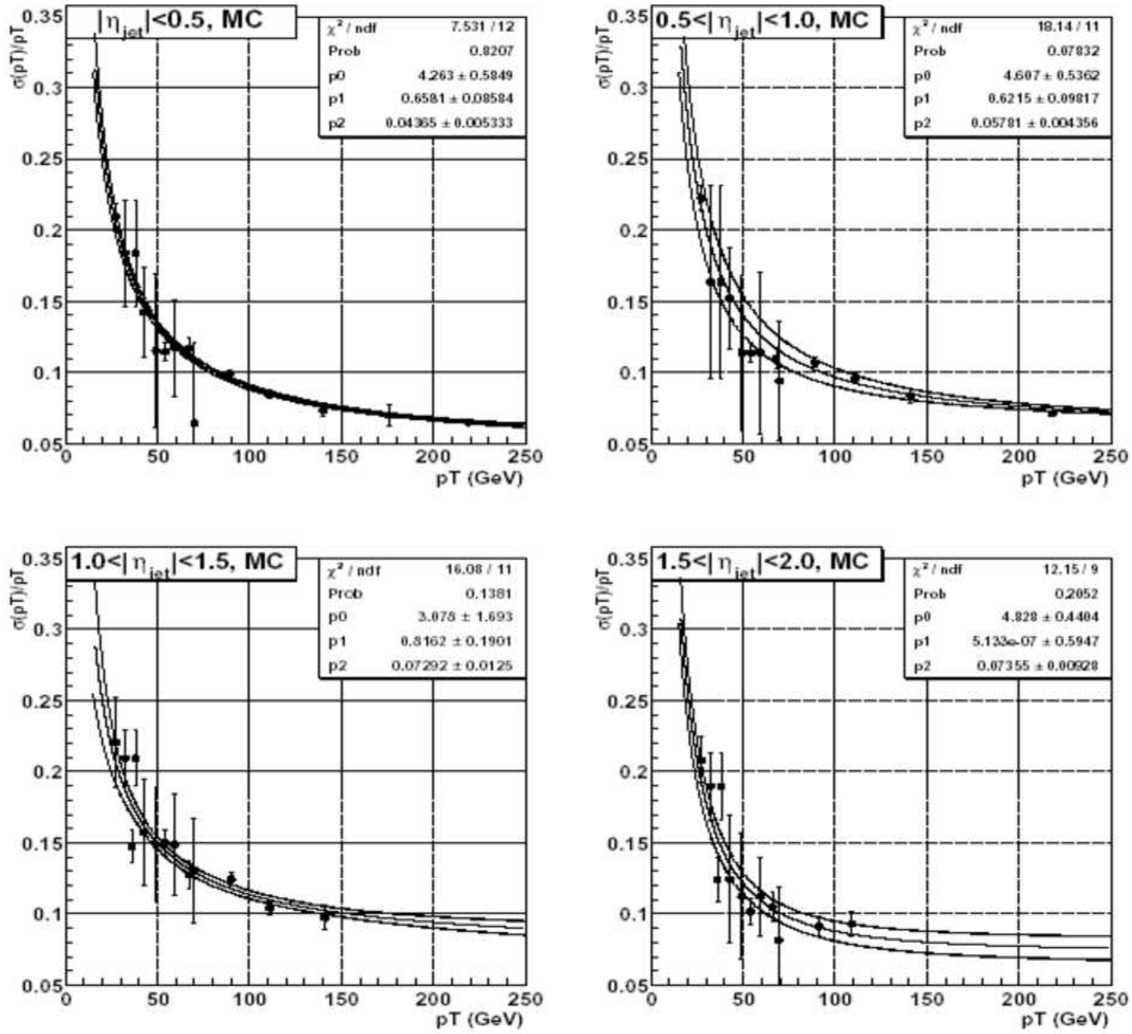

Figure 36. Jet p_T resolutions for different η_{det} regions in MC (JES 5.0 with T42).

was done up to jet multiplicities of 3. Higher jet multiplicities are from parton showering simulated by PYTHIA. The factorization scale is set to $\mu_F^2 = M_Z^2$. The renormalization scale is set to $\mu_R^2 = p_{Tjet}^2$ for jets from initial state radiation and $\mu_R^2 = k_{Tjet}^2$ for jets from final state radiation.

Process	Generators	Size
$Z/\gamma^* j \rightarrow e^+e^- j$	MADGRAPH + PYTHIA	234k
$Z/\gamma^* jj \rightarrow e^+e^- jj$	MADGRAPH + PYTHIA	20k
$Z/\gamma^* jjj \rightarrow e^+e^- jjj$	MADGRAPH + PYTHIA	3k

TABLE IV

LIST OF CKKW SAMPLES

7.2.3 MCFM Cross Sections

MCFM inclusive cross sections are calculated to NLO for up to 2 partons. The kinematic and geometric jet cuts are the same as used in the analysis: parton $p_T > 20$ GeV, $|\eta| < 2.5$. The Z boson has a mass between 80 GeV and 100 GeV, and CTEQ6M was selected for the PDF. The renormalization and factorization scales are set to $\mu_{F/R}^2 = M_Z^2 + p_{TZ}^2$.

7.3 Event Selection

The following selection criteria are applied in order to assure that events with two high p_T electrons contained within the central calorimeter and originating from the decay of a Z/γ^*

gauge boson are selected. After identifying the *Z candidate* events, the presence of $n > 0$ high p_T jets is required.

7.3.1 Primary Vertex

The efficiency to reconstruct the PV is $\approx 100\%$ in the central region of the detector, and decreases outside of the SMT fiducial volume. Therefore, the PV is required to be within 60 cm of the detector center along the beam pipe (z-axis).

7.3.2 Electron Selection

EM objects have to satisfy the following requirements:

- Loose electrons:
  - ID = 10 or ±11
  - EM Fraction > 0.9
  - Isolation < 0.15
  - H-Matrix(7) < 12
  - $p_T > 25$ GeV
  - $|\eta_{det}| < 1.1$.
- Tight electrons:
  - Requirements of loose electron.
  - Track match[1] with $P(\chi^2) > 0.01$.

---

[1] χ^2 probability for best track using the distance in η/Φ and E/p

7.3.3 Z Selection

Z candidates are selected based on the following criteria:

- Two loose electrons.
- At least one of the two electrons needs to be tight.
- One of the two electrons must have fired the trigger[1].
- Diem invariant mass window cut: 75 GeV $< M_{ee} <$ 105 GeV.

7.3.4 Jet Selection

Jets are formed using the Run II Midpoint Jet Cone Algorithm with a cone size of 0.5 and are selected based on the following criteria:

- $0.05 <$ EMF < 0.95
- HotF < 10.
- N90 > 1.
- CHF < 0.4
- L1 confirmation
- JES corrected $p_T > 20$ GeV
- $|\eta_{physics}| < 2.5$

---

[1] Matching trigger objects at L1, L2, and L3 within $\Delta R < 0.4$ are required.

Sample	N	Fraction
$Z/\gamma^* + 0$ jets	12,247	0.8815
$Z/\gamma^* + 1$ jets	1,427	0.1027
$Z/\gamma^* + 2$ jets	189	0.0136
$Z/\gamma^* + 3$ jets	25	0.0018
$Z/\gamma^* + 4$ jets	3	0.0002
$Z/\gamma^* + 5$ jets	2	0.0001
Total	13,893	1.0000

TABLE V

EVENT BREAKDOWN BY EXCLUSIVE JET MULTIPLICITIES ASSOCIATED WITH Z/γ^* PRODUCTION BEFORE ANY BACKGROUND IS SUBTRACTED OR ANY CORRECTIONS ARE APPLIED.

- Since the jet algorithm identifies *fake* jets originating from electron energy deposits, all jets overlapping with electrons coming from the Z/γ^* boson within $\Delta R = \sqrt{\Delta\eta^2 + \Delta\phi^2}$ of 0.4 are removed.

7.3.5 Event Statistics

Table V summarizes the number of $Z/\gamma^* \rightarrow e^+e^-$ event candidates for different exclusive jet multiplicities.

7.4 Data vs Monte Carlo

This section presents a comparison of basic kinematic distributions for electrons, Z candidates, and jets between data and MC simulations[1]. It is important that the MC distributions

---

[1] The MC distributions are normalized to the number of events in data.

describe the data distributions as accurately as possible. The MC simulations are used to account for the fraction of events that are lost due to kinematic and geometric electron cuts, the diem invariant mass cut, and the primary vertex cut (*acceptance*).

7.4.1 Primary Vertex Comparison

Figure 37 compares the primary vertex distribution between data and inclusive $Z/\gamma^* \rightarrow e^+e^-$ PYTHIA MC.

7.4.2 Z p_T Comparisons

Figure 38 shows the Z p_T comparison between data and inclusive $Z/\gamma^* \rightarrow e^+e^-$ PYTHIA MC. Since PYTHIA is a LO ($2 \rightarrow 2$) generator at the hard process, there is disagreement in the Z p_T distribution (especially at high p_T) between data and MC. To account for this discrepancy, an additional correction based on the Z p_T comparison between data and MC is applied to the MC events. The Z p_T correction is also shown inFigure 38.

Figure 39 and Figure 40 show Z p_T comparisons when using ALPGEN + PYTHIA for Z+1 jet and Z+2 jet samples. The agreement between ALPGEN + PYTHIA MC and data is deemed acceptable. Therefore, no additional Z p_T correction is applied to the ALPGEN + PYTHIA MC samples.

7.4.3 Z/γ^* ($\rightarrow e^+e^-$) + $\geq n$ Jet Comparisons

7.4.3.1 Z/γ^* ($\rightarrow e^+e^-$) Inclusive Sample

In this section, basic kinematic distributions for electrons and Z candidates are compared after applying all corrections (Trigger, EM, Tracking, Z p_T - see Chapters 8.1 and 9.1 for a description of the corrections). Figure 41 compares basic electron and Z kinematic distributions.

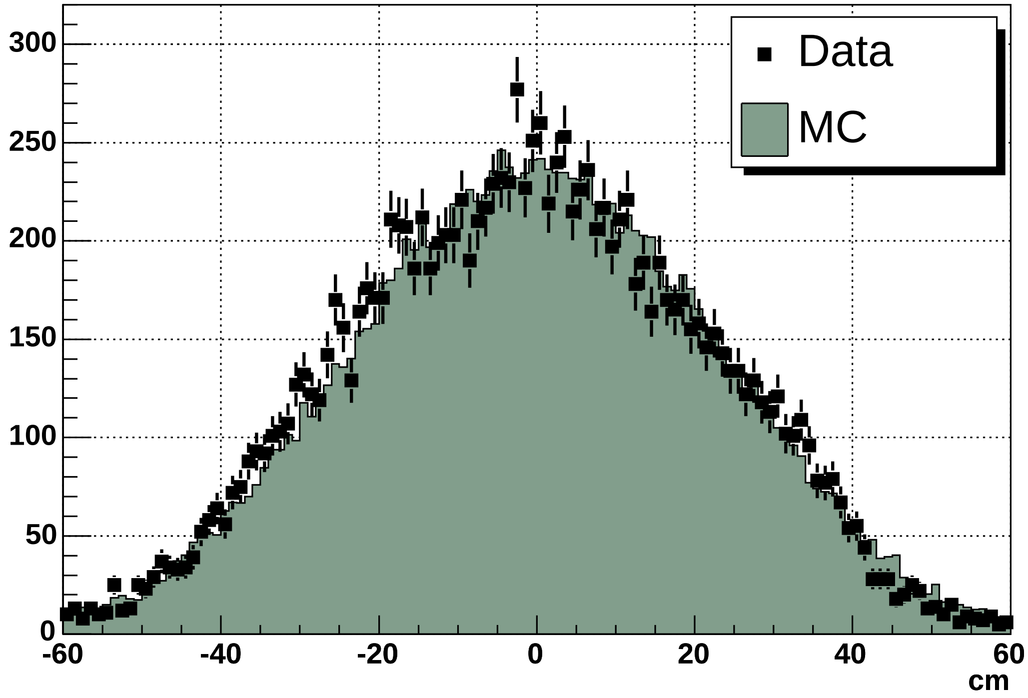

Figure 37. Primary vertex distribution in data and MC (PYTHIA) for the inclusive sample. The MC distribution is normalized to the number of events in data.

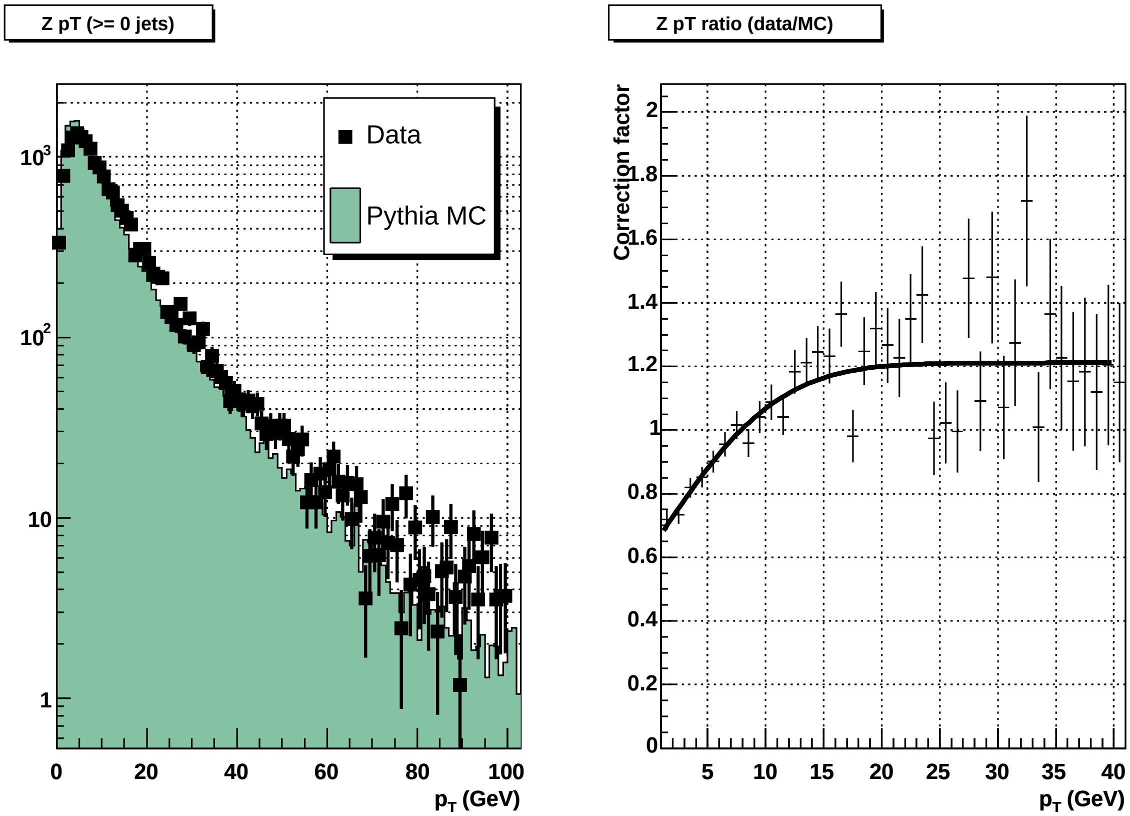

Figure 38. Comparison of Z p_T between data and PYTHIA MC (left), and ratio correction factor (right) for the inclusive sample. The MC distribution (left) is normalized to the number of events in data.

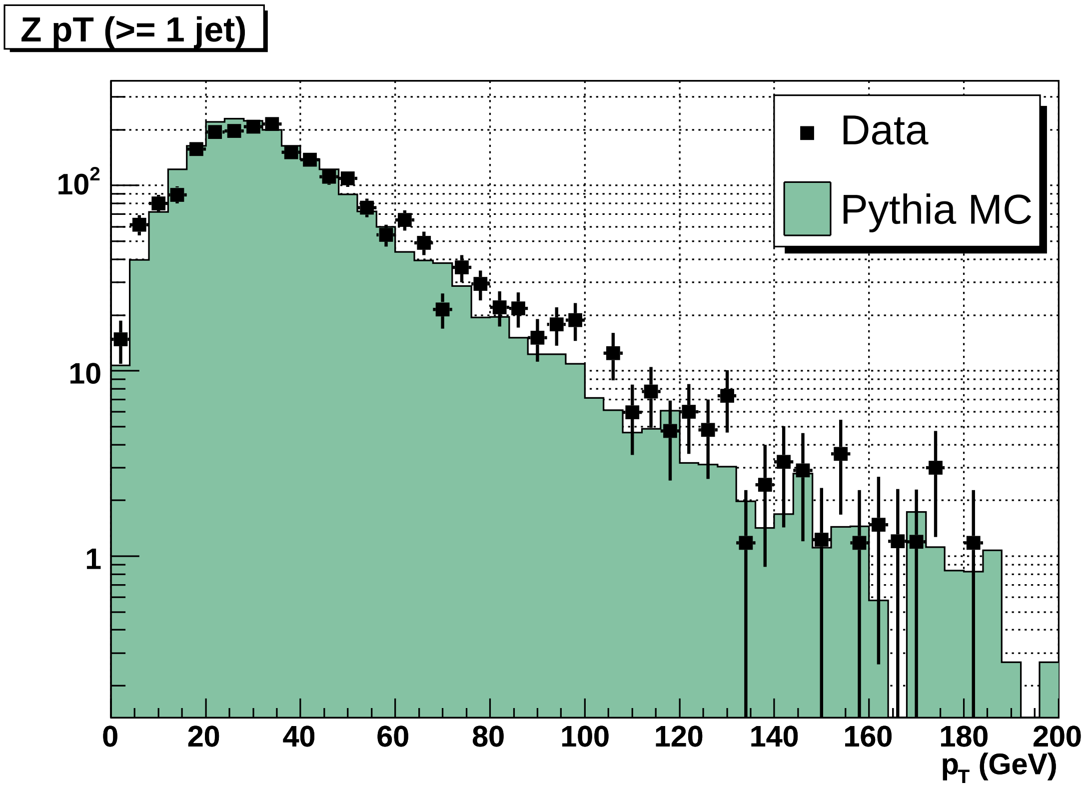

Figure 39. Comparison of Z p_T between data and ALPGEN + PYTHIA Z+1 jet MC. MC is normalized to the number of events in data.

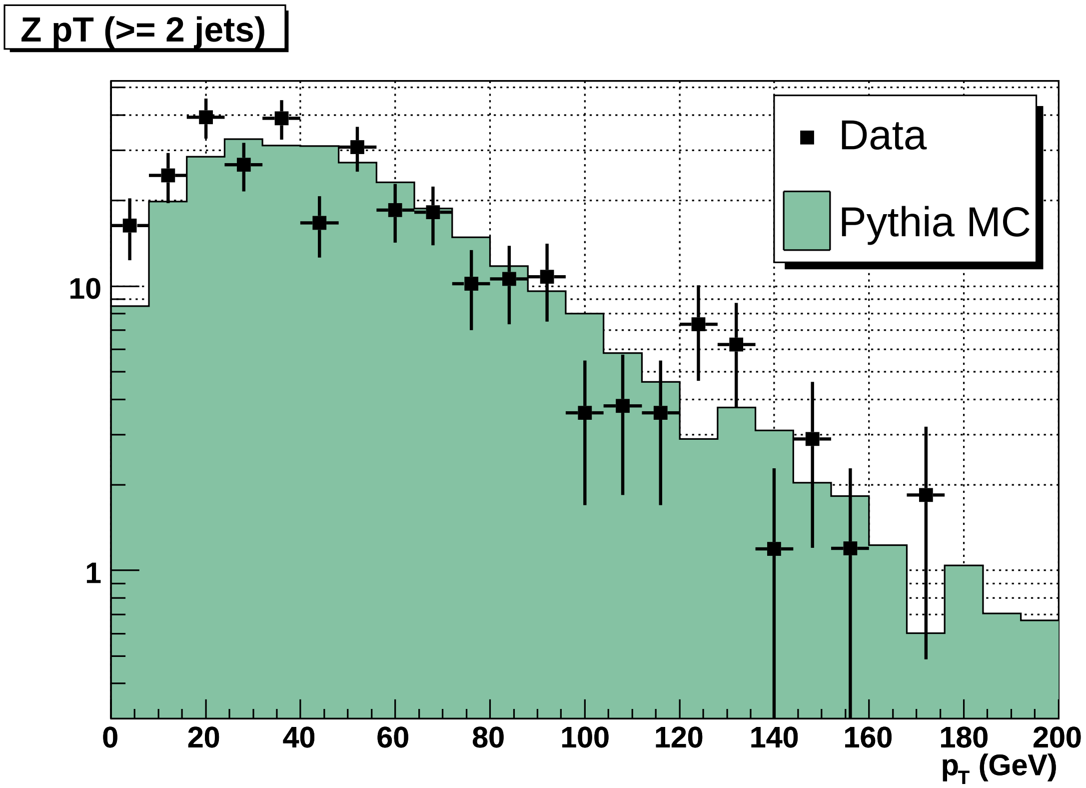

Figure 40. Comparison of Z p_T between data and ALPGEN + PYTHIA Z+2 jets MC. MC is normalized to the number of events in data.

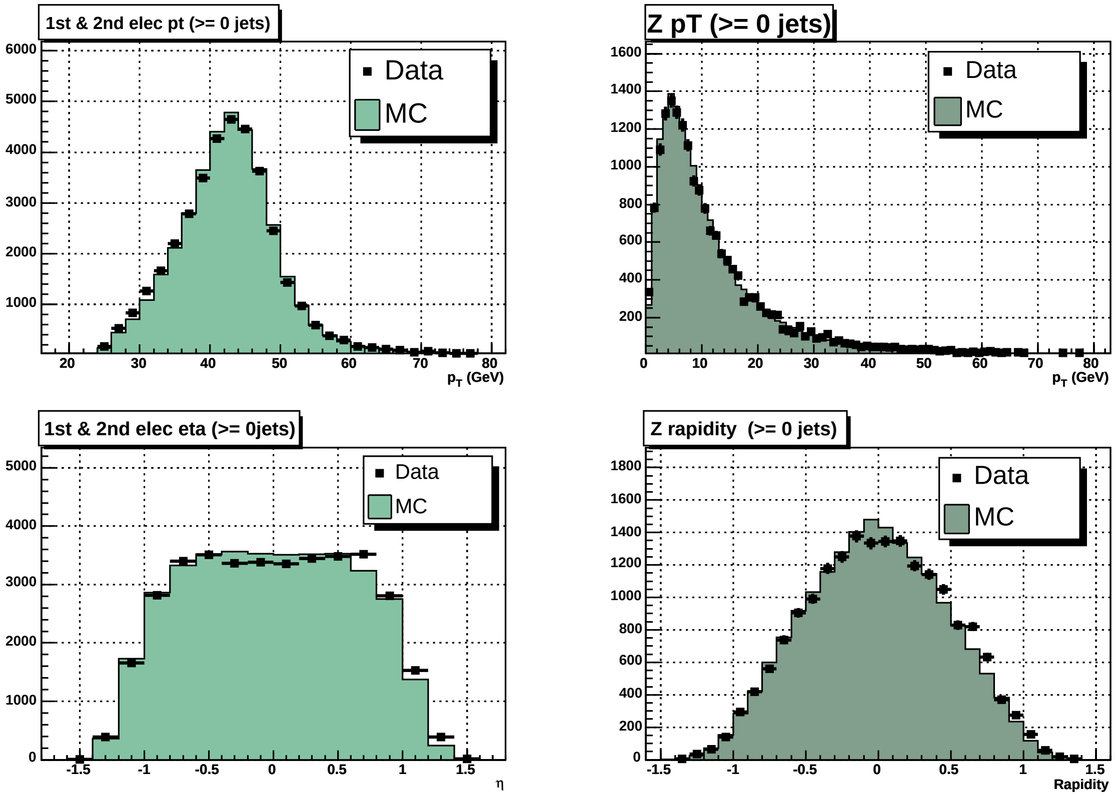

Figure 41. pT of both Z electrons (top left), physics η of both Z electrons (bottom left), Z p_T (top right), Z rapidity (bottom right) for the $Z/\gamma^* \rightarrow e^+e^-$ inclusive sample in data and MC (PYTHIA). The MC distribution is normalized to the number of events in data.

Figure 42 compares the diem invariant mass distribution. The average Z mass is 91.02 GeV with a width of 4.03 GeV.

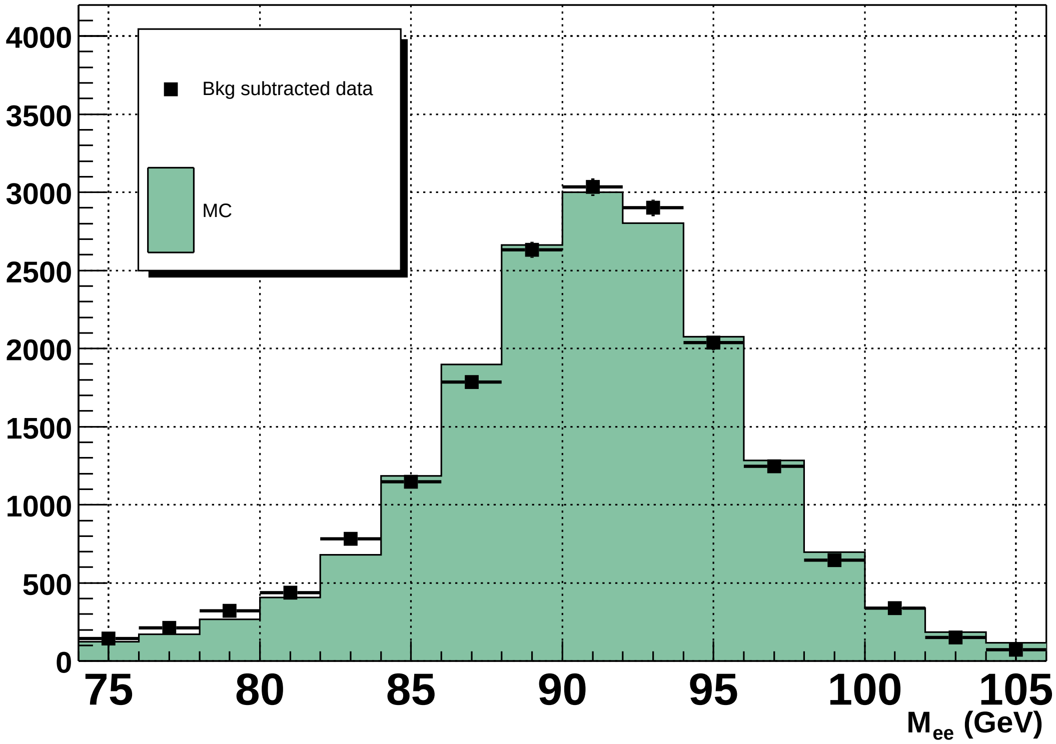

Figure 42. Diem invariant mass comparison for the $Z/\gamma^* \to e^+e^-$ inclusive sample in data and MC (PYTHIA). Data are background subtracted. The MC distribution is normalized to the number of events in data.

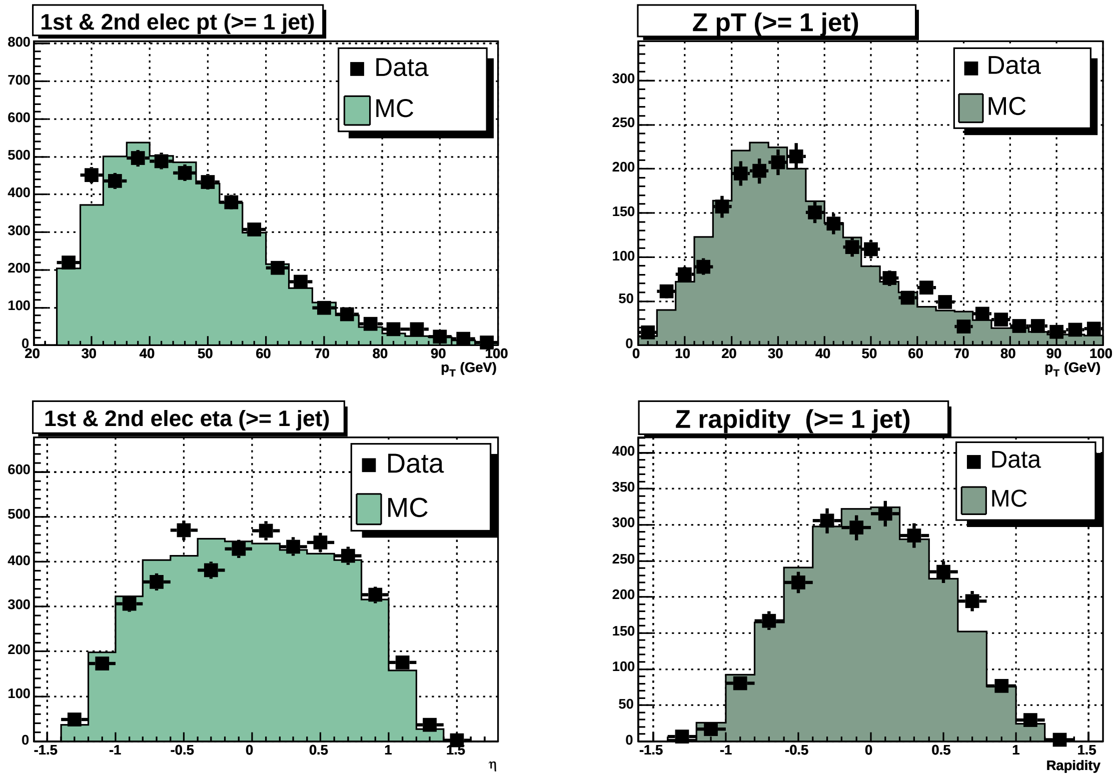

Figure 43. pT of both Z electrons (top left), physics η of both Z electrons (bottom left), Z p_T (top right), Z rapidity (bottom right) for the $Z/\gamma^* \rightarrow e^+e^-+ \geq 1$ jet sample in data and MC (ALPGEN). The MC distributions are normalized to the number of events in data.

7.4.3.2 Z/γ^* ($\rightarrow e^+e^-$) $+ \geq 1$ Jet Sample

Figure 43 shows comparisons of basic electron and Z distributions. Figure 44 shows a comparison of the diem invariant mass peak. Figure 45 and Figure 46 show comparisons of basic kinematic distributions for jets.

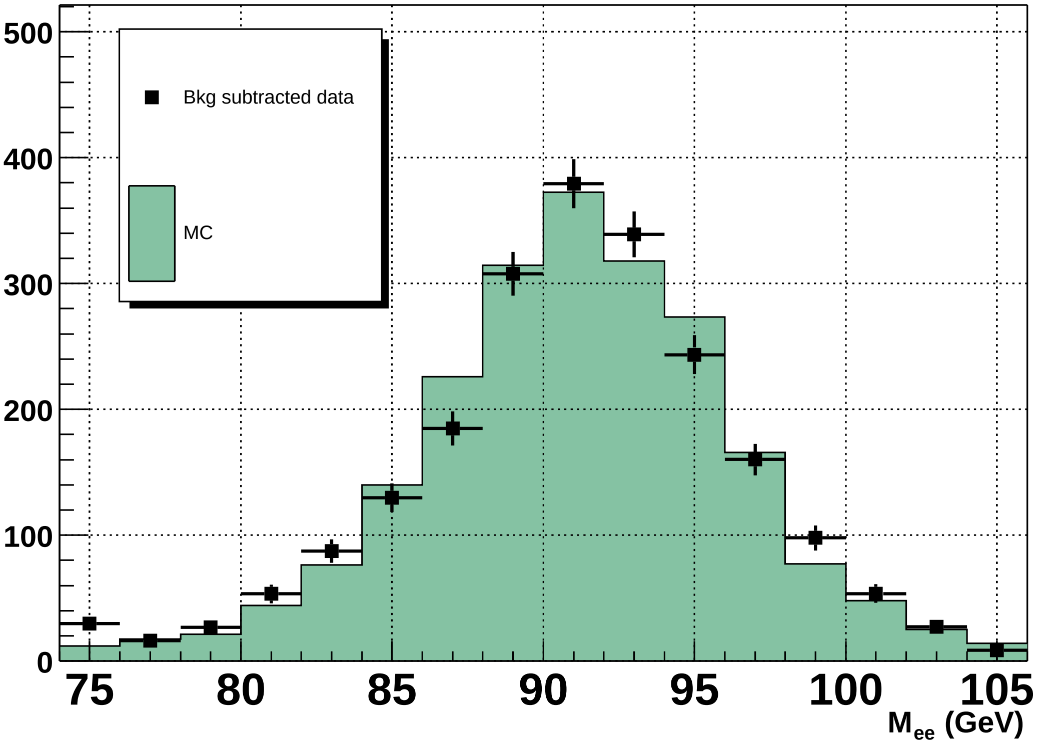

Figure 44. Diem invariant mass comparison for the $Z/\gamma^* \to e^+e^- + \geq 1$ jet sample in data and MC (ALPGEN). Data are background subtracted. The MC distribution is normalized to the number of events in data.

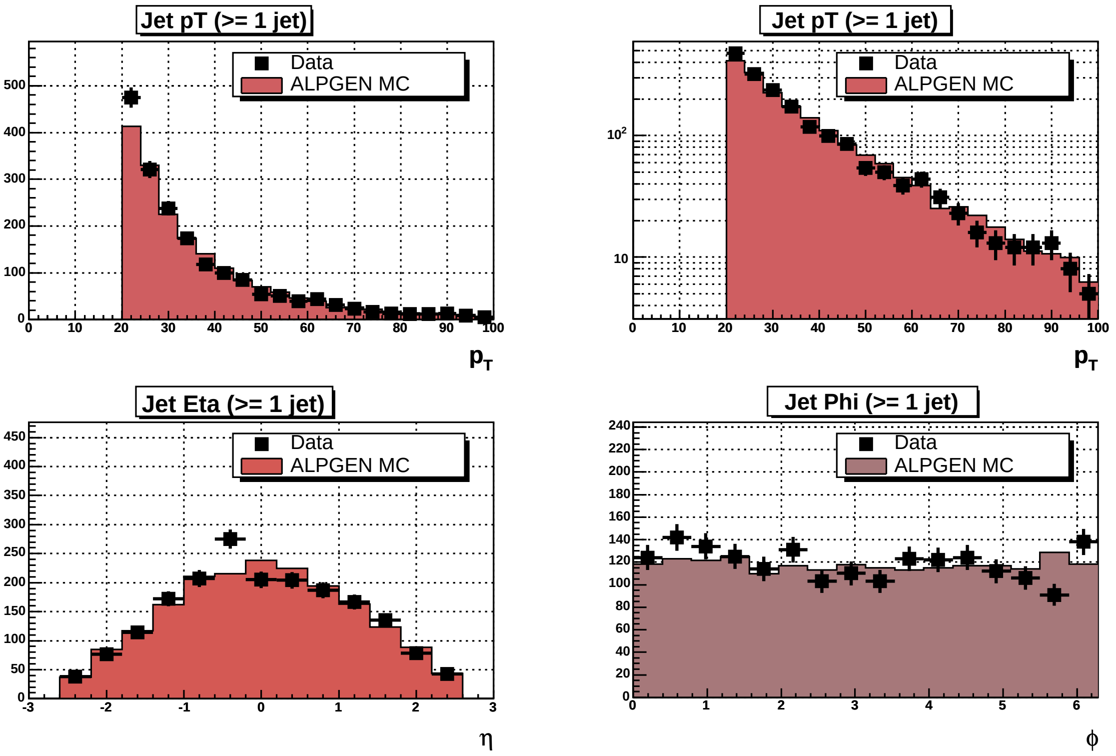

Figure 45. p_T (linear and logarithmic), physics η and physics Φ of all jets for the $Z/\gamma^* \rightarrow e^+e^- + \geq 1$ jet sample in data and MC (ALPGEN). The MC distributions are normalized to the number of events in data.

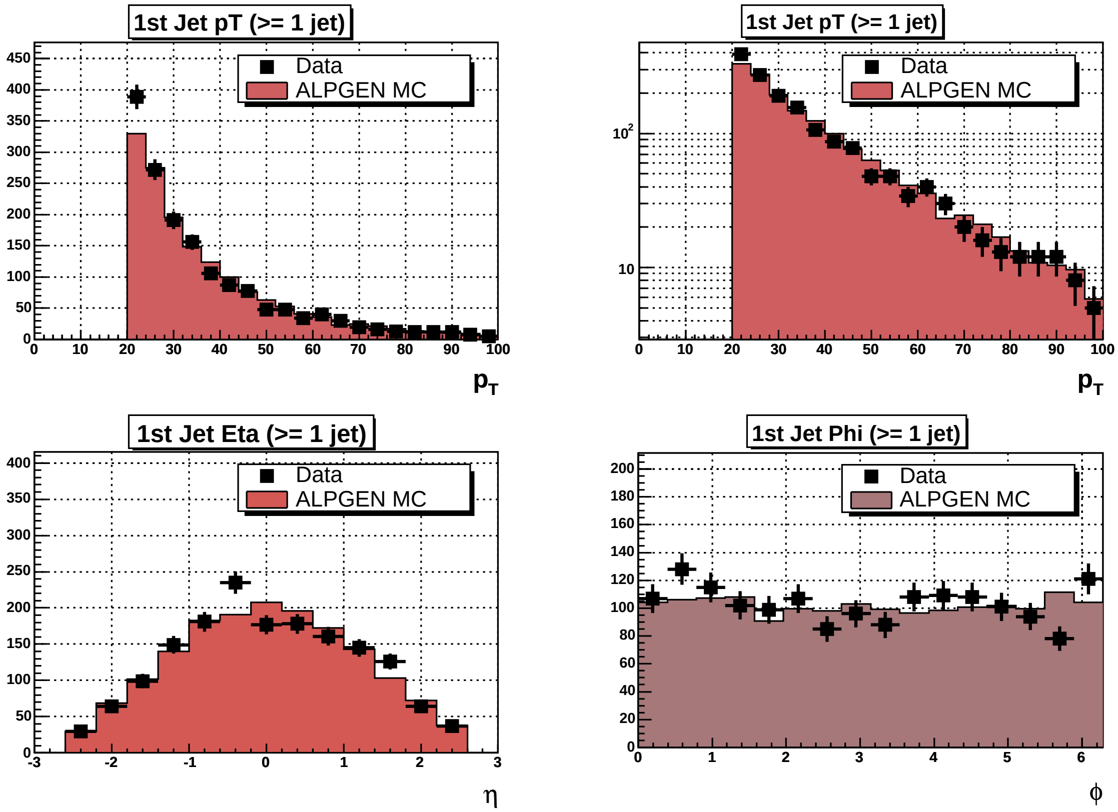

Figure 46. p_T (linear and logarithmic), physics η and physics Φ of the leading p_T jet for the $Z/\gamma^* \to e^+e^- + \geq 1$ jet sample in data and MC (ALPGEN). The MC distributions are normalized to the number of events in data.

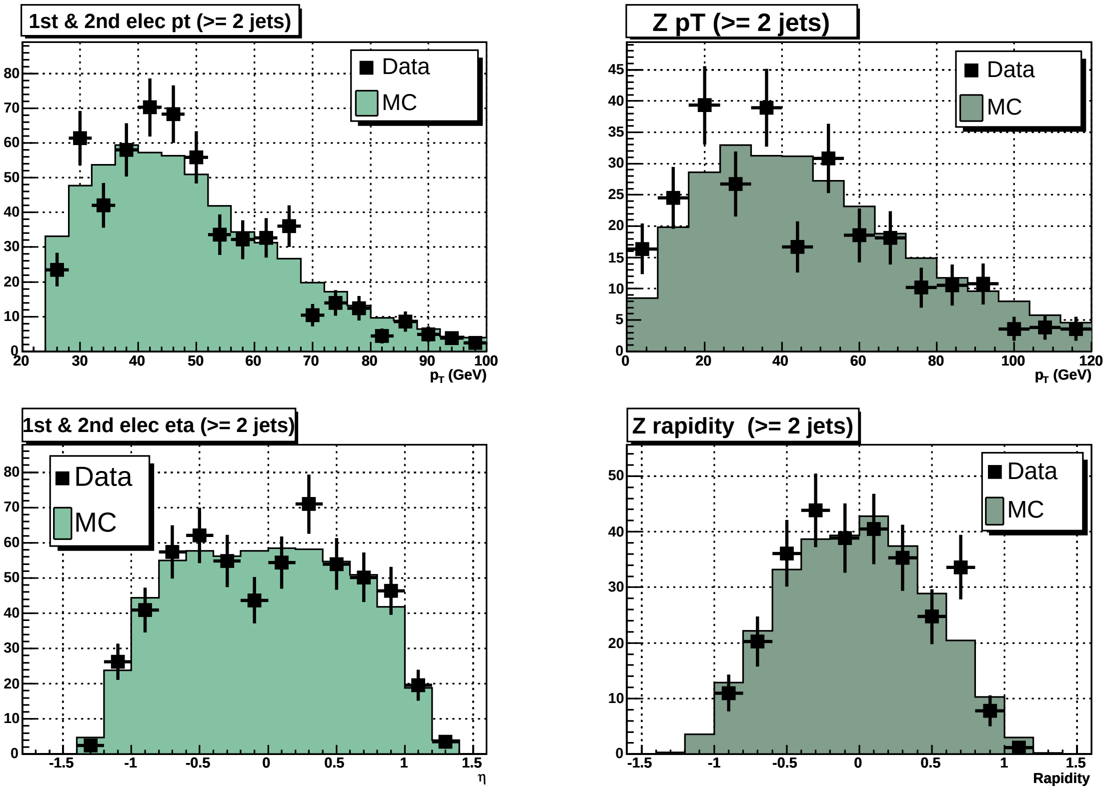

Figure 47. pT of both Z electrons (top left), physics η of both Z electrons (bottom left), Z p_T (top right), Z rapidity (bottom right) for the $Z/\gamma^* \to e^+e^- + \geq 2$ jet sample in data and MC (ALPGEN). The MC distributions are normalized to the number of events in data.

7.4.3.3 Z/γ^* $(\to e^+e^-)$ + $\geq$ 2 Jet Sample

Figure 47 shows comparisons of basic electron and Z distributions. Figure 48 shows a comparison of the diem invariant mass peak and Figure 49, Figure 50 and Figure 51 show comparisons of basic kinematic distributions for jets.

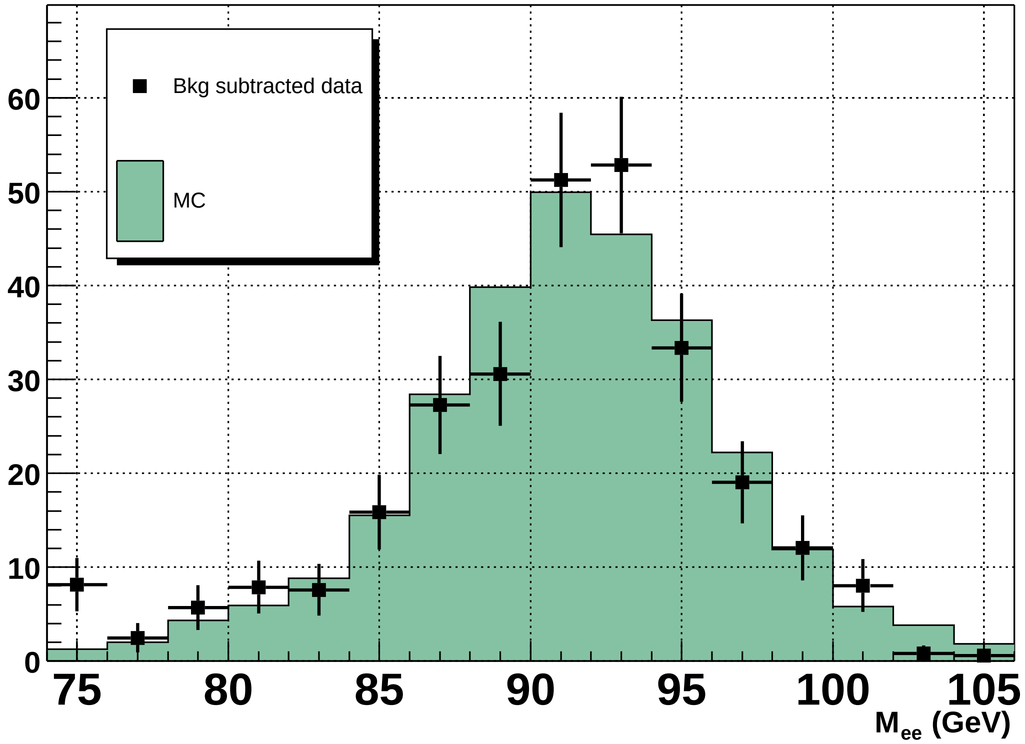

Figure 48. Diem invariant mass comparison for the $Z/\gamma^{*} \rightarrow e^{+}e^{-}+ \geq 2$ jet sample in data and MC (ALPGEN). Data are background subtracted. The MC distribution is normalized to the number of events in data.

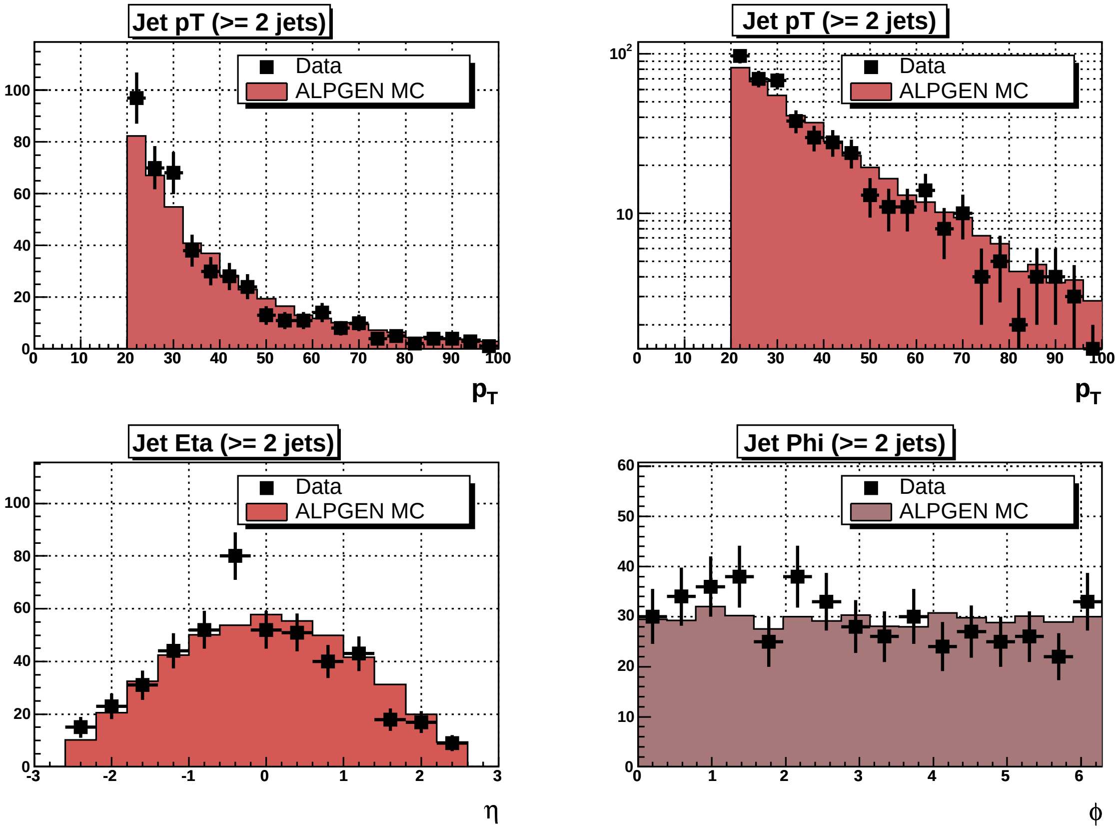

Figure 49. p_T (linear and logarithmic), physics η and physics Φ of all jets for the $Z/\gamma^* \rightarrow e^+e^- + \geq 2$ jet sample in data and MC (ALPGEN). The MC distributions are normalized to the number of events in data.

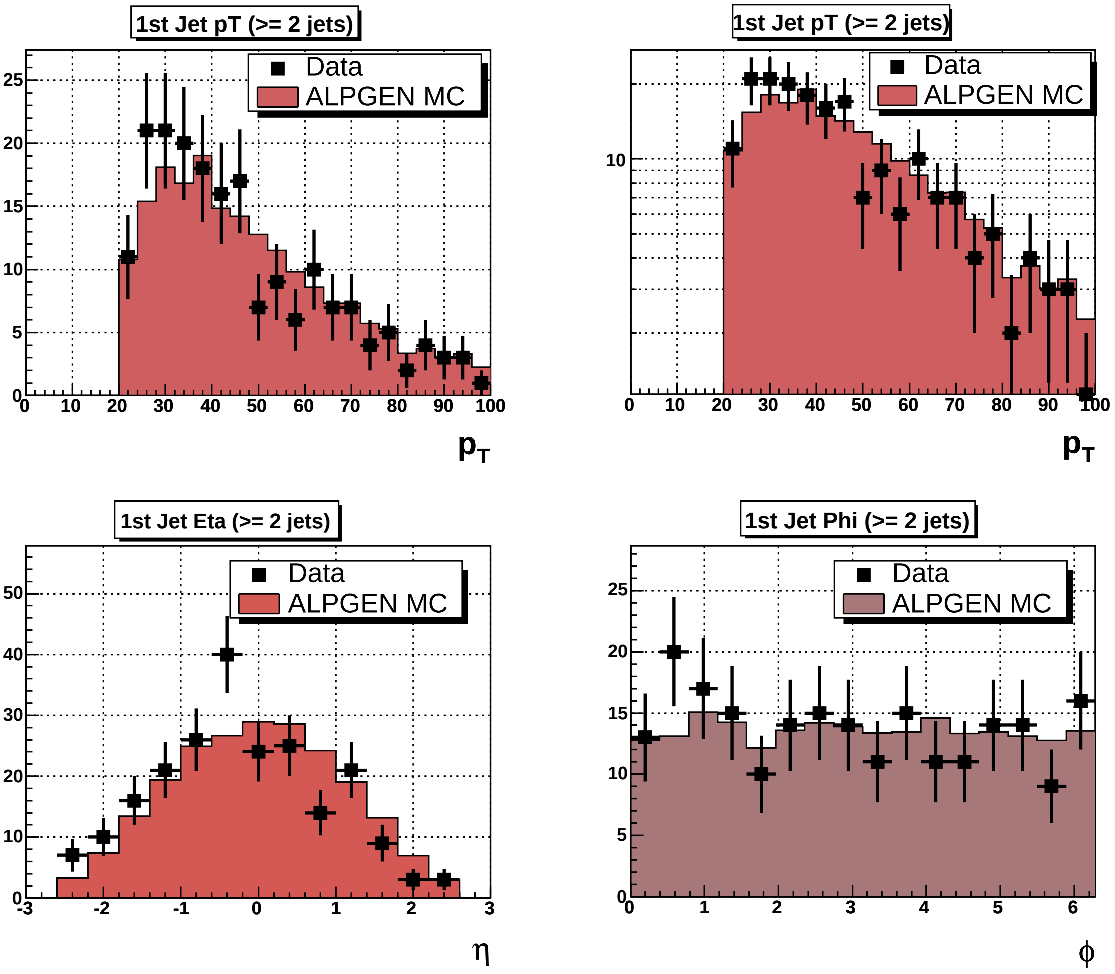

1st Jet pT (>= 2 jets)

1st Jet pT (>= 2 jets)

1st Jet Eta (>= 2 jets)

1st Jet Phi (>= 2 jets)

Figure 50. p_T (linear and logarithmic), physics η and physics Φ of the leading p_T jet for the $Z/\gamma^* \rightarrow e^+e^- + \geq 2$ jet sample in data and MC (ALPGEN). The MC distributions are normalized to the number of events in data.

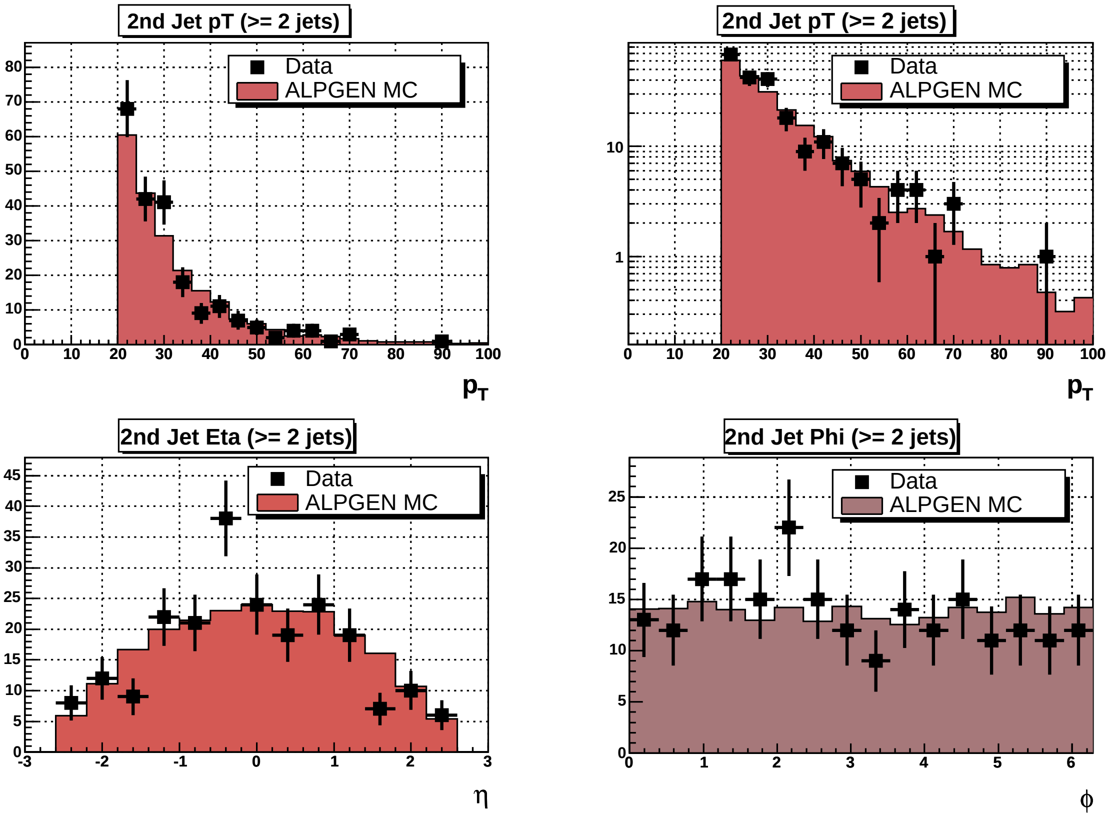

Figure 51. p_T (linear and logarithmic), physics η and physics Φ of the second leading p_T jet for the $Z/\gamma^* \rightarrow e^+e^- + \geq 2$ jet sample in data and MC (ALPGEN). The MC distributions are normalized to the number of events in data.

CHAPTER 8

MEASUREMENT OF THE $\mathbf{Z}/\gamma^*(\rightarrow \mathbf{e}^+\mathbf{e}^-)$ INCLUSIVE CROSS SECTION

The $Z/\gamma^*(\rightarrow e^+e^-)$ inclusive cross section is measured to provide a basic cross check for some of the techniques used in the final measurement of the $Z/\gamma^*(\rightarrow e^+e^-)+\geq n$ jet cross sections. In order to determine the inclusive cross section times branching fraction into electrons, the following equation is evaluated:

$$\sigma \times \mathrm{BR}(Z/\gamma^* \rightarrow e^+e^-) = \frac{N - B}{\mathcal{L} \times \varepsilon_{tot} \times A}, \tag{8.1}$$

where N and B are the total number of events and number of background events in the diem invariant mass range, respectively; $\mathcal{L}$ is the total integrated luminosity of the data sample (343 pb^{-1}); A is the *acceptance*, i.e. the efficiency of the kinematic and geometric electron cuts, the diem invariant mass cut and the primary vertex cut; and ε_{tot} is the total efficiency to identify e^+e^- pairs resulting from Z/γ^* decays. ε_{tot} can be further factorized according to:

$$\varepsilon_{tot} = \varepsilon_{trigger} \cdot \varepsilon_{EM} \cdot \varepsilon_{track}, \tag{8.2}$$

where $\varepsilon_{trigger}$ is the efficiency of the event to have at least one electron to pass all trigger levels, ε_{EM} is the efficiency of reconstructing two EM clusters which pass all electron ID cuts, and ε_{track} is the efficiency of requiring at least one EM cluster to match with a track. Practically, all efficiencies are applied as corrections to the diem invariant mass distribution.

The primary source of background to Z/γ^* decays is from QCD multi-jet production in which the jets have a large electromagnetic component or are mismeasured in such a way that the jets pass the electron selection criteria. The shape of the QCD background in the diem invariant mass distribution follows an exponential form. This is determined by examining the diem invariant mass distribution of EM object pairs that were selected by applying "anti-electron cuts" to assure that two jets with high electromagnetic energy content in the shower are selected:

- All criteria that are applied to loose electron candidates as described in Section 7.3.2 except for the H-Matrix cut.
- H-Matrix(7) > 35
- Two of these objects per event.

The goal is to measure the cross section for diem pairs where both γ^* (*Drell-Yan*) and Z boson exchange contribute. Contributions from pure Z boson decays will show up as a peak around the Z mass at ≈ 91 GeV in the diem invariant mass distribution. The Drell-Yan component follows an exponential distribution.

The following section describes the determination of the efficiencies (trigger, EM reconstruction and identification, EM-Track match) and acceptance.

8.1 Efficiencies

8.1.1 Trigger Efficiency

The combined trigger efficiency per electron is determined with a *tag-and-probe method* using Z candidate events with invariant mass between 70 and 110 GeV. For this method, both Z candidate electrons are considered as possible "tags". An electron becomes a "tag" if it passes trigger requirements for at least one unprescaled trigger in the trigger combination. To pass the requirements of a trigger, an electron must have a matching trigger object at each level which passes all cuts for the corresponding trigger. Both the tag and probe electrons must satisfy the following requirements:

- $p_T > 20$ GeV
- EM Fraction > 0.9
- Isolation < 0.15
- H-Matrix(7) < 12
- Track match with $P(\chi^2) > 0.01$.

The probe electron must have matching trigger objects at L1, L2 and L3 within $\Delta R = \sqrt{\Delta\eta^2 + \Delta\phi^2}$ of 0.4.

Trigger efficiencies are parameterized versus EM object p_T and derived separately for pre-v12 and v12 data. In cases where the L2 subsystem was not operative (all runs before 169,524), only L1 and L3 trigger objects were used. Figure 52 shows the parameterized trigger efficiencies for both datasets.

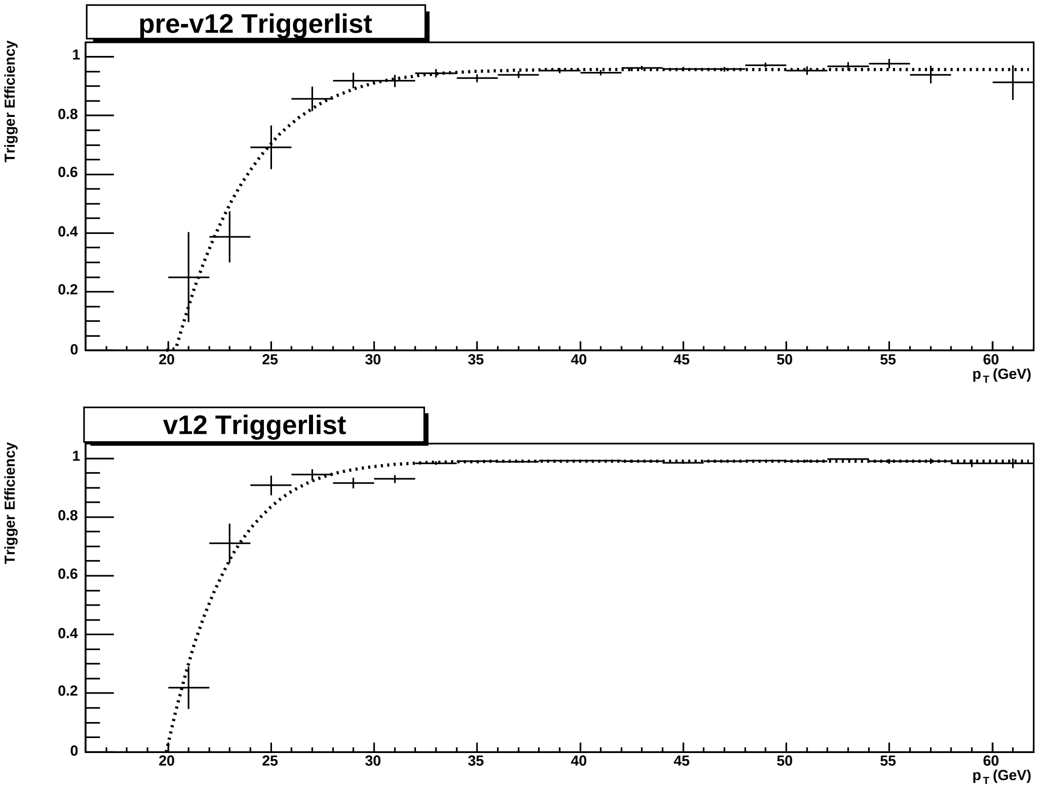

Figure 52. Trigger efficiencies for pre-v12 (top) and v12 (bottom) datasets vs EM object p_T
.

The average trigger efficiencies per electron for the pre-v12 and v12 datasets are (with statistical uncertainties):

- $\varepsilon^{electron}_{pre-v12}(\text{Trigger}) = 94.6\% \pm 0.3\%$
- $\varepsilon^{electron}_{v12}(\text{Trigger}) = 98.2\% \pm 0.1\%$.

The event trigger efficiency is calculated in the following way:

- In a given event the trigger efficiency curves are used to determine the trigger efficiencies ε_1 and ε_2 for the two EM objects (based on their p_T).
- To calculate the event based trigger efficiency, all permutations for the two EM objects to fire a trigger are taken into account:

$$\varepsilon_{trigger}^{event} = \varepsilon_1 \cdot (1-\varepsilon_2) + \varepsilon_2 \cdot (1-\varepsilon_1) + \varepsilon_1 \cdot \varepsilon_2 = \varepsilon_1 + \varepsilon_2 - \varepsilon_1 \cdot \varepsilon_2. \tag{8.3}$$

8.1.2 EM Reconstruction and Identification Efficiency

To determine EM efficiencies, a tag and probe method is used. The tag leg consists of an electron candidate, and the probe leg consists of a track. The tag electron has to pass all the loose electron selection cuts, have a matched track and satisfy trigger requirements for the event. Both tag and probe tracks have to satisfy the following selection criteria (65):

- Stereo track[1]
- 25 GeV $< p_T <$ 80 GeV
- χ^2 probability for best track < 8 (using the distance in η/Φ and E/p)
- Distance of closest approach between track and beam position in the R-Φ plane < 0.3 cm
- Δz_{vertex} of the two tracks < 4 cm
- $|\eta_{detector}| < 1.1$.

---

[1] Requiring hits in stereo layers of the tracking system (see Chapter 3.3.2).

Tag electron selection criteria:

- ID = 10 or ±11
- EMFraction > 0.9
- Isolation < 0.15
- H-Matrix(7) < 12
- $p_T > 25$ GeV
- $|\eta_{detector}| < 1.1$
- No fiducial restrictions in ϕ.
- Matched with tag track within $\Delta R = \sqrt{\Delta\eta^2 + \Delta\phi^2} = \sqrt{0.1^2 + 0.1^2} = 0.14$.
- Must have fired the trigger.

Possible background contamination is reduced by requiring that tag- and probe-tracks have opposite signs, and by imposing a cut on the missing transverse energy of the event (missing $E_T < 15$ GeV). The following lists additional requirements:

- $|PVZ| < 60$ cm
- Tag-electron-probe-track invariant mass cut: 70 GeV $< M_{ee} <$ 110 GeV.

Once an event is found which satisfies all of the above requirements, a denominator histogram is filled. If a reconstructed EM cluster is found nearby the probe-track ($\Delta R = \sqrt{\Delta\eta^2 + \Delta\phi^2} = \sqrt{0.1^2 + 0.1^2} = 0.14$) which passes the EMID cuts (HMx, EMF, Iso), the respective numerator histogram is filled.

Figure 53 and Figure 54 show the EM efficiencies for data and MC in a one-dimensional parameterization versus probe track Φ and p_T. Note that the central calorimeter has narrow uninstrumented regions between the azimuthal module boundaries (*phi cracks*). An EM object entering the calorimeter near these boundaries can lose a portion of its energy in these cracks, which results in decreased EM efficiencies for these regions.

The average EM reco and ID efficiencies are derived by dividing the tag-electron-probe-track-matched-EM diem invariant mass histograms with the tag-electron-probe-track diem invariant mass histograms. The diem invariant mass distributions have background contamination. We estimate the background in the signal region by using the sidebands of the diem invariant mass distributions.

The average EM reco and ID efficiencies in data and MC are (with statistical uncertainties):

- $\varepsilon_{data}^{electron}(\text{EM}) = 88.9\% \pm 0.3\%$
- $\varepsilon_{MC}^{electron}(\text{EM}) = 93.1\% \pm 0.1\%$.

The sideband background subtraction cannot be applied in the case of parameterized efficiencies, since no diem invariant mass distributions are used. The level of background contamination is examined by deriving the average efficiency in data without the sideband background subtraction. The result is within 1% of the sideband subtracted value: 88.2% ± 0.2%.

EM event efficiencies are calculated in the following way:

- In a given event two-dimensional efficiency curves are used (versus p_T and Φ) to estimate the EM efficiencies ε_1 and ε_2 for the two EM objects (based on their p_T and Φ).

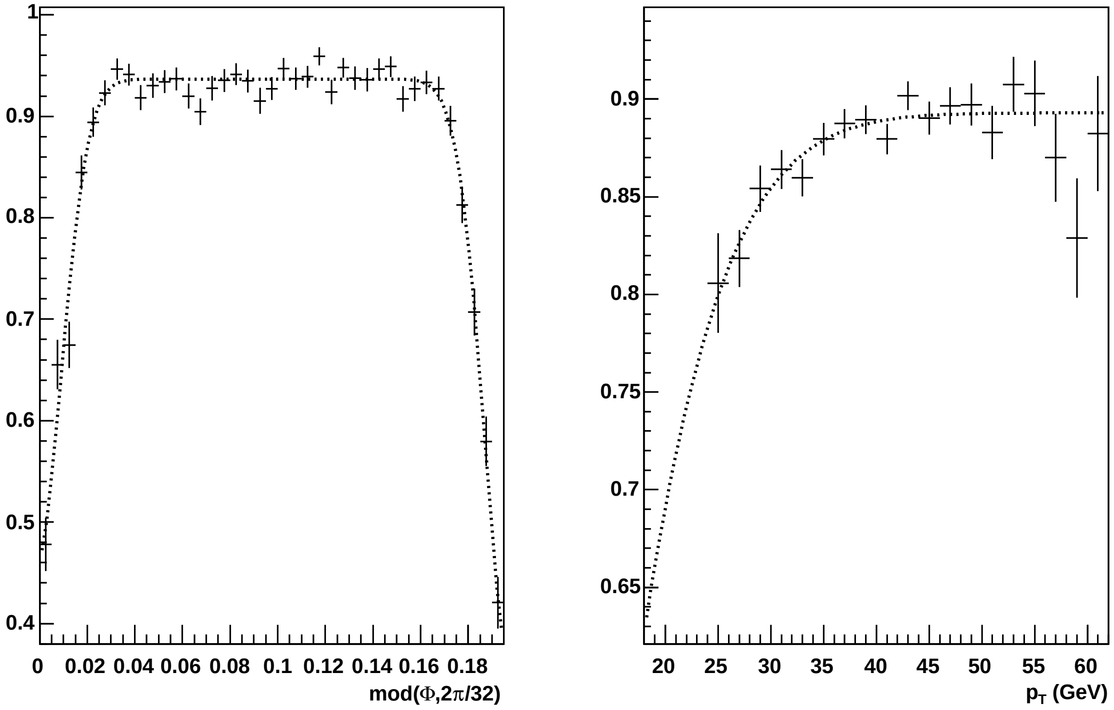

Figure 53. EM efficiencies versus probe track Φ and p_T in data. The Φ distribution shows the modulus(Φ, $\frac{2\pi}{32}$) distribution to illustrate the effect of the calorimeter Φ-module boundaries.

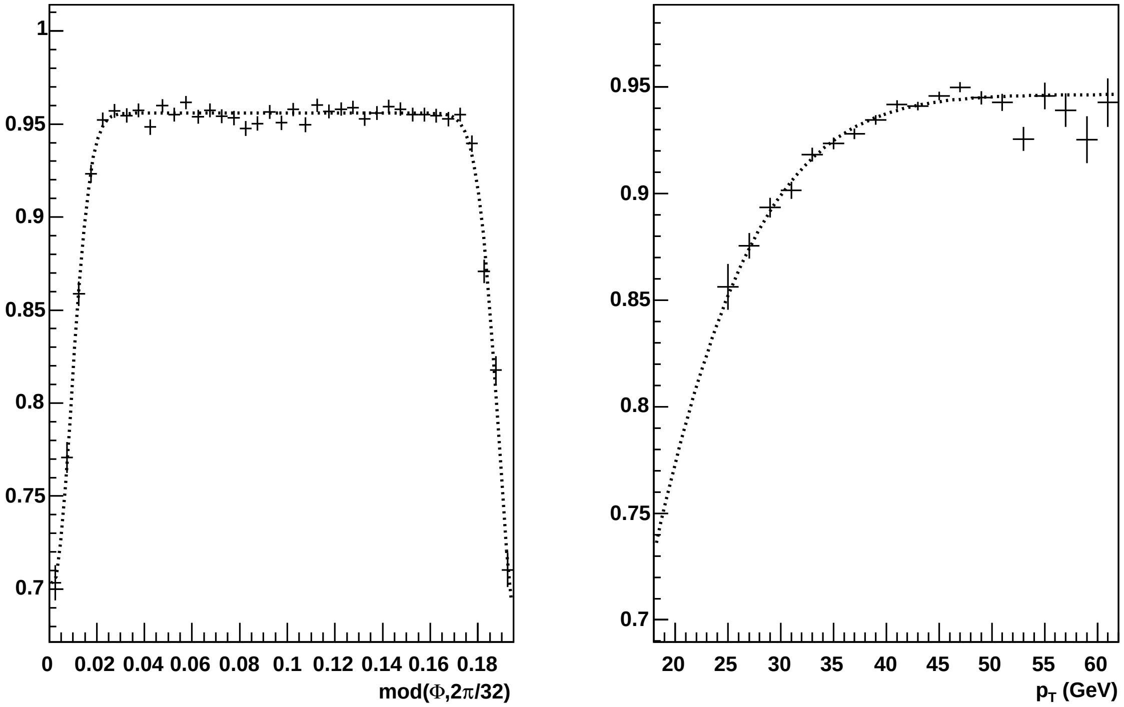

Figure 54. EM efficiencies versus probe track Φ and p_T in MC. The Φ distribution shows the modulus(Φ, $\frac{2\pi}{32}$) distribution to illustrate the effect of the calorimeter Φ-module boundaries.

- To calculate the event based EM efficiency, the product of ε_1 and ε_2 is taken:

$$\varepsilon_{EM} = \varepsilon_1 \cdot \varepsilon_2. \tag{8.4}$$

8.1.3 EM-Track Match Efficiency

Average track finding and matching efficiencies are derived using diem invariant mass distributions (Figure 55 to Figure 58).

Using a convolution of a Gaussian and Breit-Wigner fit for the Z peak and an exponential shape to describe the QCD and Drell-Yan contributions, the number of events under the Z peak is extracted from the four diem invariant mass distributions: $N_{1trk}(data)$, $N_{2trk}(data)$, $N_{1trk}(MC)$ and $N_{2trk}(MC)$. $N_{1trk}(data)$ and $N_{1trk}(MC)$ are the number of Z candidates with at least one track match in data and MC; $N_{2trk}(data)$ and $N_{2trk}(MC)$ are the number of Z candidates with exactly two track matches in data and MC. These numbers are used to estimate the average track finding and track matching efficiencies per electron in data and MC:

$$\varepsilon_{data}^{electron}(\text{Tracking}) = \frac{2 \cdot N_{2trk}(data)}{N_{2trk}(data) + N_{1trk}(data)} = 77.1\% \pm 0.3\% \tag{8.5}$$

$$\varepsilon_{MC}^{electron}(\text{Tracking}) = \frac{2 \cdot N_{2trk}(MC)}{N_{2trk}(MC) + N_{1trk}(MC)} = 87.8\% \pm 0.03\%. \tag{8.6}$$

The event based tracking efficiency is calculated in the following way:

- In each event the average electron tracking efficiency $\varepsilon_{tracking}^{electron}$ is used (Equation 8.5 and Equation 8.6).

- To calculate the event based tracking efficiency, all permutations for one or two track matched electrons are taken into account:

$$\varepsilon^{event}_{tracking} = 2 \cdot \varepsilon^{electron}_{tracking}(1 - \varepsilon^{electron}_{tracking}) + {\varepsilon^{electron}_{tracking}}^2 = 2 \cdot \varepsilon^{electron}_{tracking} - {\varepsilon^{electron}_{tracking}}^2 \qquad (8.7)$$

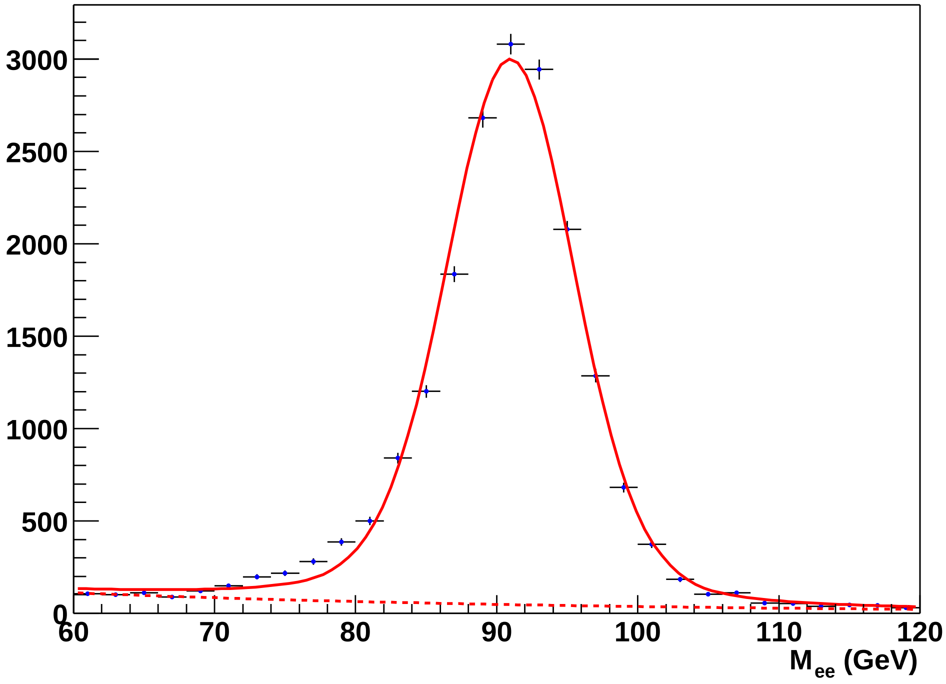

Figure 55. Invariant mass with at least one track-matched electron (data).

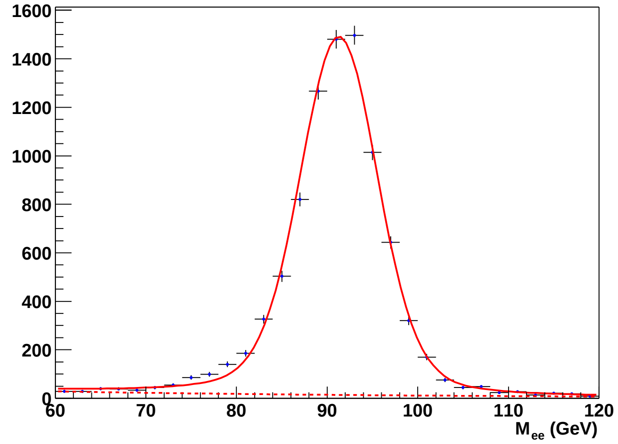

Figure 56. Invariant mass with two track-matched electrons (data).

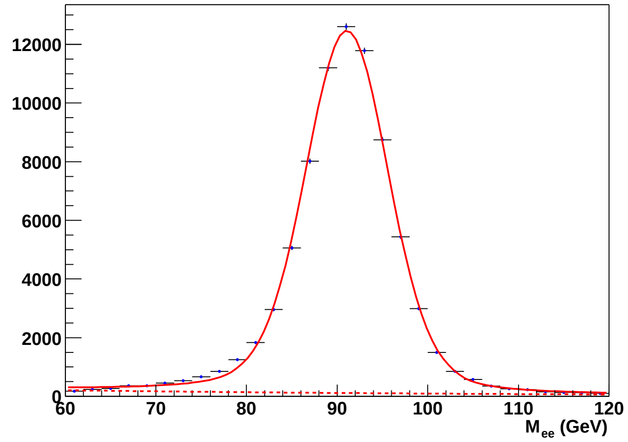

Figure 57. Invariant mass with at least one track-matched electron (MC).

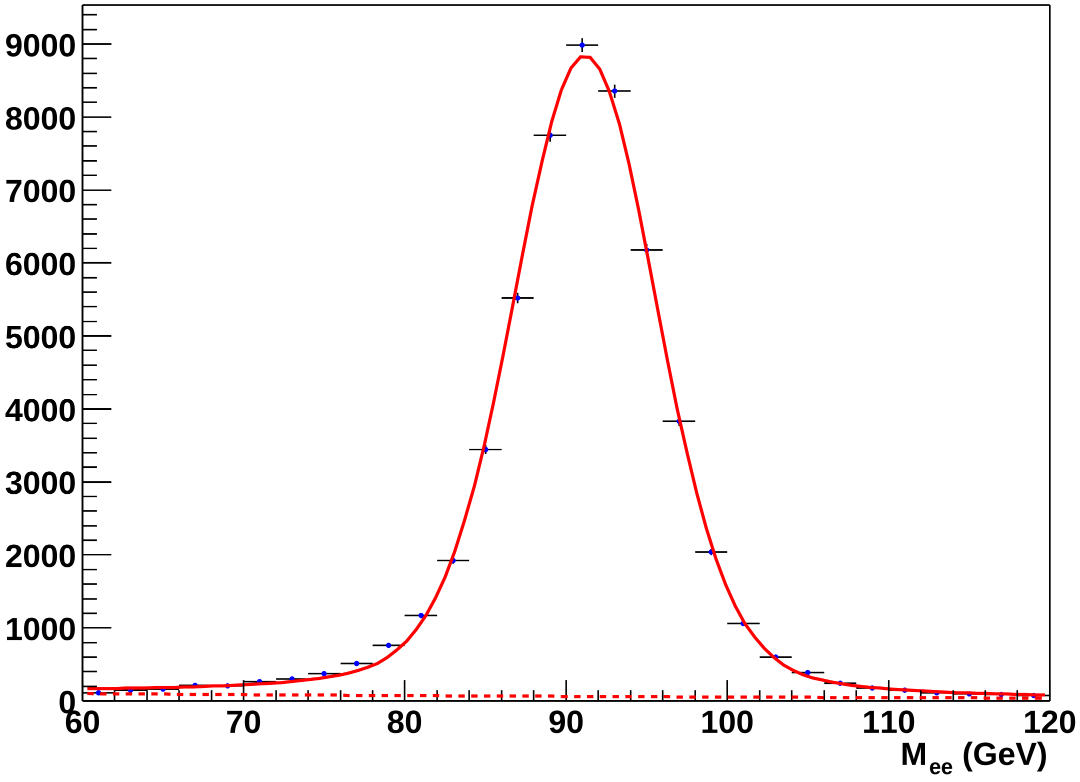

Figure 58. Invariant mass with two track-matched electrons (MC).

8.1.4 Acceptance

The $Z/\gamma^* \to e^+e^-$ PYTHIA MC sample with detector simulation is used to estimate the acceptance for the fiducial and kinematic cuts. The acceptance numerator counts the number of events satisfying the following requirements at the detector reconstructed level:

- Primary vertex cut: $|PVZ| < 60$ cm
- Electron cuts: $p_T > 25$ GeV and $|\eta| < 1.1$
- Diem invariant mass cut: 75 GeV $< M_{ee} <$ 105 GeV.

The acceptance denominator counts the number of events with generated Z/γ^* particles that are within the diem invariant mass window.

Since the acceptance calculation involves two reconstructed electrons, a corrective weight is applied to the reconstructed event. Based on the p_T and Φ values of the two electrons, the reconstruction efficiencies are estimated to be $\approx 98\%$. The product of the inverse of those reconstruction efficiencies yields a corrective weight. The Z p_T correction factor is also applied (see Chapter 7.4.2) as an additional weight in both the numerator and denominator of the acceptance.

The acceptance with statistical uncertainty for inclusive $Z/\gamma^* \to e^+e^-$ is estimated to be:

$$A(Z/\gamma^* \to e^+e^- + X) = 21.4\% \pm 0.1\%. \tag{8.8}$$

8.2 Cross Section Calculation

After applying all corrections, the number of corrected signal events is determined from the diem invariant mass distribution (Figure 59). A convolution of a Gaussian and Breit-Wigner shape is fitted to the Z peak. An exponential shape is used to describe the QCD and Drell-Yan contributions.

Since the Drell-Yan component is part of the signal, the QCD component needs to be disentangled from the Drell-Yan component. Using the inclusive $Z/\gamma^* \rightarrow e^+e^-$ PYTHIA MC sample, the percentage of Drell-Yan events in $Z/\gamma^* \rightarrow e^+e^-$ decays is estimated by fitting a Gaussian and Breit-Wigner shape to the Z component and an exponential shape to the Drell-Yan component. 2.06% of the events in the inclusive $Z/\gamma^* \rightarrow e^+e^-$ sample are due to Drell-Yan.

Based on these fits the number of signal events from direct Z boson and Drell-Yan decays is extracted, as well as the number of QCD background events in the diem invariant mass signal window (75 GeV $< M_{ee} <$ 105 GeV) [1]:

- Number of signal events from Z Boson and Drell-Yan decays = 18263.8
- Number of QCD background events = 407.5.

---

[1] The number of signal events is derived by counting all entries for a particular M_{ee} bin and subtracting from it the number of entries from the background fit.

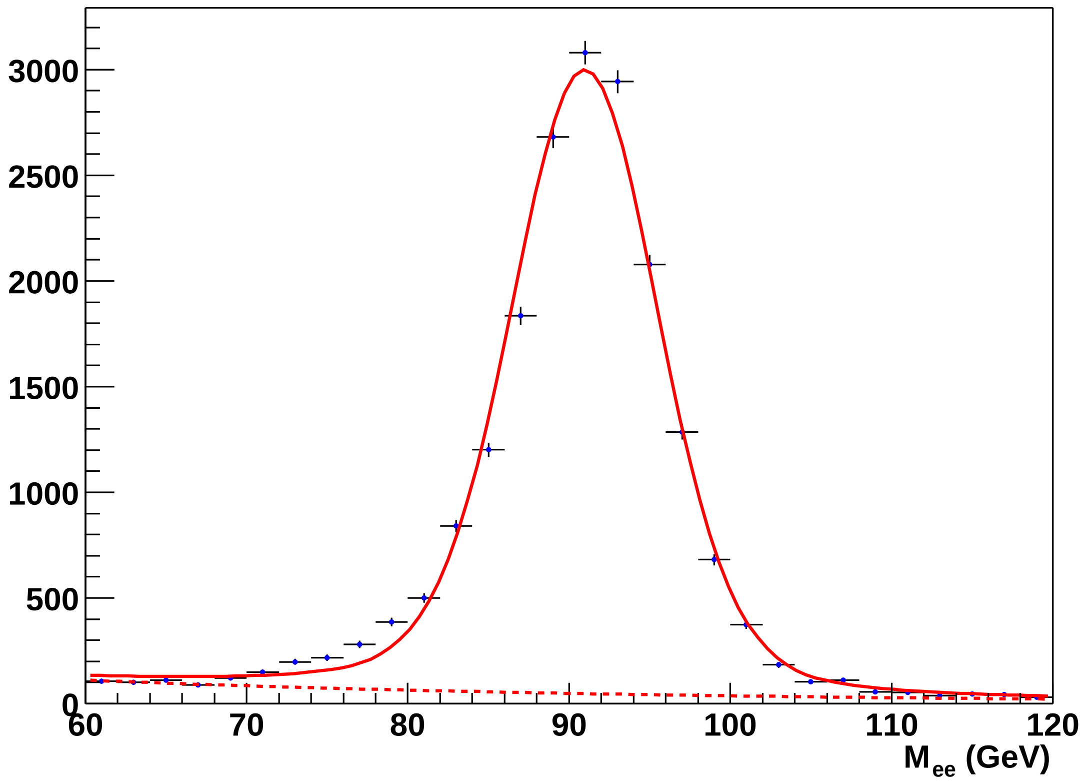

Figure 59. Diem invariant mass distribution for $Z/\gamma^* \rightarrow e^+e^- + X$ (Mean = 91.02 GeV ± 0.04 GeV, Width 4.03 GeV ± 0.04 GeV).

Based on the integrated luminosity (343 pb^{-1}) and the acceptance (21.4%), the inclusive Z/γ^* production cross section times branching fraction into electrons is calculated:

$$\sigma \times \text{BR}(Z/\gamma^* \to e^+e^-) = \frac{N - B}{\mathcal{L} \times A} = 248.9 \ \pm 2.5(\text{stat})\ \text{pb}. \tag{8.9}$$

In order to check the procedure that leads to the cross section measurement, a MC closure test was performed. The number of signal events, acceptance, and luminosity were evaluated in a PYTHIA MC sample. The calculated MC cross section (179 pb) was compared to the PYTHIA cross section that was used to generate the MC sample (183 pb). The calculated MC cross section was in good agreement with the MC input cross section.

8.3 Comparison to Other Measurements

Using the inclusive PYTHIA MC sample, a correction factor is derived to estimate the inclusive Z/γ^* cross section in a different diem invariant mass range (66 GeV $< M_{ee} <$ 116 GeV) [1]. The number of Z/γ^* candidates is counted at the particle level in the new diem invariant mass range. A ratio is taken which yields the correction to account for the change in the diem invariant mass range (66).

The result of 257.4 pb is compared with the CDF measurement (67) for the inclusive Z/γ^* cross section (66 GeV $< M_{ee} <$ 116 GeV) of 255.8 ± 3.9(stat) pb. Both results are in good agreement.

---

[1] The MC sample used a generator cut of $|\eta_Z| < 4.2$. Although no restriction in η_Z would have been preferable, the impact on the final results is believed to be negligible.

CHAPTER 9

MEASUREMENT OF THE $\mathbf{Z/\gamma^*(\rightarrow e^+e^-)+\geq n}$ JET CROSS SECTIONS

This section outlines the procedure to measure the $Z/\gamma^*(\rightarrow e^+e^-)$ production cross section for different inclusive jet multiplicities. For each jet multiplicity the number of signal events is determined from the diem invariant mass histograms in the range of 75-105 GeV. All efficiencies are examined for jet multiplicity dependence and applied to the diem invariant mass distributions as corrections. The cross sections as a function of jet multiplicity are also corrected for jet reconstruction and identification efficiencies, and for event migration due to the finite jet energy resolution of the detector (*unsmearing*).

The following sections outline the determination of all efficiencies and acceptances, as well as the unsmearing procedure and the cross section evaluation.

9.1 Efficiencies vs Jet Multiplicity

In the following sections the PYTHIA MC sample is used to derive corrections for the inclusive sample, while ALPGEN MC samples are used for the n-jet corrections.

9.1.1 Trigger Efficiency

The electron trigger efficiency as a function of jet multiplicity is measured (Figure 60). No significant variation in the trigger efficiencies is observed as jet activity increases[1]. Therefore,

---

[1] Any possible decrease of the object based trigger efficiency versus jet multiplicity for the v12 dataset would yield a negligible contribution to the overall event based trigger efficiency.

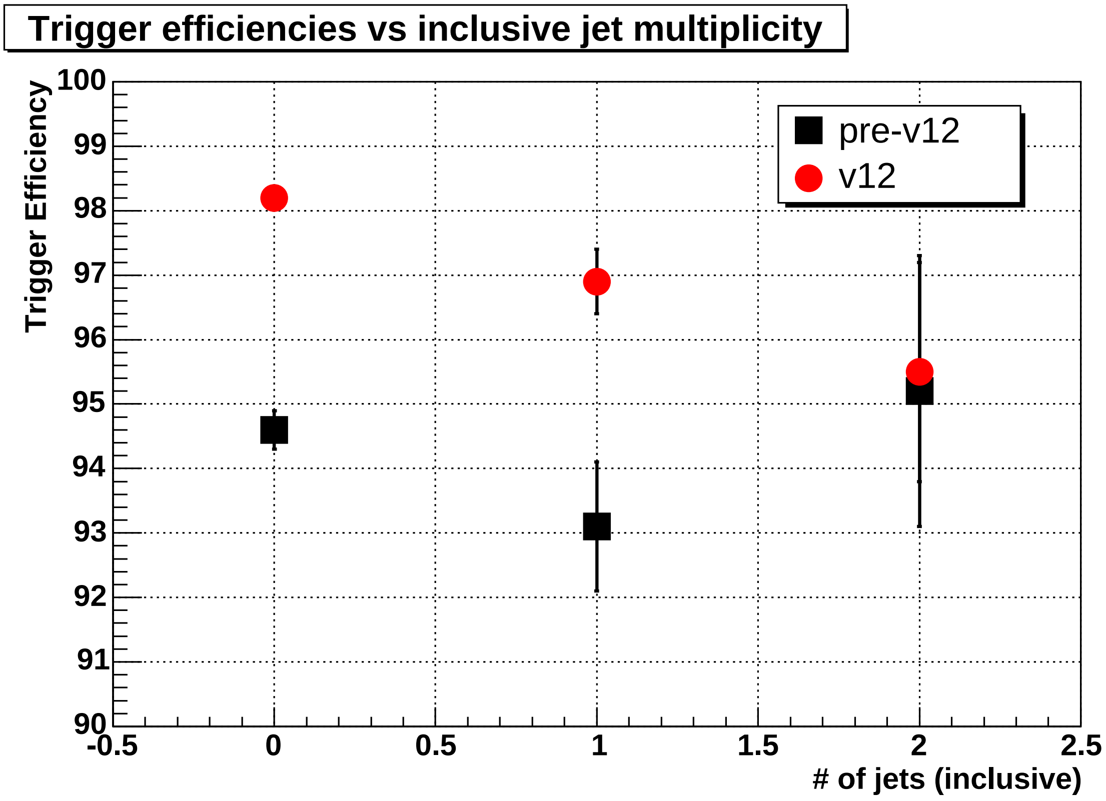

Figure 60. Average object based trigger efficiencies in data versus inclusive jet multiplicity.

the same trigger corrections as for the inclusive sample are applied to all jet multiplicity bins (see Chapter 8.1.1). Table VI summarizes electron trigger efficiencies for the pre-v12 and v12 datasets for different inclusive jet multiplicities. A systematic uncertainty of ±5% for the object based trigger efficiencies is assigned for all jet multiplicities.

Jet multiplicity	pre-v12	v12
≥ 0	94.6% ± 0.3%	98.2% ± 0.1%
≥ 1	93.1% ± 1.0%	96.9% ± 0.5%
≥ 2	95.2% ± 2.1%	95.5% ± 1.7%

TABLE VI

OBJECT BASED TRIGGER EFFICIENCIES WITH STATISTICAL UNCERTAINTIES FOR THE PRE-V12 AND V12 DATASETS FOR DIFFERENT INCLUSIVE JET MULTIPLICITIES.

9.1.2 EM Reconstruction and Identification Efficiency

Averaged single-EM efficiencies are derived using the procedure outlined in Chapter 8.1.2 in data and MC for different jet multiplicities (Figure 61). The same EM corrections as for the inclusive sample are applied to each jet multiplicity sample. Residual inefficiencies due to additional jet activity are examined (Figure 61). Table VII summarizes the EM reco and ID efficiencies in data and MC for different jet multiplicities.

No significant change of the average object based efficiencies with respect to jet multiplicity is observed in data. Therefore, no residual correction is applied. From the fluctuations of the single-EM reconstruction and ID efficiencies, a systematic uncertainty of ±3% is assigned for all jet multiplicities.

Based on the efficiency drop in MC a corrective weight is applied to each jet multiplicity. The value for the weight is derived by taking the ratio of the EM efficiency for the inclusive sample and the average of the EM efficiencies for the 1-jet, 2-jet and 3-jet samples.

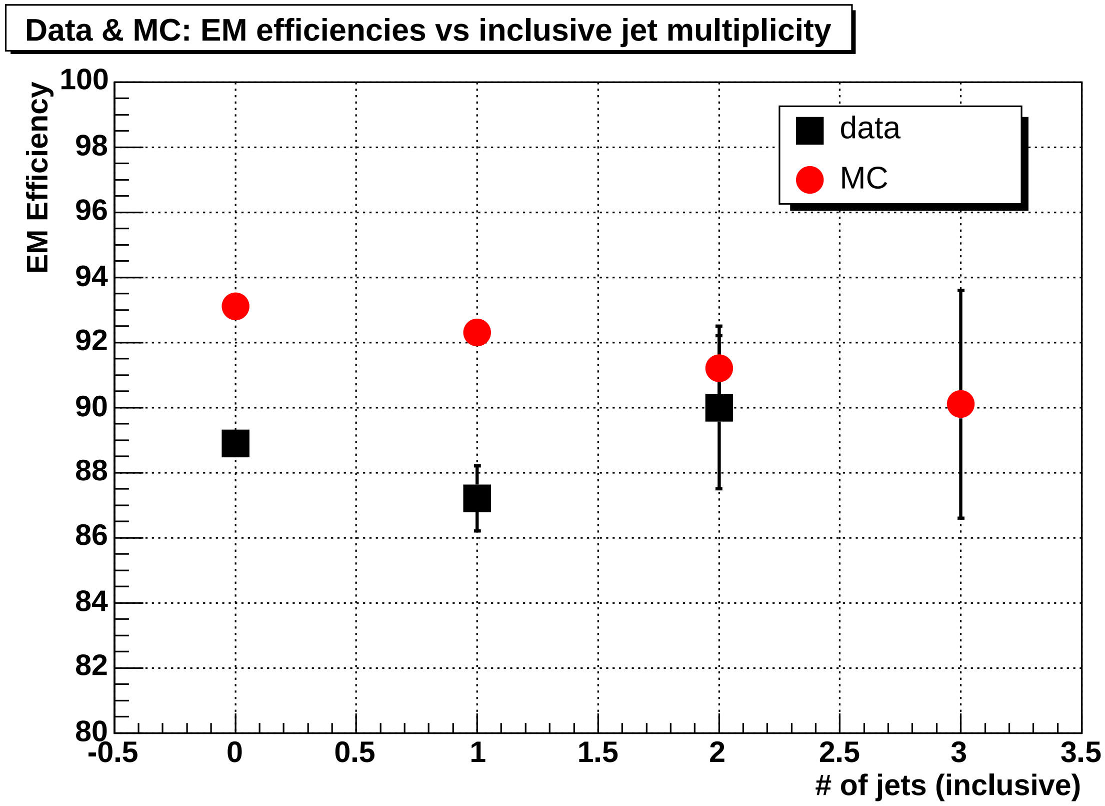

Figure 61. Average object based EM reco and ID efficiencies in data and MC versus inclusive jet multiplicity. There was not enough statistics available to estimate the EM efficiency in data for ≥ 3 jets.

Jet multiplicity	data	MC
≥ 0	88.9% ± 0.3%	93.1% ± 0.1%
≥ 1	87.2% ± 1.0%	92.3% ± 0.3%
≥ 2	90.0% ± 2.5%	91.2% ± 1.0%
≥ 3	(n/a)	90.1% ± 3.5%

TABLE VII

OBJECT BASED EM RECO AND ID EFFICIENCIES WITH STATISTICAL UNCERTAINTIES IN DATA AND MC FOR DIFFERENT INCLUSIVE JET MULTIPLICITIES. THERE WAS NOT ENOUGH STATISTICS AVAILABLE TO ESTIMATE THE EM EFFICIENCY IN DATA FOR ≥ 3 JETS.

9.1.3 EM-Track Match Efficiency

Figure 62 and Table VIII show the average object based tracking efficiencies for different jet multiplicities. In MC, no efficiency variations are observed. Therefore, the value from the inclusive sample is used to correct for tracking inefficiencies for all jet multiplicities. In data, the inclusive value is used for the inclusive sample, the 1-jet value is used for the 1-jet multiplicity and the 2-jet value is used for all multiplicities of 2 and above.

Table IX lists the systematic uncertainties for the data efficiencies. For the 1-jet and 2-jet samples, the respective statistical uncertainties are used as systematics. For the 3-, 4-, and 5-jet samples, the systematic uncertainty is estimated from the statistical uncertainty of the 2-jet bin added in quadrature with the difference between the 2-jet efficiency value, and a linear fit to the 0-, 1-, and 2-jet bins extrapolated to the 3-, 4-, and 5-jet bins.

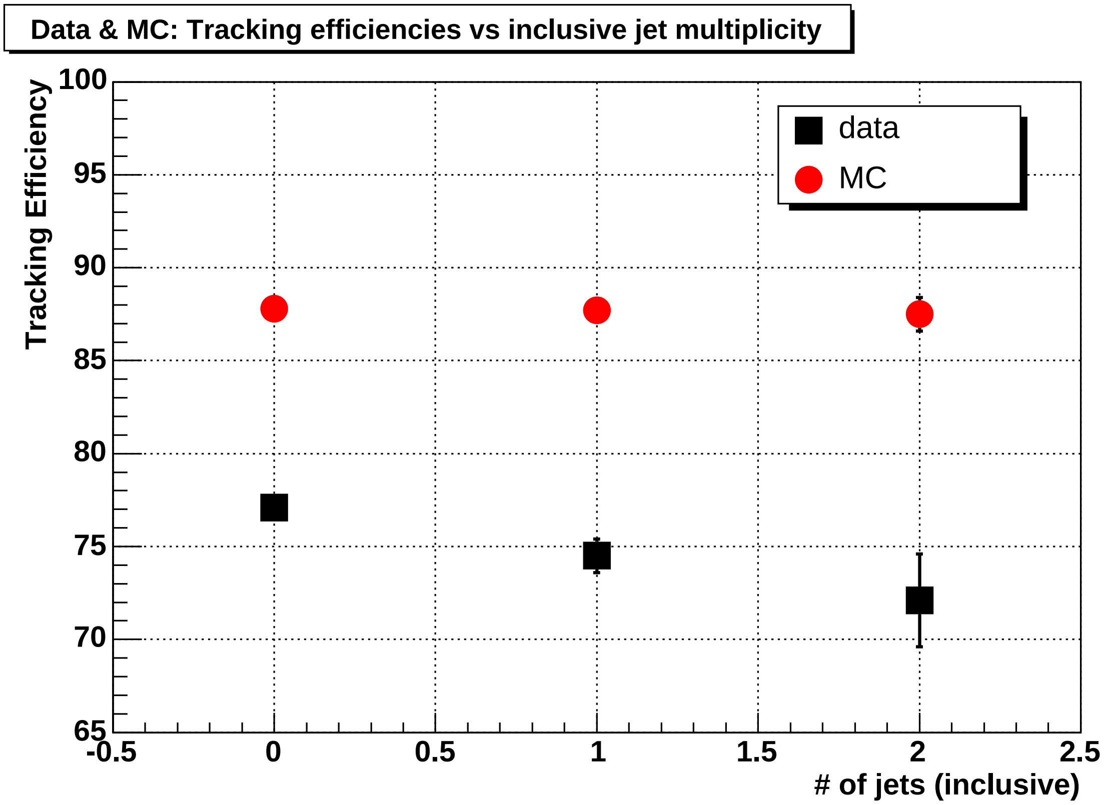

Figure 62. Average object based tracking efficiencies in data and MC versus inclusive jet multiplicity.

Jet multiplicity	data	MC
≥ 0	77.1% ± 0.3%	87.8% ± 0.03%
≥ 1	74.5% ± 0.9%	87.7% ± 0.3%
≥ 2	72.1% ± 2.5%	87.5% ± 0.9%

TABLE VIII

OBJECT BASED TRACKING EFFICIENCIES WITH STATISTICAL UNCERTAINTIES IN DATA AND MC FOR DIFFERENT INCLUSIVE JET MULTIPLICITIES.

Jet multiplicity	Data Efficiency	Systematic Uncertainty
≥ 0	77.1%	± 0.3%
≥ 1	74.5%	± 0.9%
≥ 2	72.1%	± 2.5%
≥ 3	72.1%	± 3.5%
≥ 4	72.1%	± 5.6%
≥ 5	72.1%	± 7.9%

TABLE IX

OBJECT BASED TRACKING EFFICIENCIES WITH SYSTEMATIC UNCERTAINTIES.

9.1.4 Acceptance

ALPGEN MC samples are used to estimate the kinematic and geometric acceptances for different jet multiplicities[1]. The numerator for the n-jet acceptance contains the number of events satisfying the following requirements:

- Primary vertex cut: $|PVZ| < 60$ cm
- Electron cuts: $p_T > 25$ GeV and $|\eta| < 1.1$
- Diem invariant mass cut: 75 GeV $< M_{ee} <$ 105 GeV
- Particle level jet cut: n jets with $p_T > 20$ GeV and $|\eta| < 2.5$.

The denominator for the n-jet acceptance contains the number of events satisfying the following requirements:

---

[1] The Z+3 jet sample is used for jet multiplicities of 3, 4, and 5.

Jet multiplicity	Acceptance
≥ 0	21.4% ± 0.1%
≥ 1	25.1% ± 0.2%
≥ 2	25.4% ± 0.2%
≥ 3	27.4% ± 0.3%
≥ 4	28.5% ± 0.7%
≥ 5	30.3% ± 1.9%

TABLE X

ACCEPTANCES WITH STATISTICAL UNCERTAINTIES FOR DIFFERENT JET MULTIPLICITIES.

- MC generator diem invariant mass cut: 75 GeV $< M_{ee} <$ 105 GeV
- Particle level jet cut: n jets with $p_T >$ 20 GeV and $|\eta| < 2.5$.

No additional Z p_T correction is needed since the Z p_T distributions between data and ALPGEN MC agree reasonably well (see Chapter 7.4.2). Table X summarizes the acceptances for different jet multiplicities. On average, higher jet multiplicities lead to higher Z p_T, since the Z boson recoils against the jet(s) in the event. This in turn leads to electrons coming from Z decays that are more likely to pass the acceptance requirements. Therefore, as jet multiplicities increase, acceptances increase as well.

9.1.5 Jet Reconstruction and Identification Efficiency

The jet reco/ID efficiency was estimated using a tuned MC sample according to the following procedure (68):

- A scaling factor is derived based on the "Z p_T balance" method. This method selects events with Z candidates and probes for a recoiling jet opposite in Φ. The "efficiency" of finding a recoiling jet can be measured as a function of the Z p_T in data and MC.
- The ratio of the Z p_T "efficiency" in data and MC yields a scaling factor.
- The scaling factor is applied to the MC sample to tune it to match the data distributions.
- The tuned MC is used to measure the "straight" jet reco/ID efficiency by matching particle level jets with calorimeter jets within a search cone of $\Delta \mathrm{R} = 0.4$.
- The efficiency is parameterized versus particle jet p_T. The p_T values of the particle jets are smeared with the data energy resolutions (see Chapter 7.2.1).

Figure 63 shows the data jet reconstruction efficiencies for different regions in the calorimeter.

9.2 Cross Section Calculation

9.2.1 Unsmearing

In order to determine particle level cross sections, we correct the measured data jet multiplicities for event migration due to the finite jet energy resolution of the detector. Correction factors are determined using a Z + jets PYTHIA MC sample, which was generated using $f_i \bar{f}_i \rightarrow g Z^0$ and $f_i g \rightarrow f_i Z^0$ subprocesses. The sample only contained particle level jets, i.e. no detector simulation. The p_T values of the particle level jets were smeared with the data jet energy resolution. Subsequently, jets were removed from the sample, probabilistically, and according to the measured jet reconstruction efficiencies. Figure 64 - Figure 71 compares jet

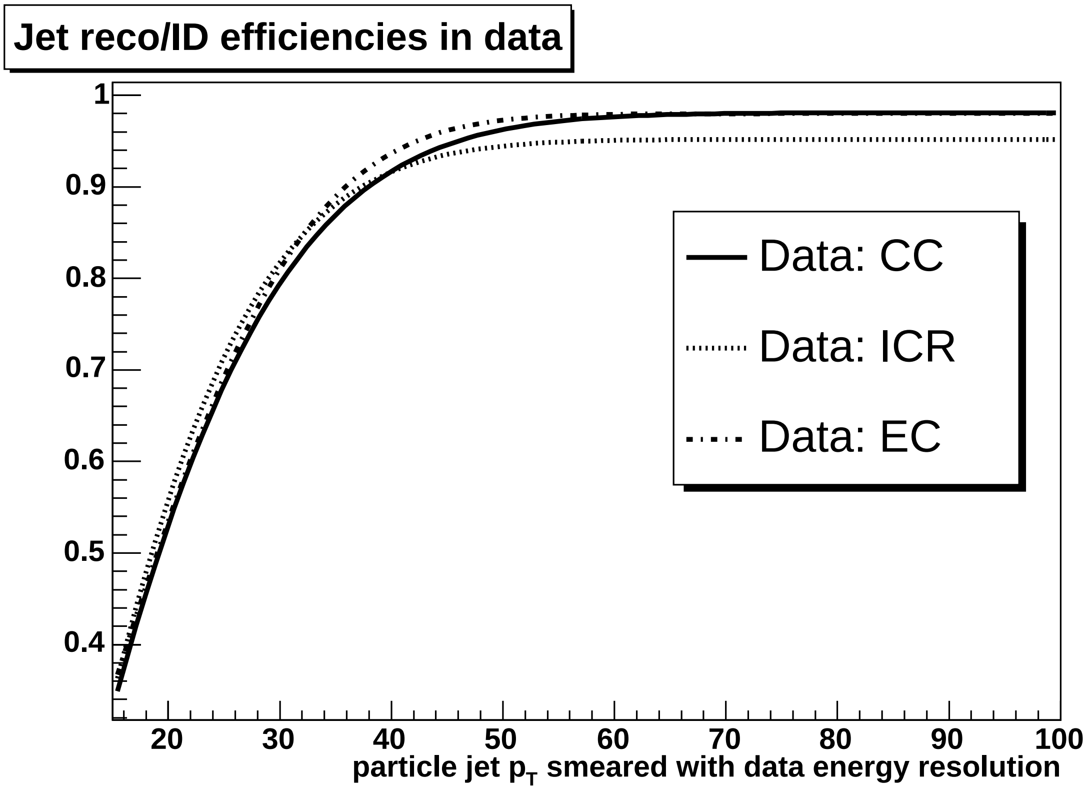

Figure 63. Jet reco/ID efficiencies in data. CC $= -0.7 < |\eta_{det}| < 0.7$, ICR $= 0.7 < |\eta_{det}| < 1.5$, EC $= 1.5 < |\eta_{det}| < 2.5$.

p_T and η distributions between the data and MC sample with reasonable agreement.

The inclusive jet multiplicity for this PYTHIA sample is compared to data in Figure 72. There is increasing disagreement at higher jet multiplicities, since PYTHIA does not include higher order contributions at the hard scatter level. This discrepancy is corrected by taking the ratio between data and MC for each inclusive jet multiplicity (Figure 73) and then applying these weights to the PYTHIA events. After this additional step, the inclusive jet multiplicity spectrum in PYTHIA is again compared with data with much better agreement (Figure 74)[1]. This corrected MC sample is used to derive the coefficients that unsmear the measured data jet multiplicities, also taking into account jet reco/ID inefficiencies.

To calculate the coefficients, the inclusive jet multiplicity histogram for particle level jets with $p_T > 20$ GeV and $|\eta_{physics}| < 2.5$ is divided by the inclusive jet multiplicity histogram for particle level jets with smeared $p_T > 20$ GeV and $|\eta_{physics}| < 2.5$ (after applying jet reco/ID efficiencies). The exact values of these ratios yield the unsmearing and jet reco/ID coefficients which are applied as multiplicative factors to the measured jet multiplicities in data. Figure 75 shows the numerator and denominator jet multiplicity histograms, as well as the ratio when applying jet smearing and jet reco/ID efficiencies in the denominator. For comparison Figure 76 shows the same distributions without applying jet reco/ID efficiencies, i.e. applying only jet smearing.

The statistical uncertainty of each unsmearing and jet reco/ID coefficient is used as a sta-

---

[1] Since a probabilistic method is used in this procedure, the final comparison is not expected to show perfect agreement.

Jet multiplicity	Unsmearing and jet reco/ID coefficient
≥ 1	$1.10\ ^{+0.08}_{-0.06}$
≥ 2	$1.26\ ^{+0.18}_{-0.16}$
≥ 3	$1.50\ ^{+0.25}_{-0.24}$
≥ 4	$1.90\ ^{+0.52}_{-0.39}$
≥ 5	$4.00\ ^{+3.42}_{-1.13}$

TABLE XI

UNSMEARING AND JET RECO/ID COEFFICIENTS WITH SYSTEMATIC UNCERTAINTY DUE TO RESOLUTION AND JET RECO/ID EFFICIENCY.

tistical uncertainty for the final cross sections (see Chapter 10.7). Table XI summarizes all coefficients.

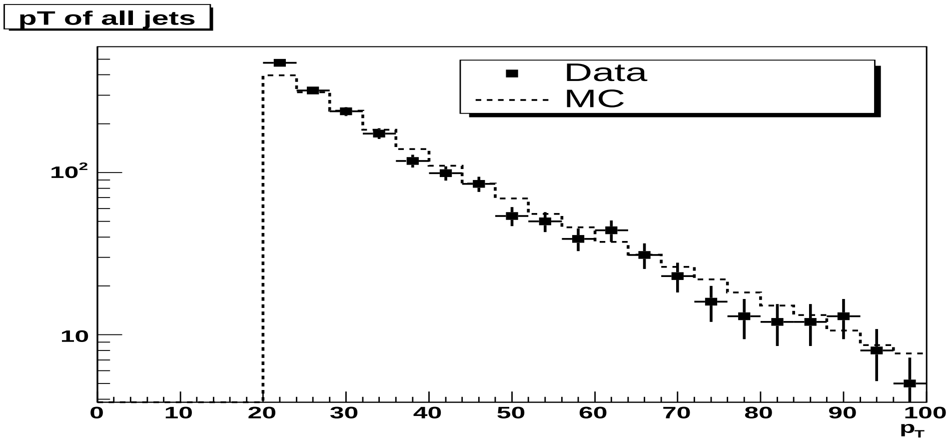

Figure 64. Comparison of jet p_T for all jets between data and particle level MC on a logarithmic scale (with data resolution smearing and jet reco/ID efficiencies applied). The MC distribution is normalized to the number of events in data.

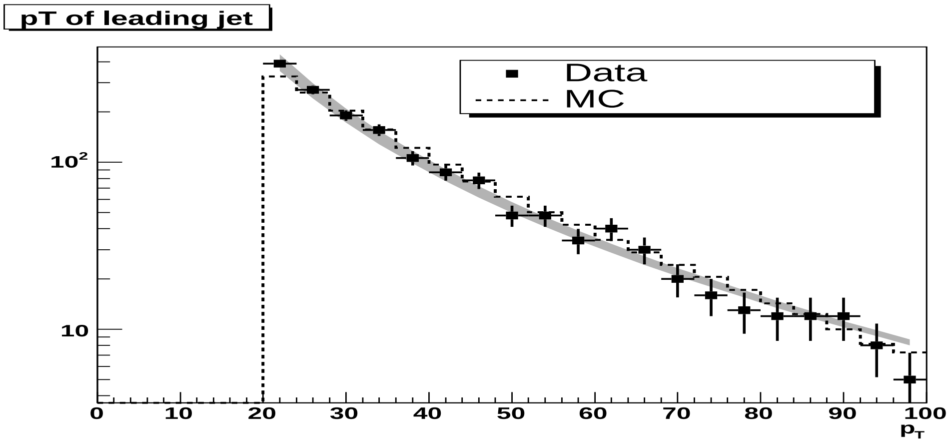

Figure 65. Comparison of jet p_T for leading jets between data and particle level MC on a logarithmic scale (with data resolution smearing and jet reco/ID efficiencies applied). The gray band shows the uncertainty due to the jet energy scale. The MC distribution is normalized to the number of events in data.

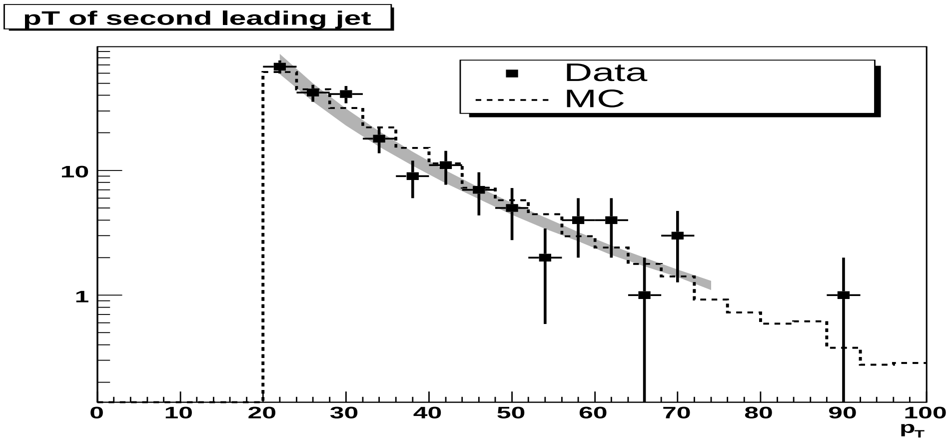

Figure 66. Comparison of jet p_T for second leading jets between data and particle level MC on a logarithmic scale (with data resolution smearing and jet reco/ID efficiencies applied). The gray band shows the uncertainty due to the jet energy scale. The MC distribution is normalized to the number of events in data.

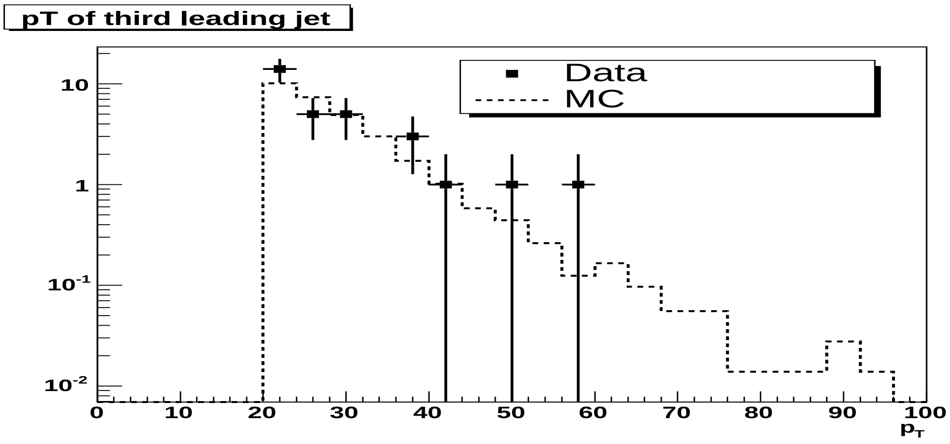

Figure 67. Comparison of jet p_T for third leading jets between data and particle level MC on a logarithmic scale (with data resolution smearing and jet reco/ID efficiencies applied). The MC distribution is normalized to the number of events in data.

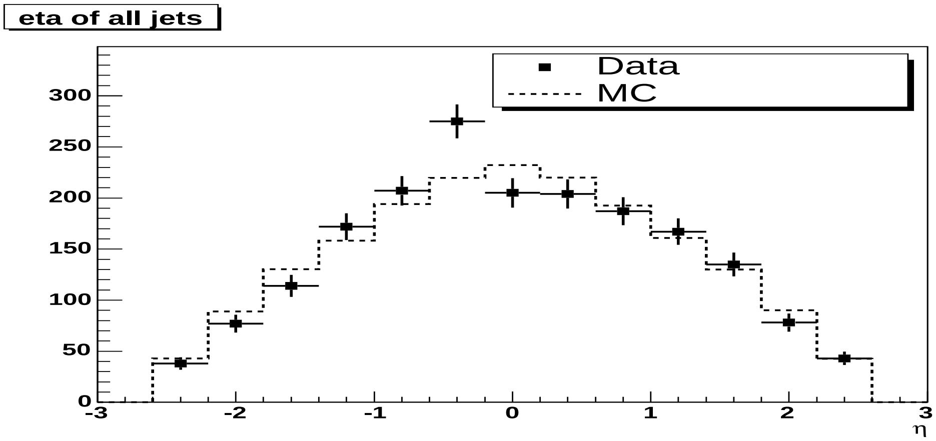

Figure 68. Comparison of jet η for all jets between data and particle level MC (with data resolution smearing and jet reco/ID efficiencies applied). The MC distribution is normalized to the number of events in data.

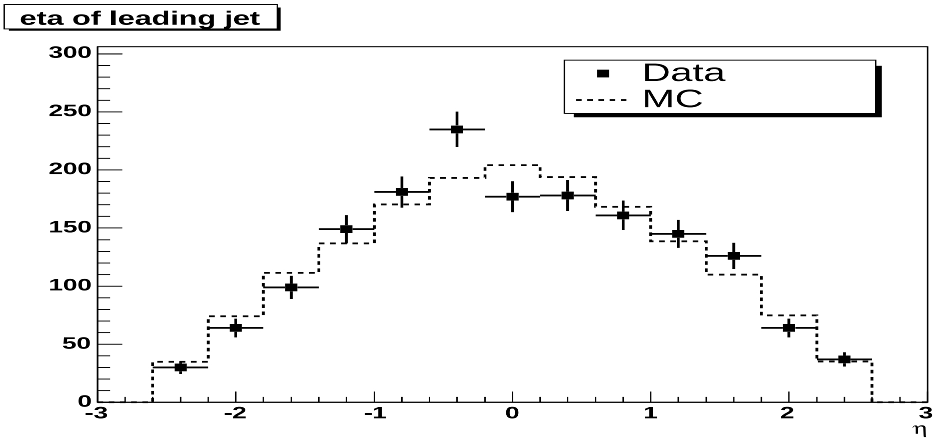

Figure 69. Comparison of jet η for leading jets between data and particle level MC (with data resolution smearing and jet reco/ID efficiencies applied). The MC distribution is normalized to the number of events in data.

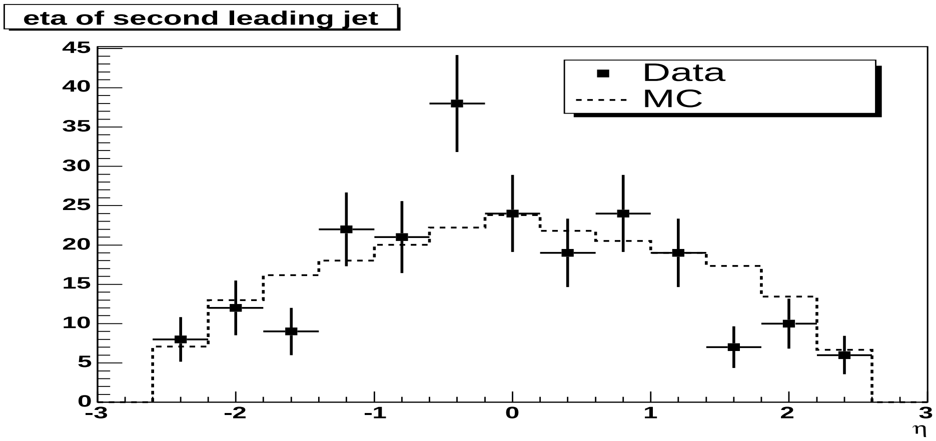

Figure 70. Comparison of jet η for second leading jets between data and particle level MC (with data resolution smearing and jet reco/ID efficiencies applied). The MC distribution is normalized to the number of events in data.

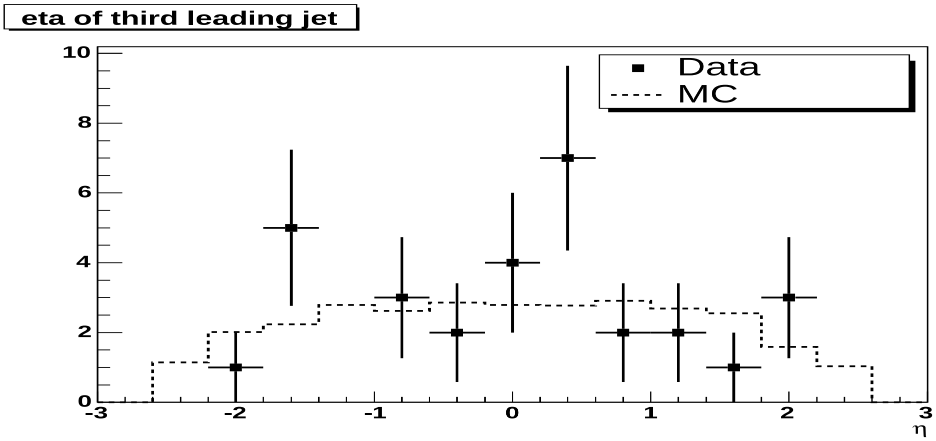

Figure 71. Comparison of jet η for third leading jets between data and particle level MC (with data resolution smearing and jet reco/ID efficiencies applied). The MC distribution is normalized to the number of events in data.

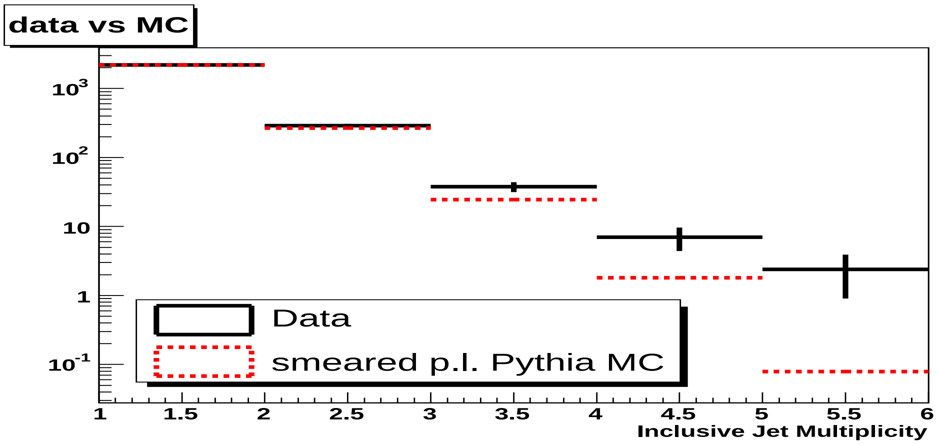

Figure 72. Comparison of inclusive jet multiplicities between data and particle level MC (applying data resolution smearing and data jet reco/ID efficiencies). The distributions are normalized with respect to the first bin. Only statistical uncertainties for data are shown.

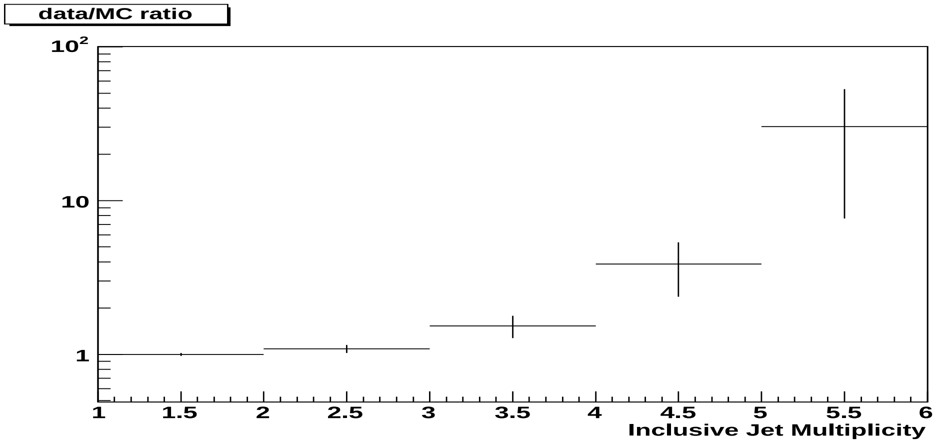

Figure 73. Ratio of MC (with smearing and jet reco/ID efficiencies) inclusive jet multiplicities and data inclusive jet multiplicities.

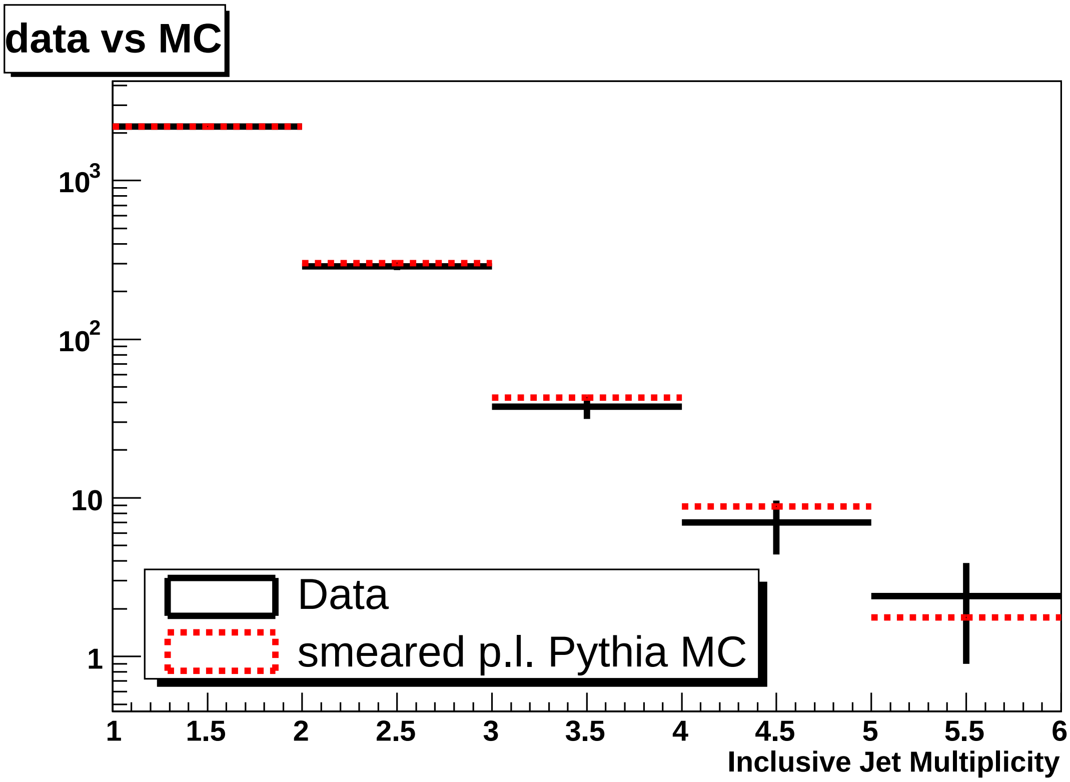

Figure 74. Comparison of inclusive jet multiplicities between data and particle level MC (after applying correction factors). The distributions are normalized with respect to the first bin. Only statistical uncertainties for data are shown.

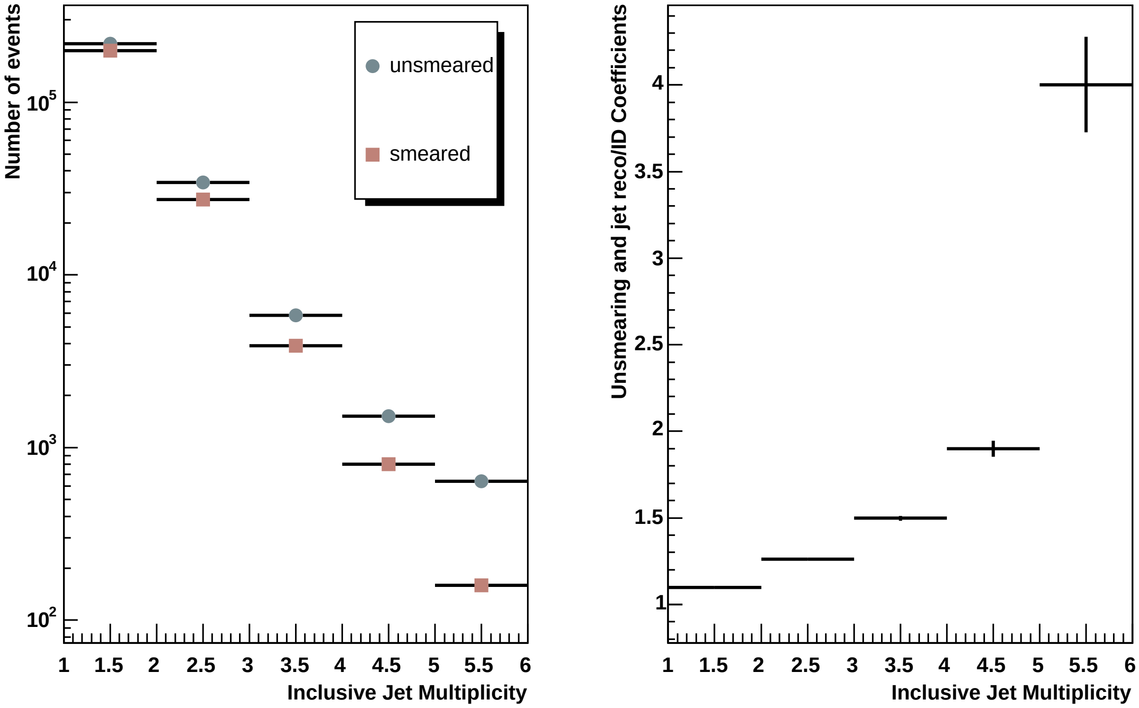

Figure 75. Unsmearing and jet reco/ID particle jet multiplicities (left) and coefficients (right).

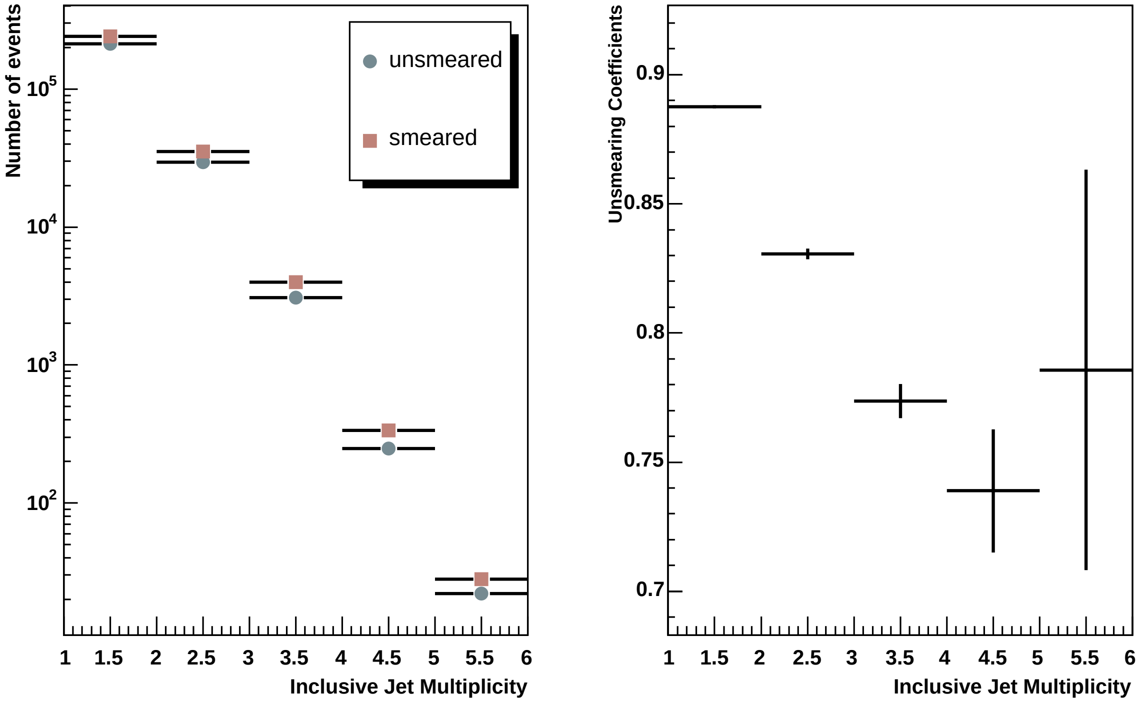

Figure 76. Unsmearing jet multiplicities (left) and coefficients (right) without applying jet reco/ID efficiencies.

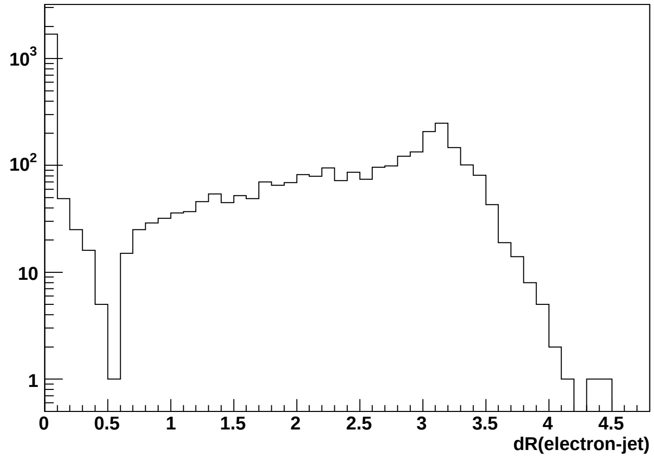

Figure 77. ΔR between probe tracks and good jets in data (without electron-jet-overlap cut).

9.2.2 Electron-Jet-Overlap Correction

The electron-jet-overlap correction provides an adjustment for the fraction of jets that are rejected due to an overlap with electrons from Z/γ^* decays.

Using the tag-and-probe method outlined in Chapter 8.1.2, the ΔR distribution between probe tracks and reconstructed jets that pass all jet quality cuts except for the electron-jet-overlap cut is plotted in data and MC (Figure 77 and Figure 78).

There is an excess of entries at ΔR values of 0 and π due to fake jets (i.e. originated from the electron energy deposits) which survived the jet quality cuts. Therefore, all jets are rejected that are near either of the two electrons from Z/γ^* decays within ΔR=0.4. Figure 79 shows the same distribution as in Figure 77 after adding the electron-jet-overlap cut in data.

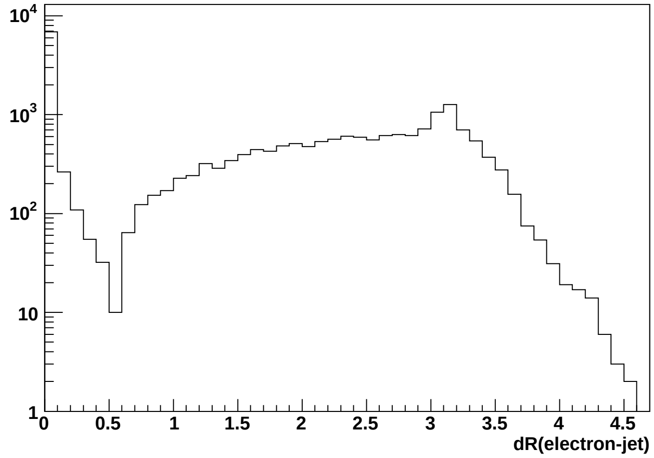

Figure 78. ΔR between probe tracks and good jets using PYTHIA MC (without electron-jet-overlap cut).

For comparison Figure 80 shows the ΔR between generated Z/γ^* electrons and partons in MC.

A correction is derived in order to account for the real jets that are removed by the electron-jet-overlap cut. Using the same PYTHIA MC sample as for the unsmearing studies (see Chapter 9.2.1), the correction factors due to the electron-jet-overlap are estimated by taking the ratio of the inclusive parton multiplicity distribution for all partons with $p_T > 20$ GeV and $|\eta| <2.5$ and the inclusive parton multiplicity distribution for partons that are outside of the ΔR cone with respect to the electrons from the Z/γ^*.

Correction factors are derived per multiplicity bin using ΔR cones of size 0.4 and 0.7 and then taking the middle value as the final correction factors and the half difference as the

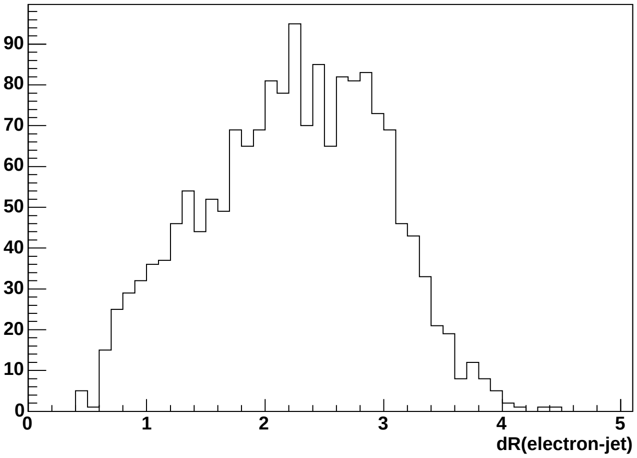

Figure 79. ΔR between probe tracks and good jets in data (after the electron-jet-overlap cut was applied).

systematic uncertainty. This is done in order to account for the position resolution between partons and calorimeter jets (see Figure 81).

Table XII summarizes the electron-jet-overlap correction factors for different jet multiplicity samples. These corrections are applied as multiplicative factors to the cross sections as a function of jet multiplicity in data.

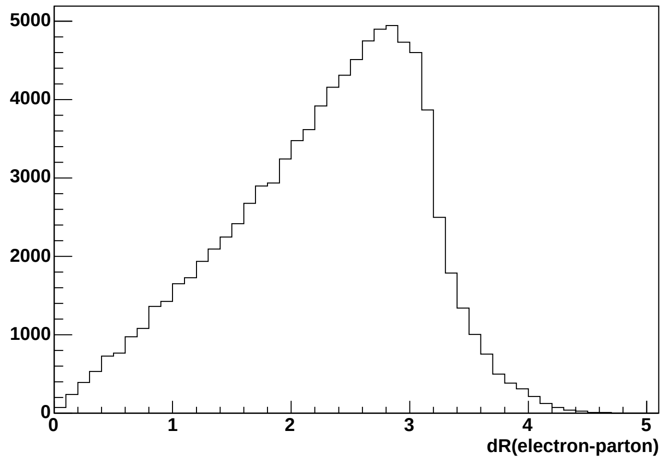

Figure 80. ΔR between generated electrons ($p_T > 25$ GeV, $|\eta| < 1.1$) and partons ($p_T > 20$ GeV, $|\eta| < 2.5$) in MC.

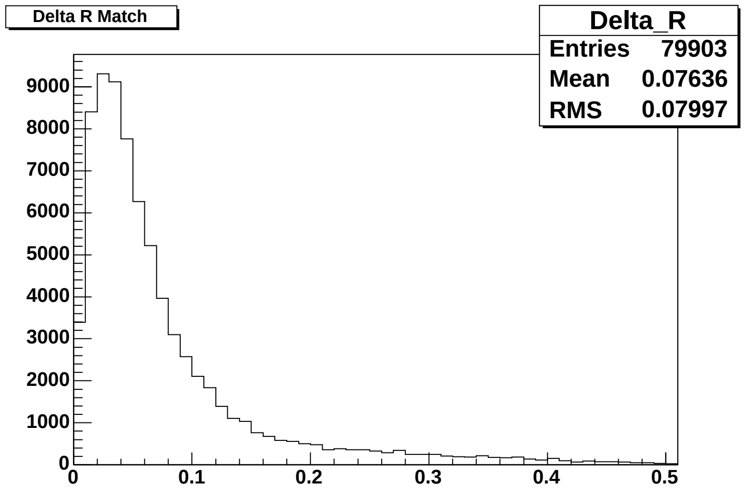

Figure 81. ΔR between partons and matched calorimeter jets ($p_T > 20$ GeV, $|\eta| < 2.5$) in MC.

Jet Multiplicity	Electron-Jet-Overlap Coefficient
≥ 1	1.059 ±0.028
≥ 2	1.075 ±0.041
≥ 3	1.092 ±0.054
≥ 4	1.109 ±0.067
≥ 5	1.125 ±0.077

TABLE XII

ELECTRON-JET-OVERLAP COEFFICIENTS WITH SYSTEMATIC UNCERTAINTIES.

9.2.3 Cross Sections

Figure 82 - Figure 86 shows the diem invariant mass distributions for jet multiplicities $\geq$1 to $\geq$5 which are used to extract the number of signal and background events for the cross section calculation (corrected for trigger, EM and tracking inefficiencies). For jet multiplicities of $\geq$1 and $\geq$2, the same technique to extract the number of signal and background events is used as outlined in Chapter 8.2. For jet multiplicities of $\geq$3, sidebands are used to estimate the background. The background contributions for higher jet multiplicity samples were estimated by extrapolating an exponential fit to the QCD background of the 0 - 3 jet multiplicity bins (see Chapter 10.7).

Table XIII summarizes the number of signal and background events for each jet multiplicity. A 2.06% Drell-Yan contribution to the number of signal events is derived using the inclusive MC PYTHIA sample. The fully corrected and unsmeared cross sections versus jet multiplicities (with jet $p_T > 20$ GeV, $|\eta| < 2.5$) are shown in Figure 87 with statistical uncertainties.

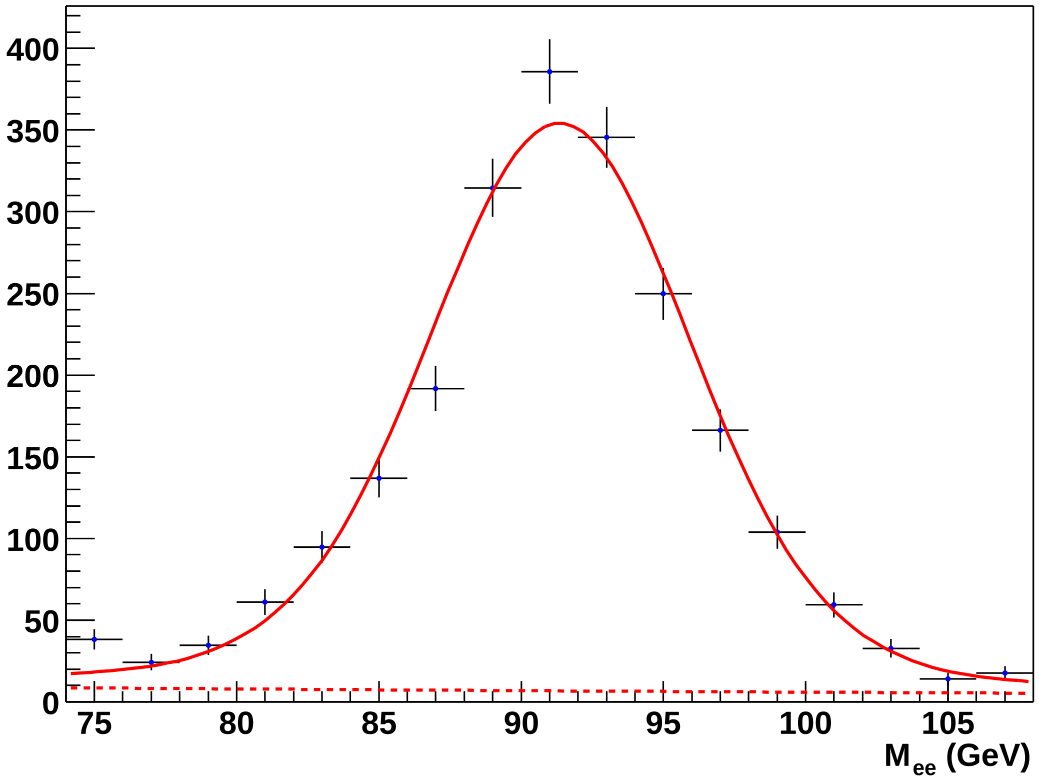

Figure 82. Diem invariant mass distribution for the $Z/\gamma^* \to e^+e^- + \geq 1$ jet sample. The solid line shows a Gaussian plus Breit-Wigner fit to the Z peak. The dashed line shows an exponential fit to the QCD and Drell-Yan contribution.

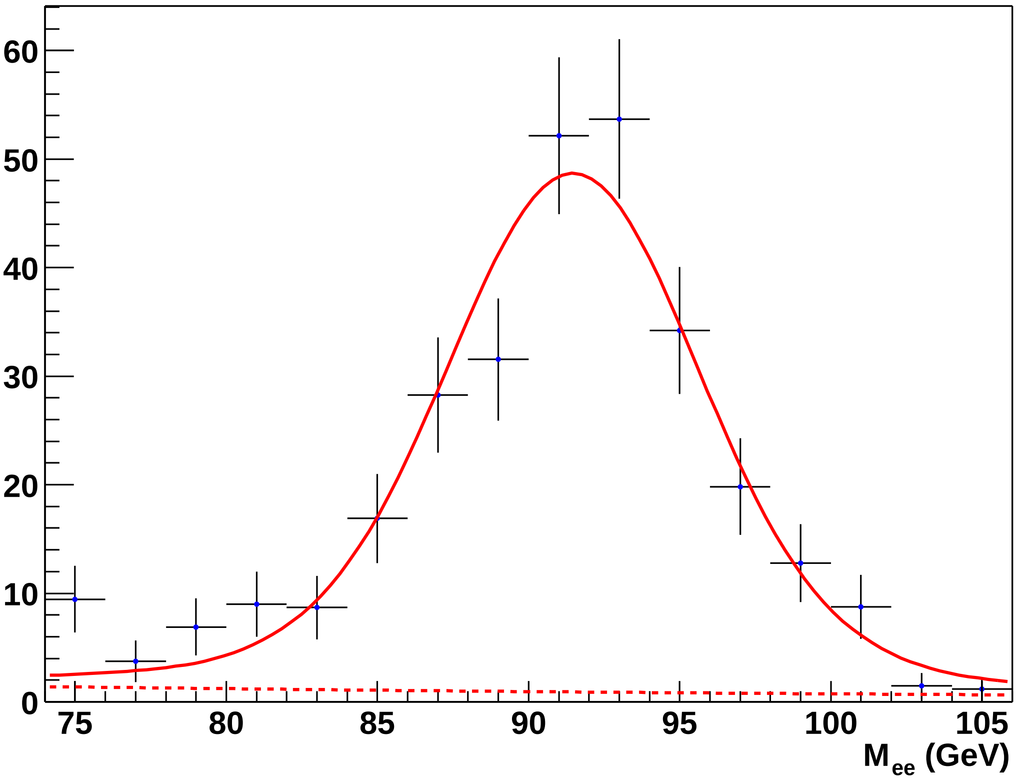

Figure 83. Diem invariant mass distribution for the $Z/\gamma^* \rightarrow e^+e^- + \geq 2$ jet sample. The solid line shows a Gaussian plus Breit-Wigner fit to the Z peak. The dashed line shows an exponential fit to the QCD and Drell-Yan contribution.

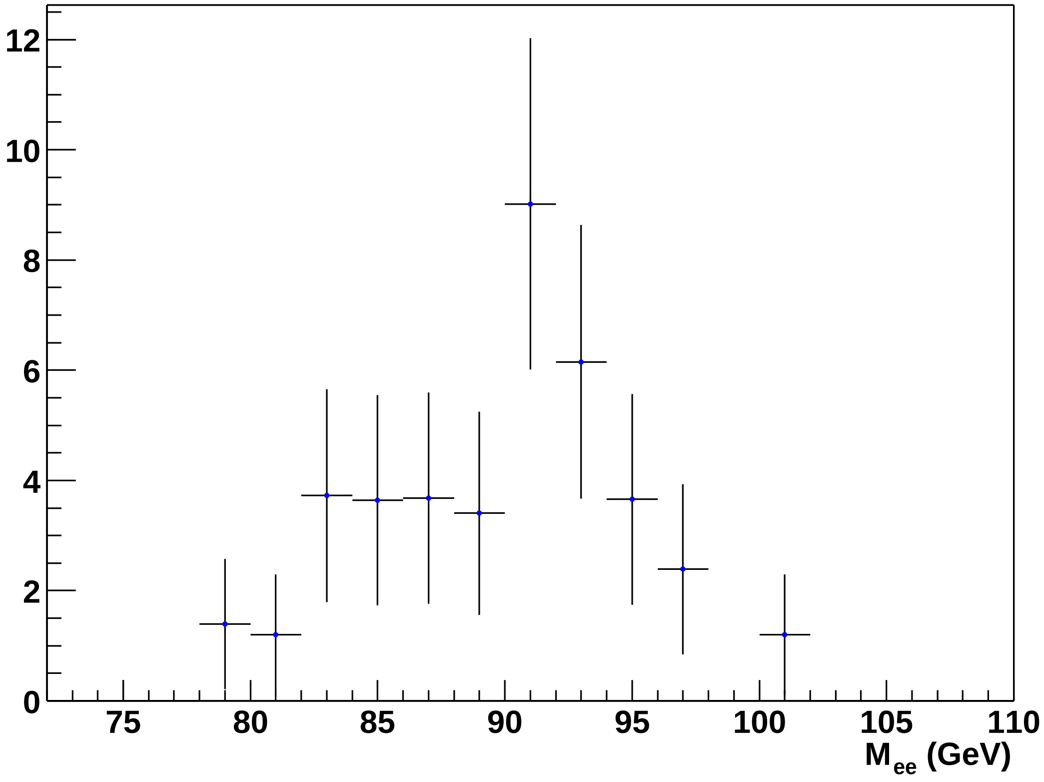

Figure 84. Diem invariant mass distribution for the $Z/\gamma^* \rightarrow e^+e^- + \geq 3$ jet sample.

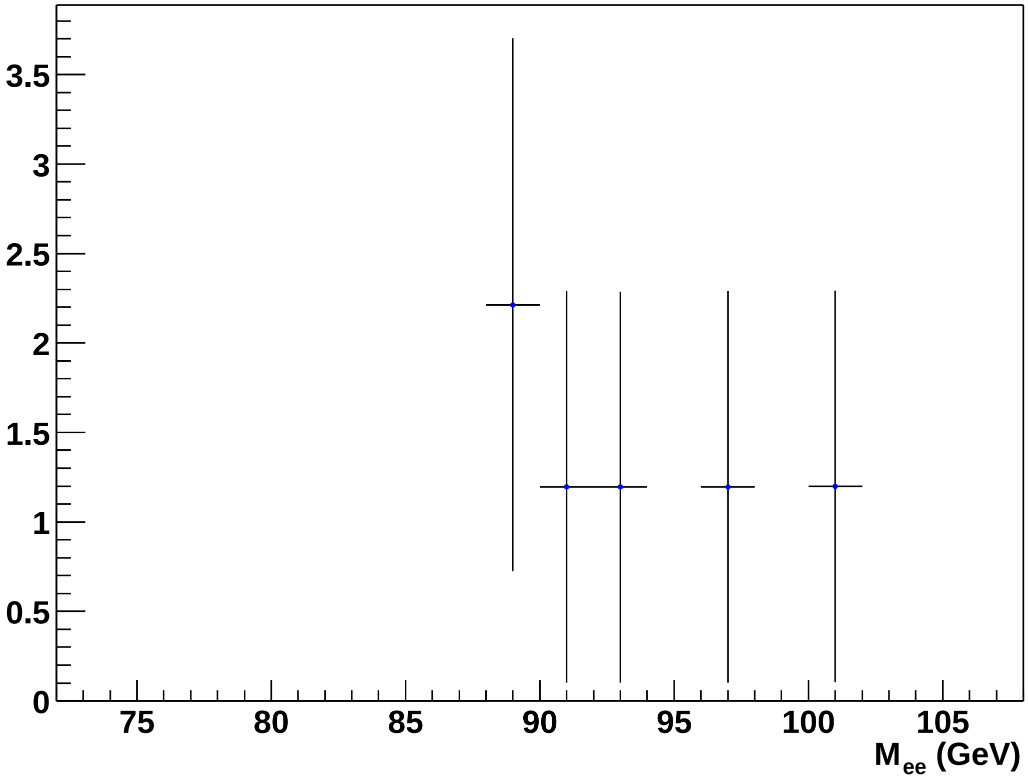

Figure 85. Diem invariant mass distribution for the $Z/\gamma^* \rightarrow e^+e^- + \geq 4$ jet sample.

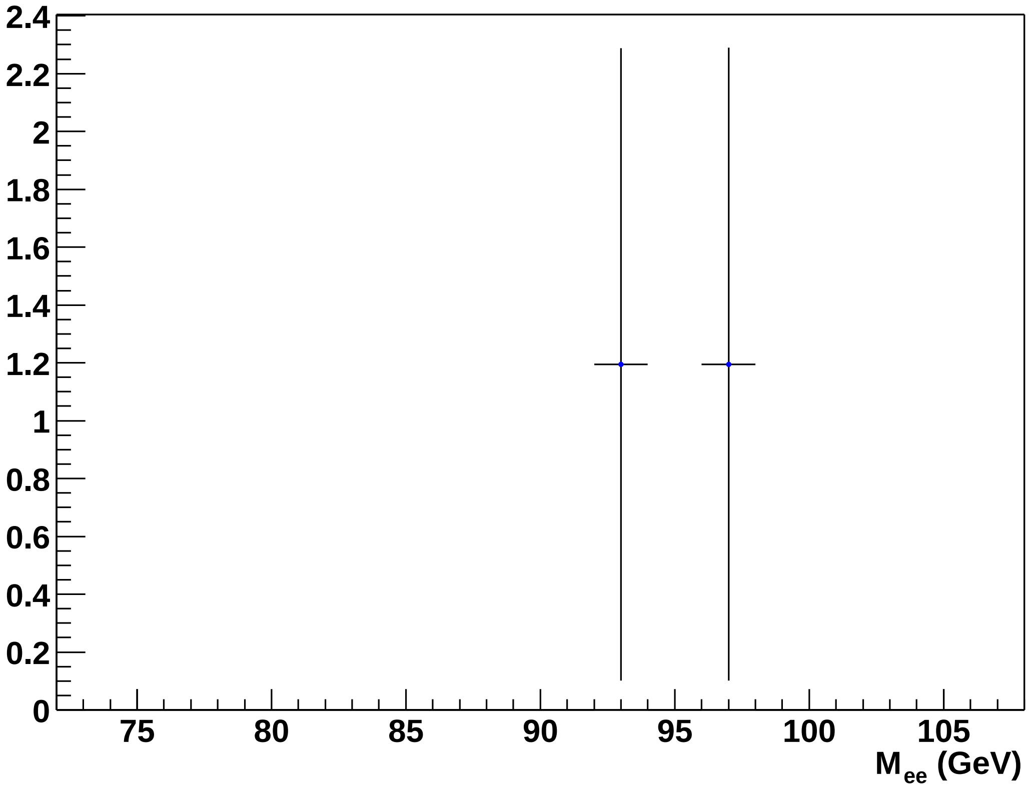

Figure 86. Diem invariant mass distribution for the $Z/\gamma^* \to e^+e^- + \geq 5$ jet sample.

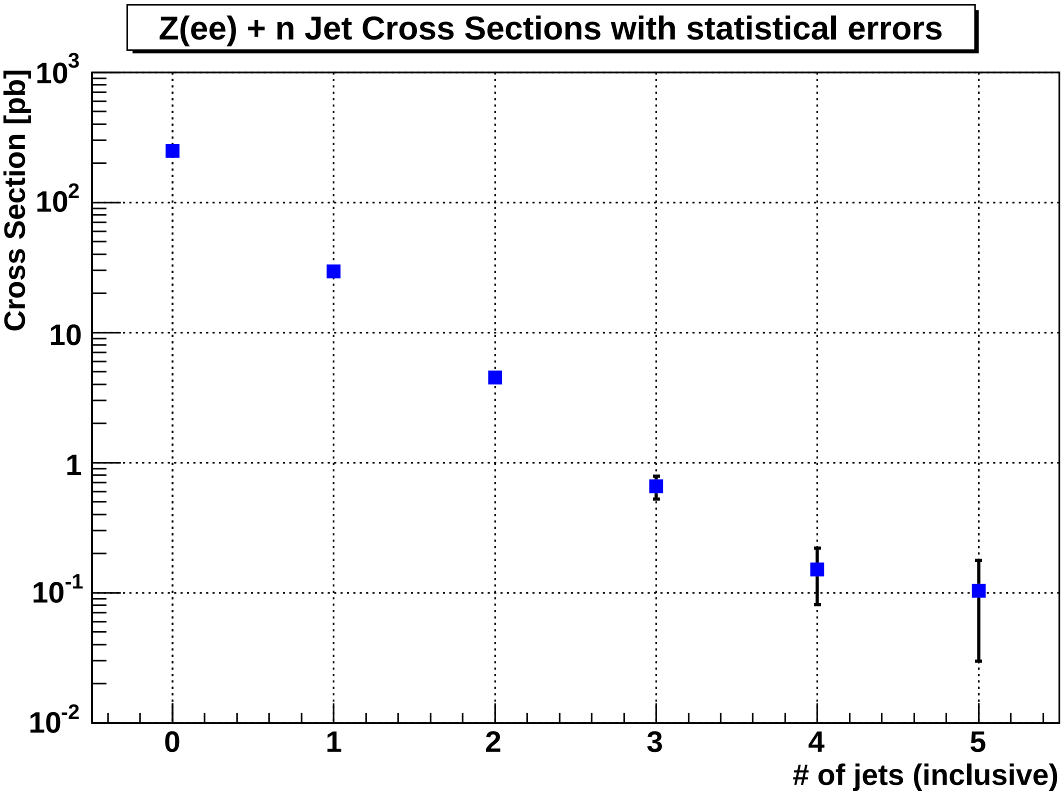

Figure 87. Fully corrected $Z/\gamma^*(\rightarrow e^+e^-)+\geq n$ jet cross sections with statistical uncertainties.

Jet Multiplicity	Signal	Background
≥ 1	2,550.7 (52.5)	74.6
≥ 2	391.9 (8.1)	12.5
≥ 3	61.6 (1.3)	3.1
≥ 4	14.8 (0.3)	0.5
≥ 5	10.8 (0.2)	0.2

TABLE XIII

NUMBER OF FULLY CORRECTED AND UNSMEARED SIGNAL EVENTS (DRELL-YAN IN PARENTHESIS) AND NUMBER OF BACKGROUND EVENTS FOR DIFFERENT JET MULTIPLICITIES.

CHAPTER 10

SYSTEMATICS

In this chapter various sources for systematic uncertainties to the $Z + n$ jet cross section measurement are evaluated.

10.1 Jet Energy Scale Systematic Uncertainty

The uncertainty due to the jet energy scale (version 5.3) is estimated by varying the energy scale correction up and down by 1σ (combined systematic and statistical JES uncertainty) and subsequently recalculating the diem invariant mass histograms (corrected for trigger, EM reco/ID, and EM-Track matching inefficiencies) to get the number of corrected signal events for different jet multiplicities. After this step, the cross sections are recalculated to estimate the JES uncertainty. Figure 88 shows the effect of the JES uncertainty on the corrected jet multiplicity distribution.

Table XIV summarizes the JES uncertainties. The JES is the dominant source of uncertainty in this analysis.

10.2 Systematic Uncertainty of Cross Section Unfolding

A detailed description of the jet reco/ID efficiency uncertainties can be found in Reference (68). Figure 89, Figure 90 and Figure 91 show the jet reco/ID efficiencies with uncertainty bands for central, ICR, and forward rapidities. To estimate the jet reco/ID uncertainty, the unsmearing and jet reco/ID correction factors are rederived using the upper and lower uncer-

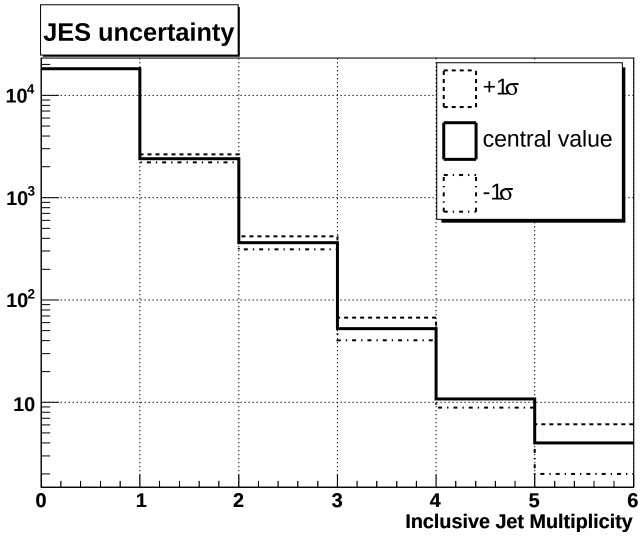

Figure 88. ±1σ fluctuation of the jet energy scale (JES 5.3). The distributions are normalized with respect to the number of events in the 0-jet bin.

Jet multiplicity	Cross Section	JES Uncertainties
≥ 1	29.6 pb	±2.9 pb
≥ 2	4.50 pb	±0.83 pb
≥ 3	0.655 pb	±0.185 pb
≥ 4	0.151 pb	±0.057 pb
≥ 5	0.1035 pb	±0.0520 pb

TABLE XIV

FINAL CROSS SECTIONS WITH JET ENERGY SCALE UNCERTAINTIES.

Jet multiplicity	Cross Section	Jet Reco/ID Uncertainties
≥ 1	29.6 pb	$^{+2.2}_{-1.6}$pb
≥ 2	4.50 pb	$^{+0.64}_{-0.57}$pb
≥ 3	0.655 pb	$^{+0.109}_{-0.105}$pb
≥ 4	0.157 pb	$^{+0.041}_{-0.028}$pb
≥ 5	0.1035 pb	$^{+0.0567}_{-0.0287}$pb

TABLE XV

FINAL CROSS SECTIONS WITH JET RECO/ID UNCERTAINTIES.

tainty bands of the jet reco/ID efficiencies. Table XV summarizes the jet reco/ID uncertainties.

The parameterization of the jet energy resolution used in this analysis is based on JES 5.0 with T42 applied (see Chapter 7.2.1). The difference between JES 5.0 and a later parameterization (JES 5.3) is taken into account as an additional systematic uncertainty. The estimation of the systematic uncertainty is based on a comparison between JES 5.1 (equivalent to JES 5.0) and JES 5.3 parameterizations (Figure 92). The comparison shows a difference of approximately 5% between JES 5.1 and 5.3 (69). A conservative uncertainty of 10% is assigned to account for this difference. Subsequently, the uncertainty due to jet energy resolution smearing in the unsmearing procedure is derived by varying the data jet energy resolution by ± 10%. Table XVI summarizes the jet resolution uncertainties.

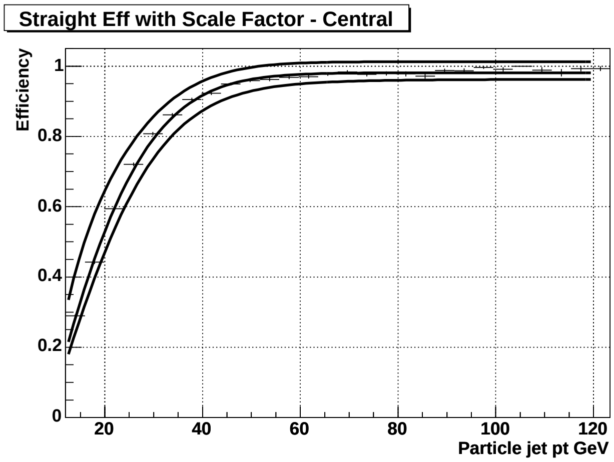

Figure 89. Jet reco/ID efficiencies with uncertainties plotted versus particle jet p_T smeared with data energy resolution (central).

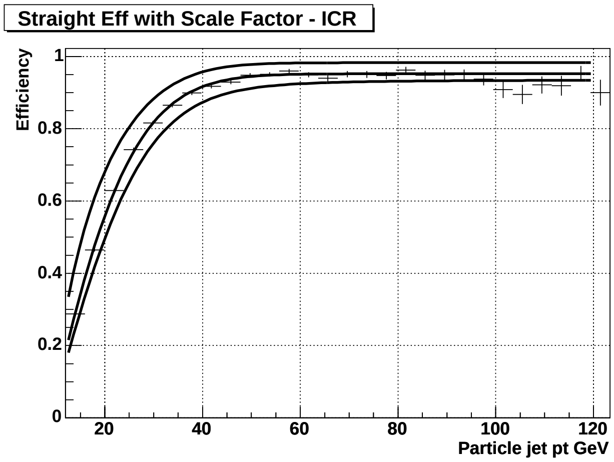

Figure 90. Jet reco/ID efficiencies with uncertainties plotted versus particle jet p_T smeared with data energy resolution (ICR).

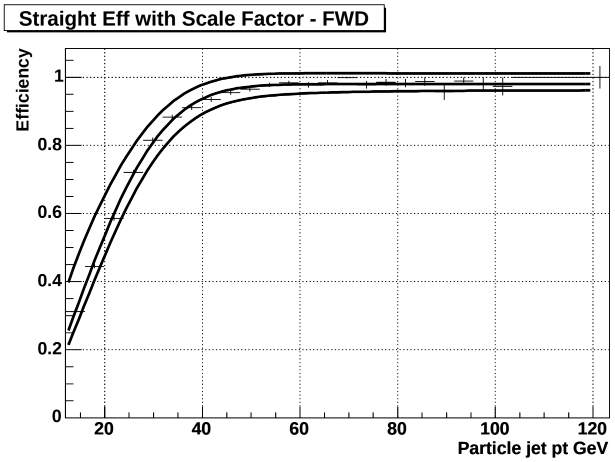

Figure 91. Jet reco/ID efficiencies with uncertainties plotted versus particle jet p_T smeared with data energy resolution (forward).

Jet Multiplicity	Cross Section	Jet Energy Resolution Uncertainties
≥ 1	29.6 pb	±0.5 pb
≥ 2	4.50 pb	±0.14 pb
≥ 3	0.655 pb	±0.017 pb
≥ 4	0.151 pb	±0.014 pb
≥ 5	0.1035 pb	±0.0681 pb

TABLE XVI

FINAL CROSS SECTIONS WITH JET ENERGY RESOLUTION UNCERTAINTIES.

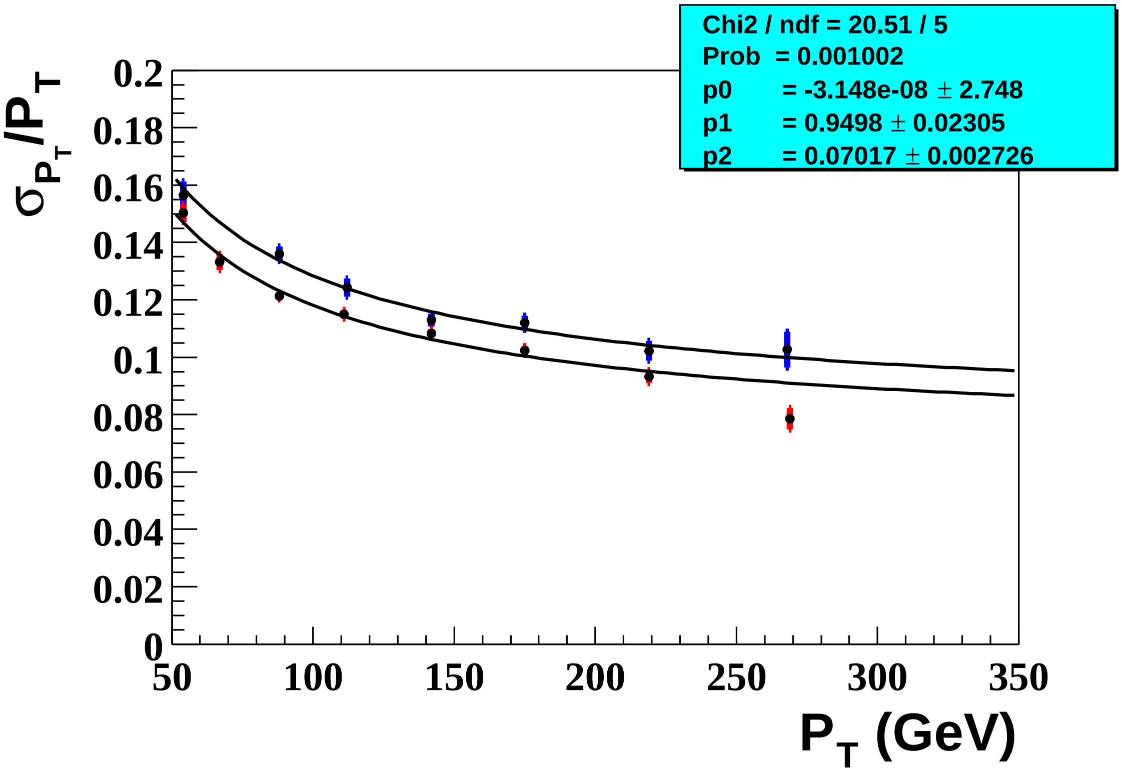

Figure 92. Comparison of jet energy resolution for JES 5.1 (upper curve) and JES 5.3 (lower curve) in the central region of the Calorimeter. The difference is approximately 5% over the whole range.

Jet Multiplicity	Cross Section	Electron-jet-overlap Uncertainties
≥ 1	29.6 pb	±0.8 pb
≥ 2	4.50 pb	±0.17 pb
≥ 3	0.655 pb	±0.032 pb
≥ 4	0.151 pb	±0.009 pb
≥ 5	0.1035 pb	±0.0071 pb

TABLE XVII

FINAL CROSS SECTIONS WITH ELECTRON-JET-OVERLAP CUT UNCERTAINTIES.

10.3 Electron-Jet-Overlap Systematic Uncertainty

For each jet multiplicity, electron-jet-overlap correction factors are derived using ΔR=0.4 and ΔR=0.7 rejection cones and taking the middle value as the final correction. The systematic uncertainty is estimated by the difference between the middle values and the correction factors derived with ΔR=0.4 and ΔR=0.7.

Table XVII summarizes the systematic uncertainties for the electron-jet-overlap cut.

10.4 Luminosity Systematic Uncertainty

The uncertainty due to the uncertainty in the luminosity measurement is 6.5% (21). Table XVIII summarizes the luminosity uncertainties.

10.5 Systematic Uncertainty Due to Efficiencies

In the following, the systematic uncertainties of the object based efficiencies are taken from Chapters 9.1.1 to 9.1.3, converted into event based systematic uncertainties, and then propagated to the cross sections.

Jet multiplicity	Cross Section	Luminosity Uncertainties
≥ 0	248.9 pb	±16.2 pb
≥ 1	29.6 pb	±1.9 pb
≥ 2	4.50 pb	±0.29 pb
≥ 3	0.655 pb	±0.043 pb
≥ 4	0.151 pb	±0.010 pb
≥ 5	0.1035 pb	±0.0067 pb

TABLE XVIII

FINAL CROSS SECTIONS WITH LUMINOSITY UNCERTAINTIES.

10.5.1 Trigger Efficiency

A relative systematic uncertainty to the cross section of ±1% is estimated due to the variations in the trigger efficiencies versus jet multiplicity (see Chapter 9.1.1). The uncertainties are estimated based on the following equations:

$$\varepsilon_{Object}(\text{pre-v12, inclusive sample}) = 94.6\%, \quad \delta\varepsilon_{Object} = 5\% \tag{10.1}$$

$$\varepsilon_{Event} = 2 \cdot \varepsilon_{Object} - \varepsilon^2_{Object} = 99.7\% \tag{10.2}$$

$$\delta\varepsilon_{Event}(-1\sigma) = 2 \cdot (\varepsilon_{Object} - \delta\varepsilon_{Object}) - (\varepsilon_{Object} - \delta\varepsilon_{Object})^2 = 98.9\% \tag{10.3}$$

$$\text{Relative Uncertainty} = \frac{99.7\% - 98.9\%}{99.7\%} = 0.8\% \approx 1\%. \tag{10.4}$$

10.5.2 EM Reconstruction and Identification Efficiency

A relative systematic uncertainty to the cross section of ±7% is assumed due to the variations in the EM reco and ID efficiencies versus jet multiplicity (see Chapter 9.1.2). The uncertainties are estimated based on the following equations:

$$\varepsilon_{Object}(\text{data, inclusive sample}) = 88.9\%, \quad \delta\varepsilon_{Object} = 3\% \tag{10.5}$$

$$\varepsilon_{Event} = \varepsilon^2_{Object} = 79.0\% \tag{10.6}$$

$$\delta\varepsilon_{Event}(-1\sigma) = (\varepsilon_{Object} - \delta\varepsilon_{Object})^2 = 73.8\% \tag{10.7}$$

$$\text{Relative Uncertainty} = \frac{79.0\% - 73.8\%}{79.0\%} = 6.6\% \approx 7\%. \tag{10.8}$$

10.5.3 EM-Track Match Efficiency

Table XIX summarizes the relative systematic uncertainties to the cross section due to the variations in the EM-Track matching efficiencies versus jet multiplicity (see Chapter 9.1.3). The uncertainties are estimated based on the following equations:

$$\varepsilon_{Object}(\text{data, n-jet sample}) = \varepsilon_n, \quad \delta\varepsilon_{Object}(\text{data, n-jet sample}) = \delta\varepsilon_n \tag{10.9}$$

$$\varepsilon_{Event} = 2 \cdot \varepsilon_n - \varepsilon^2_n \tag{10.10}$$

$$\delta\varepsilon_{Event}(-1\sigma) = 2 \cdot (\varepsilon_n - \delta\varepsilon_n) - (\varepsilon_n - \delta\varepsilon_n)^2 \tag{10.11}$$

Jet Multiplicity	Relative Uncertainty
≥ 1	0.5%
≥ 2	1.5%
≥ 3	2.3%
≥ 4	3.7%
≥ 5	5.5%

TABLE XIX

RELATIVE UNCERTAINTIES DUE TO UNCERTAINTY IN EM-TRACK MATCHING EFFICIENCIES.

$$\text{Relative Uncertainty} = \frac{\varepsilon_{Event} - \varepsilon_{Event}(-1\sigma)}{\varepsilon_{Event}}. \tag{10.12}$$

10.5.4 Overall Efficiency Systematic Uncertainty

Table XX summarizes the overall systematic uncertainties of the cross sections versus jet multiplicity due to the efficiencies after adding all contributions in quadrature.

10.6 Jet Promotion Systematic Uncertainty

The measurement of the $Z/\gamma^* \rightarrow e^+e^- + \geq n$ jet cross section depends on a precise determination of jet multiplicities for each event. Therefore, the effect of additional jets from multiple interactions within the same beam crossing (*jet promotion*) is studied. Jet multiplicities of events that have exactly one reconstructed primary vertex are compared with events that have at least two reconstructed primary vertices (Table XXI).

The two samples are normalized with respect to the number of events in the inclusive jet

Jet Multiplicity	Cross Section	Efficiency Uncertainties
≥ 1	29.6 pb	±2.1 pb
≥ 2	4.50 pb	±0.32 pb
≥ 3	0.655 pb	±0.047 pb
≥ 4	0.151 pb	±0.011 pb
≥ 5	0.1035 pb	±0.0093 pb

TABLE XX

OVERALL SYSTEMATIC UNCERTAINTIES DUE TO EFFICIENCIES (TRIGGER, EM, TRACKING).

Jet multiplicity	Exactly one primary vertex	At least two primary vertices
≥ 0	5,900	5,900
≥ 1	705	696
≥ 2	92	97
≥ 3	11	16
≥ 4	3	1
≥ 5	1	1

TABLE XXI

NUMBER OF EVENTS FOR DIFFERENT INCLUSIVE JET MULTIPLICITIES WHEN REQUIRING EXACTLY ONE RECONSTRUCTED PRIMARY VERTEX AND AT LEAST TWO RECONSTRUCTED PRIMARY VERTICES. ENTRIES ARE NORMALIZED WITH RESPECT TO THE 2 VERTEX SAMPLE.

Jet multiplicity	Average number of primary vertices
≥ 1	1.583 ± 0.852
≥ 2	1.622 ± 0.911
≥ 3	1.733 ± 0.814
≥ 4	1.4 ± 0.8
≥ 5	2.0 ± 1.0

TABLE XXII

AVERAGE NUMBER OF RECONSTRUCTED PRIMARY VERTICES FOR DIFFERENT JET MULTIPLICITIES.

multiplicity bin. Initially the single vertex sample contains 7,848 events and the 2 (or more) vertex sample contains 5,900 events.

The jet promotion effect is small since the discrepancy between the two samples is within the statistical uncertainty.

Table XXII shows the average number of reconstructed primary vertices for different jet multiplicity samples. Since this number does not change statistically versus jet multiplicity, a bias due to additional $p\bar{p}$ interactions should be negligible.

10.7 Statistical Uncertainty

The statistical uncertainty of the cross sections includes the following components:

- The uncertainty due to the total number of corrected events $\delta\mathrm{N}_{corr}$ (corrected for Trigger, EM and Tracking inefficiencies) is estimated based on the following equations:

$$\mathrm{N}_{corr} = \mathrm{w}_{average} \cdot \mathrm{N}_{uncorr} \tag{10.13}$$

$$\Rightarrow \quad \delta\mathrm{N}_{corr} = \sqrt{(\mathrm{w}_{average} \cdot \delta\mathrm{N}_{uncorr})^2 + (\mathrm{N}_{uncorr} \cdot \delta\mathrm{w}_{average})^2}, \tag{10.14}$$

where N_{corr} is the total number of corrected events, N_{uncorr} is the total number of uncorrected events, and $\mathrm{w}_{average}$ is the average weight used to correct for EM, Trigger and Tracking inefficiencies (≈1.36).

- The uncertainty due to the number of background events δB is estimated by fitting an exponential function $a \cdot \exp(\ b \cdot \mathrm{x}\ )$ to the measured number of QCD events (Figure 93), and then propagating the uncertainty of the two fitting parameters a and b. The uncertainty of the exponential fit takes into account that the fitting parameters a and b are correlated:

$$f(x) = a \cdot exp(b \cdot x) \tag{10.15}$$

$$\delta f(x) = \sqrt{\left(\frac{\partial f}{\partial a} \cdot \delta a\right)^2 + \left(\frac{\partial f}{\partial b} \cdot \delta b\right)^2 + 2 \cdot \frac{\partial f}{\partial a} \cdot \frac{\partial f}{\partial b} \cdot covariance(a, b)}. \tag{10.16}$$

- The statistical uncertainty of the acceptances (see Table X).
- The statistical uncertainty due to the unsmearing and jet reco/ID coefficients (see Chapter 9.2.1). This component is only relevant for jet multiplicities ≥ 1.

Table XXIII summarizes the statistical uncertainties.

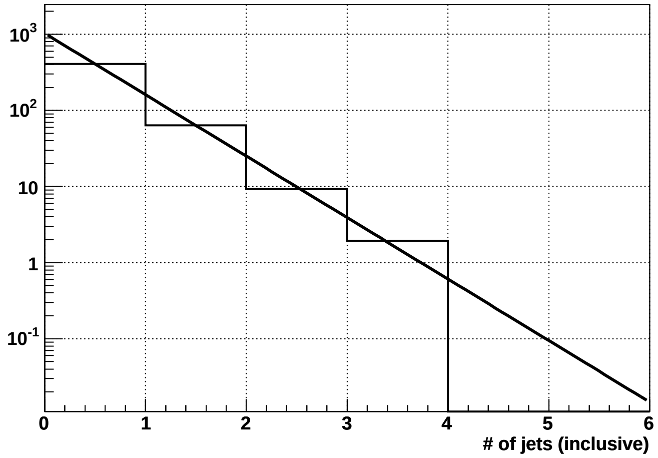

Figure 93. Exponential fit to the number of background events for different inclusive jet multiplicities.

Jet Multiplicity	Cross Section	Total Statistical Uncertainty
≥ 0	248.9 pb	±2.5 pb
≥ 1	29.6 pb	±0.8 pb
≥ 2	4.50 pb	±0.32 pb
≥ 3	0.655 pb	±0.129 pb
≥ 4	0.151 pb	±0.070 pb
≥ 5	0.1035 pb	±0.0738 pb

TABLE XXIII

CROSS SECTIONS WITH TOTAL STATISTICAL UNCERTAINTIES TO THE CROSS SECTIONS.

CHAPTER 11

CONCLUSIONS

The $Z/\gamma^*(\rightarrow e^+e^-)+\geq n$ jet cross sections for jet multiplicities of 0 to 5 have been measured. The results are presented in terms of absolute cross sections and cross section ratios normalized with respect to the inclusive cross section.

Table XXIV summarizes all measured cross sections, together with uncertainties due to statistics, systematics, and luminosity. Also listed is the number of fully corrected signal events for each jet multiplicity sample. The measured cross sections with results from MCFM and CKKW theory predictions (see Chapter 7.2) are compared in Table XXV and Figure 94. The CKKW cross sections are normalized with respect to the measured cross section for the 1-jet sample. The matrix element generation of the CKKW samples was done up to jet multiplicities of 3. Higher jet multiplicities are due to parton showering and hadronization simulated with PYTHIA.

The cross section ratios with results from MCFM and CKKW MC simulations are compared in Table XXVI and Figure 95. For cross section ratios, R_n, the luminosity measurement uncertainties cancel. All other systematic uncertainties contribute as shown in the following equation:

$$\delta R_n = \frac{\delta\sigma_n}{\sigma_0}, \quad \text{with} \quad \sigma_0 = 248.9\ pb. \tag{11.1}$$

Jet Multiplicity	# of Signal Events	$Z/\gamma^*(\rightarrow e^+e^-)+\geq n$ Jet Cross Section
≥ 0	18,263.8	248.9 pb ± 2.5(stat) ± 16.2(lumi)
≥ 1	2,550.7	29.6 pb ± 0.81(stat) $^{+4.3}_{-4.0}$(sys) ± 1.9(lumi)
≥ 2	391.9	4.50 pb ± 0.32(stat) $^{+1.1}_{-1.1}$(sys) ± 0.29(lumi)
≥ 3	61.6	0.655 pb ± 0.13(stat) $^{+0.22}_{-0.22}$(sys) ± 0.043(lumi)
≥ 4	14.8	0.151 pb ± 0.070(stat) $^{+0.072}_{-0.066}$(sys) ± 0.010(lumi)
≥ 5	10.8	0.104 pb ± 0.074(stat) $^{+0.10}_{-0.06}$(sys) ± 0.0067(lumi)

TABLE XXIV

CROSS SECTIONS FOR DIFFERENT INCLUSIVE JET MULTIPLICITIES. NUMBER OF SIGNAL EVENT ENTRIES HAVE UNSMEARING, JET RECO/ID AND ELECTRON-JET-OVERLAP CORRECTIONS APPLIED.

Jet p_T distributions for different jet multiplicities are compared between data and ALPGEN+PYTHIA simulations (Figure 96).

The results are in good agreement with QCD predictions.

Jet Multiplicity	Measured Cross Section	MCFM	CKKW
≥ 0	248.9 pb ±16.4(tot)	241.5 pb ±0.1(stat)	-
≥ 1	29.6 pb $^{+4.8}_{-4.6}$(tot)	26.2 pb ±0.044(stat)	29.6 pb
≥ 2	4.50 pb $^{+1.2}_{-1.2}$(tot)	5.21 pb ±0.069(stat)	5.22 pb
≥ 3	0.655 pb $^{+0.26}_{-0.26}$(tot)	-	0.798 pb
≥ 4	0.151 pb $^{+0.10}_{-0.10}$(tot)	-	0.096 pb
≥ 5	0.104 pb $^{+0.13}_{-0.10}$(tot)	-	0.008 pb

TABLE XXV

COMPARISON OF MEASURED CROSS SECTIONS WITH RESULTS FROM MCFM AND CKKW.

Jet multiplicity	$\frac{\sigma(Z/\gamma^*(\rightarrow e^+e^-)+\geq nJets)}{\sigma_{Z/\gamma^*}}$ $[\cdot 10^{-3}]$	MCFM	CKKW
≥ 1	119.1 ±3.3(stat) $^{+17.2}_{-16.2}$(sys)	108.4	119.1
≥ 2	18.1 ±1.3(stat) $^{+4.5}_{-4.3}$(sys)	21.6	21.0
≥ 3	2.6 ±0.52(stat) $^{+0.90}_{-0.89}$(sys)	-	3.2
≥ 4	0.61 ±0.28(stat) $^{+0.29}_{-0.27}$(sys)	-	0.39
≥ 5	0.42 ±0.30(stat) $^{+0.42}_{-0.24}$(sys)	-	0.03

TABLE XXVI

COMPARISON OF MEASURED CROSS SECTION RATIOS WITH RESULTS FROM MCFM AND CKKW.

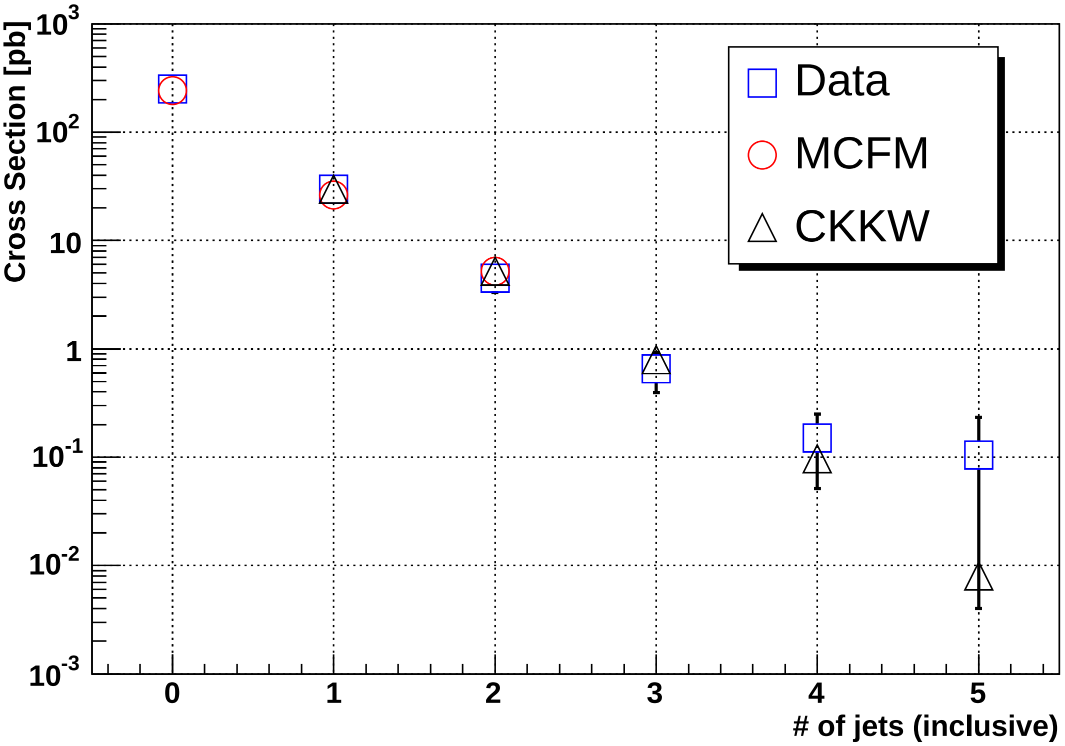

Figure 94. $Z/\gamma^*(\rightarrow e^+e^-)+\geq n$ jet cross sections in data (with total uncertainties) compared with MCFM and CKKW.

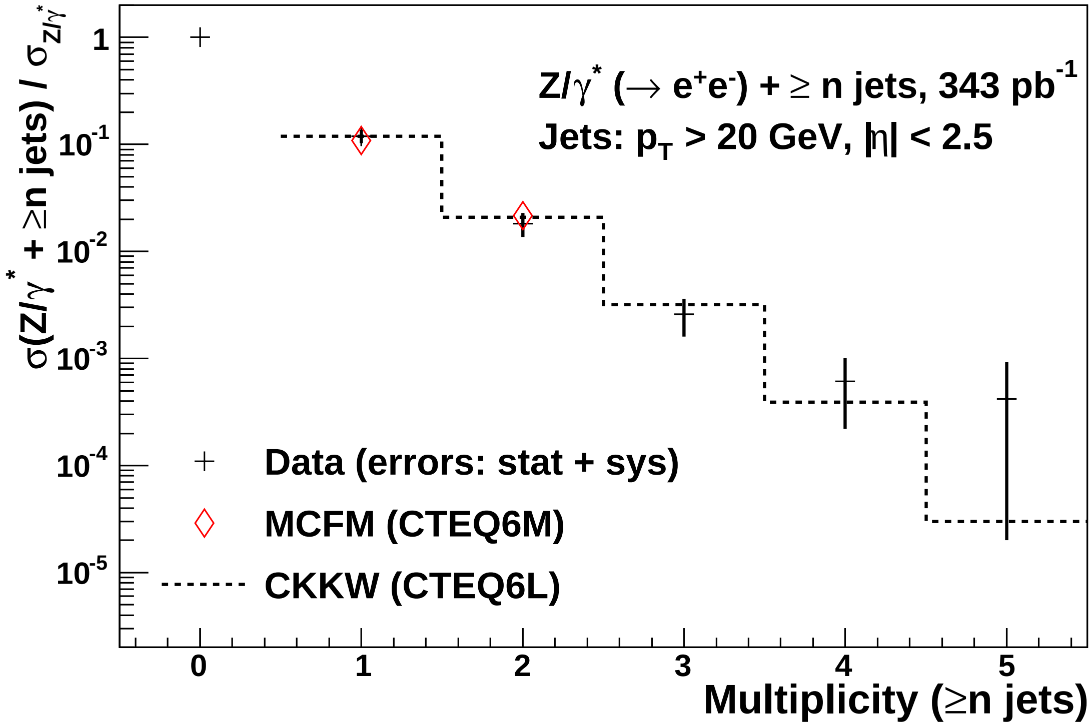

Figure 95. Ratios of the $Z/\gamma^*(\rightarrow e^+e^-)+\geq n$ jet cross sections to the total inclusive $Z/\gamma^* \rightarrow e^+e^-$ cross section versus n. The uncertainties on the data include the combined statistical and systematic uncertainties. The dashed line (CKKW) represents the predictions of LO matrix element calculations using PYTHIA for parton showering and hadronization, normalized to the measured $Z/\gamma^*+\geq 1$ jet cross section ratio. The diamonds represent the MCFM predictions.

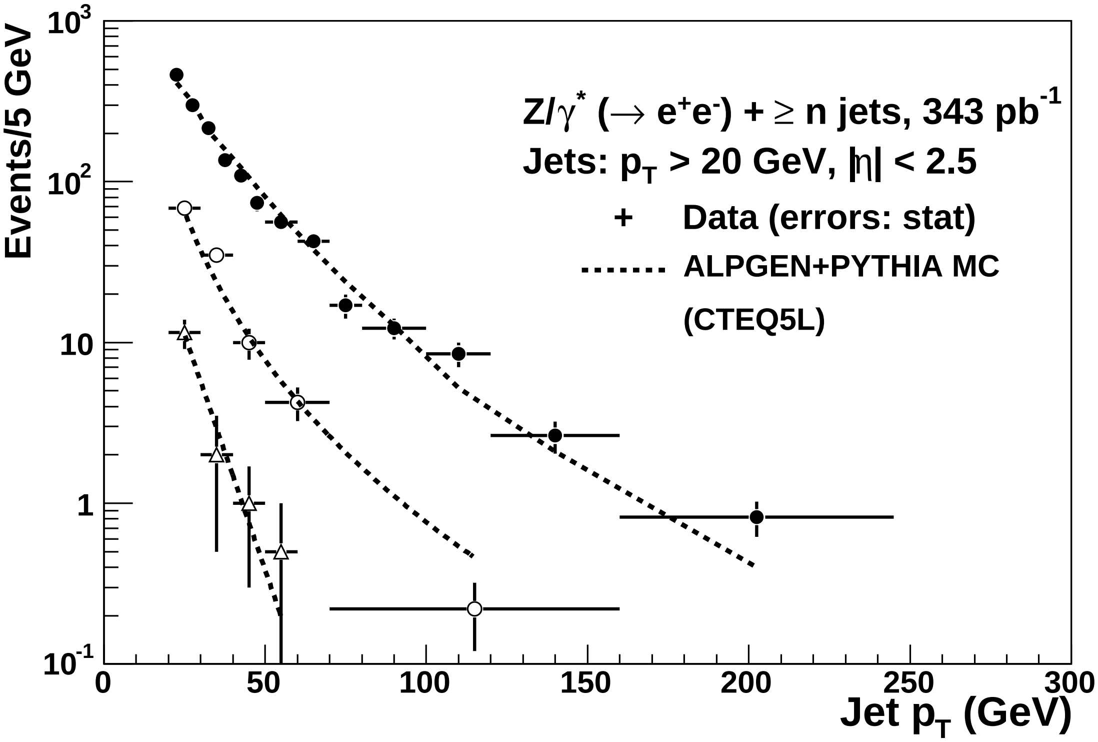

Figure 96. Data to theory (ALPGEN+PYTHIA) comparison for the highest p_T jet distribution in the $Z+ \geq 1$ jet sample (●), for the second highest p_T jet distribution in the $Z+ \geq 2$ jet sample (○), and for the third highest p_T jet distribution in the $Z+ \geq 3$ jet sample (△). The uncertainties on the data are only statistical.

APPENDICES

Appendix A

THE DØ COLLABORATION

R. Piegaia

Universidad de Buenos Aires, Buenos Aires, Argentina

G.A. Alves, J. Barreto, H. da Motta, M.-E. Pol, M.S. Rangel, F.A.S. Rezende, M. Souza, M. Vaz

LAFEX, Centro Brasileiro de Pesquisas Físicas, Rio de Janeiro, Brazil

A.C.S. Assis Jesus, M. Begalli, W. Carvalho, C. De Oliveira Martins, S. Greder, J.R.P. Mahon, H.B. Malbouisson, J. Molina, L. Mundim, V. Oguri, N. Oliveira, W.L. Prado da Silva, R.F. Rodrigues, A. Santoro, A. Sznajder

Universidade do Estado do Rio de Janeiro, Rio de Janeiro, Brazil

E.M. Gregores, S.M. Lietti, P.G. Mercadante, S.F. Novaes

Instituto de Física Teórica, Universidade Estadual Paulista, São Paulo, Brazil

S. Beale, C. Belanger-Champagne, K. Chan, Y. Coadou, D. Gillberg, Z. Liu, R.W. Moore, D.C. O'Neil, W. Taylor, B. Vachon, M.C. Vetterli

University of Alberta, McGill University, Simon Fraser University and York University, Canada

H.S. Mao

Institute of High Energy Physics, Beijing, People's Republic of China

L. Han, J. Yi

University of Science and Technology of China, Hefei, People's Republic of China

C. Avila, B. Gómez, D. Mendoza, J.P. Negret, R. Ramirez, J.M.R. Roldan

Universidad de los Andes, Bogotá, Colombia

V. Hynek, J. Kvita, R. Leitner, K. Soustruznik

Charles University, Center for Particle Physics, Prague, Czech Republic

P. Homola, Z. Hubacek, R. Otec, V. Simak, P. Vokac

Czech Technical University, Prague, Czech Republic

A. Kupco, M. Lokajicek, V. Vrba

Institute of Physics, Academy of Sciences, Center for Particle Physics, Prague, Czech Republic

B. Hoeneisen

Universidad San Francisco de Quito, Quito, Ecuador

F. Badaud, P. Gay, Ph. Gris, V. Lesne, F. Tissandier

Laboratoire de Physique Corpusculaire, IN2P3-CNRS, Université Blaise Pascal, Clermont-Ferrand, France

Y. Arnoud, F. Chevallier, S. Crépé-Renaudin, A.-M. Magnan, G. Sajot, J. Stark, C. Yu

Laboratoire de Physique Subatomique et de Cosmologie, IN2P3-CNRS, Université de Grenoble, Grenoble, France

L. Berntzon, S. Calvet, M.-C. Cousinou, A. Duperrin, E. Kajfasz, S. Kermiche, A. Mendes, E. Nagy, M. Talby

CPPM, IN2P3-CNRS, Université de la Méditerranée, Marseille, France

L. Duflot, J.-F. Grivaz, M. Jaffré, N. Makovec, P. Pétroff

Laboratoire de l'Accélérateur Linéaire, IN2P3-CNRS, Orsay, France

B. Andrieu, U. Bassler, G. Bernardi, E. Busato, L. Sonnenschein, S. Trincaz-Duvoid, J.-R. Vlimant

LPNHE, Universités Paris VI and VII, IN2P3-CNRS, Paris, France

M. Agelou, M. Besançon, F. Déliot, P. Demine, P. Lutz, M. Michaut, E. Perez, C. Royon, V. Shary, B. Tuchming, D. Vilanova

DAPNIA/Service de Physique des Particules, CEA, Saclay, France

J.-L. Agram, D. Bloch, F. Charles, B. Clément, A. Gay, W. Geist, D. Gelé, A.-C. Le Bihan, A. Lounis, I. Ripp-Baudot, V. Siccardi

IReS, IN2P3-CNRS, Université Louis Pasteur Strasbourg, and Université de Haute Alsace, France

N. Estre, G. Grenier, T. Kurča, P. Lebrun, J.P. Martin, T. Millet, G.S. Muanza, P. Verdier

Institut de Physique Nucléaire de Lyon, IN2P3-CNRS, Université Claude Bernard, Villeurbanne, France

C. Autermann, M. Erdmann, T. Hebbeker, D. Käfer, C. Magass, A. Meyer

RWTH Aachen, III. Physikalisches Institut A, Aachen, Germany

J. Meyer, A. Quadt, C. Schwanenberger, N. Wermes

Universität Bonn, Physikalisches Institut, Bonn, Germany

U. Blumenschein, V. Buescher, I. Fleck, H. Fox, G. Herten, K. Jakobs, J.-P. Konrath, O. Mundal, C. Noeding, M. Titov, I. Torchiani

Universität Freiburg, Physikalisches Institut, Freiburg, Germany

C. Ay, M. Hohlfeld, T. Kuhl, D. Meder, S. Tapprogge, T. Trefzger, C. Zeitnitz

Universität Mainz, Institut für Physik, Mainz, Germany

O. Biebel, M. Binder, J. Elmsheuser, F. Fiedler, P. Haefner, B. Leonhardt, T. Nunnemann,
D. Schaile, P. Schieferdecker, R. Ströhmer

Ludwig-Maximilians-Universität München, München, Germany

K. Hamacher, A. Harel, H. Hoeth, S. Kersten, P. Mättig, C. Schmitt, M. Vaupel

Fachbereich Physik, University of Wuppertal, Wuppertal, Germany

S.B. Beri, V. Bhatnagar, R. Kaur, J.M. Kohli

Panjab University, Chandigarh, India

B. Choudhary, A. Kumar, M. Naimuddin, K. Ranjan, R.K. Shivpuri

Delhi University, Delhi, India

B.S. Acharya, P. Banerjee, S. Banerjee, S. Chakrabarti, A. Chandra, S.R. Dugad, P.K. Mal,
N.K. Mondal, K.J. Rani

Tata Institute of Fundamental Research, Mumbai, India

M. Cwiok, M.W. Grünewald

University College Dublin, Dublin, Ireland

S.H. Ahn, S.J. Hong, T.J. Kim, K.S. Lee, S.K. Park

Korea Detector Laboratory, Korea University, Seoul, Korea

H. Castilla-Valdez, P.L.M. Podesta-Lerma, A. Sánchez-Hernández

CINVESTAV, Mexico City, Mexico

K. Bos, S. Caron, P. de Jong, J.G. Hegeman, P. Houben, G.G.G. Massaro, P.J. van den Berg, W.M. van Leeuwen, M. Vreeswijk

FOM-Institute NIKHEF and University of Amsterdam/NIKHEF, Amsterdam, The Netherlands

M. Anastasoaie, L.S. Ancu, S.J. de Jong, F. Filthaut, C.F. Galea, M.H. Kirby, N.A. Naumann

Radboud University Nijmegen/NIKHEF, Nijmegen, The Netherlands

V.M. Abazov, G.D. Alexeev, D.V. Bandurin, G. Erusalimtsev, G. Golovanov, A.M. Kalinin, Y.M. Kharzheev, E.V. Komissarov, V.L. Malyshev, Y.P. Merekov, S.Y. Porokhovoi, N.A. Russakovich, A.A. Shishkin, N.B. Skachkov, V.V. Tokmenin, L.S. Vertogradov, Y.A. Yatsunenko

Joint Institute for Nuclear Research, Dubna, Russia

A. Evdokimov, V. Gavrilov, P. Polozov, G. Safronov, V. Stolin, V.I. Turtikov

Institute for Theoretical and Experimental Physics, Moscow, Russia

E.E. Boos, S. Bunichev, L.V. Dudko, P. Ermolov, D. Karmanov, A. Koubarovsky, V.A. Kuzmin, A. Leflat, M. Merkin, V.I. Rud, S. Sherstnev, E.G. Zverev

Moscow State University, Moscow, Russia

V.A. Bezzubov, S.P. Denisov, S.A. Efremov, V.N. Evdokimov, A.V. Ferapontov, A.K. Klimenko, V.M. Korablev, V.I. Koreshev, A.V. Kozelov, E.A. Kozlovsky, V.V. Lipaev, A.V. Popov, A.A. Shchukin, Y.V. Sinkin, D.A. Stoyanova, I.A. Vasilyev, S.A. Zvyagintsev

Institute for High Energy Physics, Protvino, Russia

G. Alkhazov, S. Anufriev, V. Kim, A. Lobodenko, P. Neustroev, G. Obrant, Y. Scheglov, L. Uvarov, S. Uvarov

Petersburg Nuclear Physics Institute, St. Petersburg, Russia

B. Åsman, C. Clément, P. Eerola, T. Ekelöf, N. Gollub, P. Hansson, S. Lager, B. Lund-Jensen, T. Moa, J. Strandberg

Lund University, Royal Institute of Technology, Stockholm University, and Uppsala University, Sweden

M. Audsley Hammond, I. Bertram, C. Biscarat, G. Borissov, B. Davies, M. Doidge, A.J. Finch, M. Lewin, P. Love, A. Rakitine, P.N. Ratoff, A. Sopczak

Lancaster University, Lancaster, United Kingdom

C. Barnes, R. Beuselinck, I. Blackler, F. Blekman, C.P. Buszello, G. Davies, J.F. Hassard, A. Jenkins, R. Jesik, P. Jonsson, P. Lewis, L. Lobo, M. Petteni, S. Robinson, T. Scanlon, F. Villeneuve-Seguier, P. Vint

Imperial College, London, United Kingdom

B. Cox, T. Edwards, M. Ford, J. Monk, M. Owen, K. Peters, S. Söldner-Rembold, P. Telford, A.S. Turcot, T.R. Wyatt

University of Manchester, Manchester, United Kingdom

N.M. Giao, D. Han, T.M. Ngoc, H.T.K. Trang, T.D. Tu

Hochiminh City Institute of Physics, Hochiminh City, Vietnam

S. Anderson, S. Burke, E. Cheu, B. Gmyrek, K. Johns, J. Leveque, R. McCroskey, M. Shupe, P. Tamburello, J. Temple, E.W. Varnes

University of Arizona, Tucson, Arizona 85721, USA

R.J. Madaras, M. Strovink

Lawrence Berkeley National Laboratory and University of California, Berkeley, California 94720, USA

R.E. Hall

California State University, Fresno, California 93740, USA

S. Choi, R. Clare, J. Ellison, R. Gelhaus, A.P. Heinson, I. Iashvili, P.M. Perea, S.J. Wimpenny

University of California, Riverside, California 92521, USA

T. Adams, A. Askew, S. Blessing, N.J. Buchanan, D. Duggan, Y. Gershtein, S. Hagopian, V. Hagopian, D. Kau, J. Lazoflores, W.M. Lee, J. Miao, S. Nelson, H.B. Prosper, J. Sekaric, S. Sengupta, S. Sumowidagdo, S. Tentindo-Repond, H.D. Wahl

Florida State University, Tallahassee, Florida 32306, USA

B. Baldin, J.F. Bartlett, L. Bellantoni, R. Bernhard, P.C. Bhat, A. Boehnlein, A. Bross, S. Burdin, W.E. Cooper, M. Demarteau, D. Denisov, H.T. Diehl, M. Diesburg, V.D. Elvira, J. Estrada, W. Fisher, H.E. Fisk, S. Fu, S. Fuess, E. Gallas, H. Greenlee, S. Grünendahl, G. Gutierrez, K. Hanagaki, R. Illingworth, A.S. Ito, M. Johnson, A. Jonckheere, A. Juste, P. Kasper, B. Klima, F. Lehner, Q.Z. Li, D. Lincoln, R. Lipton, A.L. Lyon, Y. Maravin, M. Martens, K.W. Merritt, M. Mulders, A. Nomerotski, V. O'Dell, N. Oshima, V.M. Podstavkov, P. Rubinov, G. Savage, V. Sirotenko, R.P. Smith, L. Stutte, M. Tomoto, M.H.L.S Wang, M. Weber, D. Wicke, M. Wobisch, J. Womersley, R. Yamada, T. Yasuda, M. Zanabria, D. Zhang

Fermi National Accelerator Laboratory, Batavia, Illinois 60510, USA

M. Adams, M. Buehler, M. Camuyrano, C.E. Gerber, J.M. Heinmiller, G.J. Otero y Garzón, E. Shabalina, A. Stone, T. Ten, N. Varelas

University of Illinois at Chicago, Chicago, Illinois 60607, USA

L. Bagby, G. Blazey, D. Chakraborty, A. Dyshkant, M. Eads, M. Fortner, D. Hedin, J.G.R. Lima, A.K.A. Maciel, X. Song, N.M. Tran, S. Uzunyan, A. Zatserklyaniy, V. Zutshi

Northern Illinois University, DeKalb, Illinois 60115, USA

T. Andeen, D. Buchholz, G.A. Davis, M. Gagliardi, J. Hays, H. Schellman, D. Strom, S. Yacoob, S.W. Youn

Northwestern University, Evanston, Illinois 60208, USA

R. Abrams, D. Bauer, J. Rieger, K. Stevenson, R. Van Kooten, L. Welty, D. Zieminska, A. Zieminski

Indiana University, Bloomington, Indiana 47405, USA

O. Boeriu, N.M. Cason, E. Galyaev, A. Goussiou, M.D. Hildreth, D. Karmgard, A. Kharchilava, D. Lam, H. Luo, M. Lynker, J. Osta, Y. Pogorelov, R. Ruchti, W.D. Shephard, P. Svoisky, J. Torborg, J. Warchol, M. Wayne, N. Xuan

University of Notre Dame, Notre Dame, Indiana 46556, USA

O. Atramentov, J.M. Hauptman

Iowa State University, Ames, Iowa 50011, USA

P. Baringer, A. Bean, L. Christofek, D. Coppage, J. Gardner, C. Hensel, S. Jabeen, T. Moulik, G.W. Wilson

University of Kansas, Lawrence, Kansas 66045, USA

M. Ahsan, T.A. Bolton, K. Harder, D. Onoprienko, F. Rizatdinova, M. Shamim, R.A. Sidwell, M. Smith, E. Von Toerne

Kansas State University, Manhattan, Kansas 66506, USA

M. Das, Z.D. Greenwood, N. Parashar, L. Sawyer, J. Steele

Louisiana Tech University, Ruston, Louisiana 71272, USA

A. Baden, S. Eno, N.J. Hadley, C. Jarvis, S. Kunori, J. Mans, M.P. Sanders, T. Toole, M. Verzocchi, L. Wang, M. Wetstein, M. Yan

University of Maryland, College Park, Maryland 20742, USA

K.M. Black, J.M. Butler, D.K. Cho, A. Das, S.N. Fatakia, L. Feligioni, U. Heintz, J. Kasper, M. Narain

Boston University, Boston, Massachusetts 02215, USA

G. Alverson, E. Barberis, S. Doulas, R. Harrington, G. Hesketh, S. Reucroft, D. Shpakov, D.R. Wood

Northeastern University, Boston, Massachusetts 02115, USA

A. Alton, J.D. Degenhardt, E. De La Cruz-Burelo, A. Magerkurth, H.A. Neal, J. Qian, B. Zhou

University of Michigan, Ann Arbor, Michigan 48109, USA

M. Abolins, J. Benitez, R. Brock, J. Dyer, D. Edmunds, R. Hauser, J. Kalk, J. Kozminski, J. Linnemann, J. Piper, B.G. Pope, R. Schwienhorst, R. Unalan, H. Weerts

Michigan State University, East Lansing, Michigan 48824, USA

A. Melnitchouk, B. Quinn

University of Mississippi, University, Mississippi 38677, USA

A. Bellavance, K. Bloom, D. Claes, A. Dominguez, C. Lundstedt, S. Malik, G.R. Snow, M. Voutilainen

University of Nebraska, Lincoln, Nebraska 68588, USA

J. Haley, A. Schwartzman, C. Tully, R. Wagner, J. Werner

Princeton University, Princeton, New Jersey 08544, USA

T. Bose, G. Brooijmans, H. Evans, A. Haas, C. Johnson, I. Katsanos, D. Khatidze, B. Kothari, S. Lammers, J. Mitrevski, M. Mulhearn, J. Parsons, P.M. Tuts

Columbia University, New York, New York 10027, USA

M. Begel, J. Cammin, K.M. Chan, R. Demina, T. Ferbel, C. Garcia, G. Ginther, A. Khanov, T. Negrini, S.-J. Park, M.-A. Pleier, P. Slattery, M. Zielinski

University of Rochester, Rochester, New York 14627, USA

S. Desai, H. Dong, P.D. Grannis, J. Guo, J.D. Hobbs, Y. Hu, R. McCarthy, Y.D. Mutaf,
N. Parua, M. Rijssenbeek, R.D. Schamberger, S. Towers, D. Tsybychev, A. Yurkewicz, J. Zhu

State University of New York, Stony Brook, New York 11794, USA

S. Kahn, J. Kotcher, A. Patwa, S. Protopopescu, S. Snyder, K. Yip

Brookhaven National Laboratory, Upton, New York 11973, USA

J. Snow

Langston University, Langston, Oklahoma 73050, USA

B. Abbott, P. Gutierrez, I. Hall, S. Jain, M. Kopal, A. Pompoš, H. Severini, P. Skubic,
M. Strauss

University of Oklahoma, Norman, Oklahoma 73019, USA

B.C.K. Casey, D. Chapin, D. Cutts, R. Hooper, S. Kesisoglou, G. Landsberg,
S.E.K. Mattingly, R. Partridge, Y. Xie, H.D. Yoo

Brown University, Providence, Rhode Island 02912, USA

A. Brandt, D. Brown, K. De, F. Jaafari, V. Kaushik, H. Kim, J. Li, M. Sosebee, B. Spurlock,
M.A. Strang, A. Vartapetian, A. White, J. Yu

University of Texas, Arlington, Texas 76019, USA

R. Kehoe, P. Renkel

Southern Methodist University, Dallas, Texas 75275, USA

P. Bargassa, M. Cooke, M. Corcoran, S.J. Lee, D. Mackin, H. Miettinen, P. Padley,

G. Pawloski

Rice University, Houston, Texas 77005, USA

R. Hirosky, A. Kryemadhi, K. Nelson

University of Virginia, Charlottesville, Virginia 22901, USA

T.H. Burnett, T. Gadfort, A. Garcia-Bellido, G. Gaudio, H.J. Lubatti, G. Watts, T. Zhao

University of Washington, Seattle, Washington 98195, USA

Appendix B

THE LEVEL 2 TRIGGER SYSTEM AND ALPHA BOARDS

Level 2 is an essential part of the DØ trigger and data acquisition system (70; 71; 72; 73). It was designed to provide a reduction in the event rate by a factor of 10 within a 100 μsec time window while inducing less than 5% deadtime. As outlined in Chapter 4.2 the L2 trigger system is organized as a two-stage *stochastic pipeline*. In the first step (*preprocessing stage*) subdetector based proto-objects are formed by preprocessors. The second step (*global processing*) combines the information provided by the preprocessors to make the event-wide L2 trigger decision. One advantage of this design is that each preprocessor is able to operate in parallel, independently from all other preprocessors. This avoids deadtime since decision times can vary significantly from event to event. Additionally up to 16 events can be queued in buffers (*FIFOs*) between the stages.

B.1 The Standard Level 2 Crate

All L2 systems occupy 9U[1] VME crates (74):

- Forward Muon Preprocessor (L2MUF)
- Central Muon Preprocessor (L2MUC)
- Calorimeter Preprocessor (L2CAL)

---

[1] 1U = 1.75 in

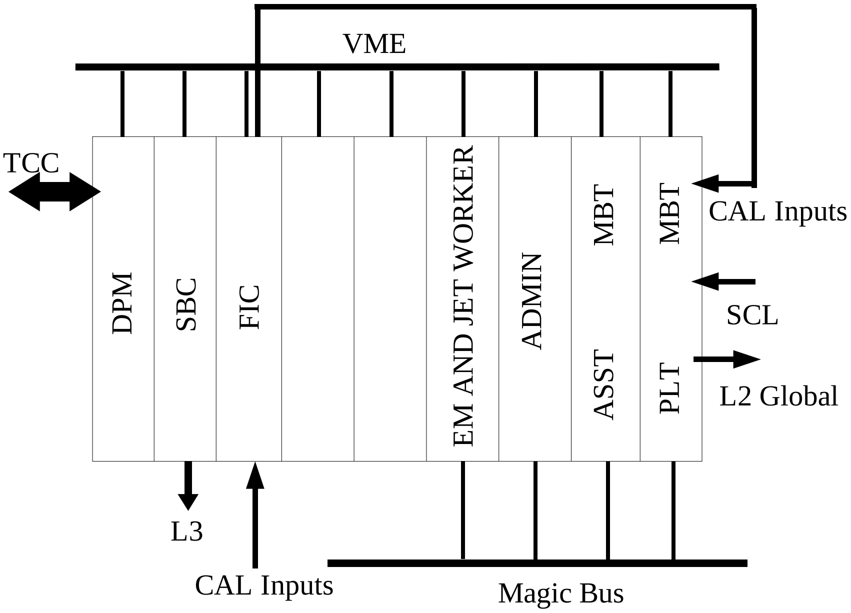

Figure 97. Layout of the Level 2 calorimeter (L2CAL) crate.

- Preshower Preprocessor (L2PS)
- Tracking Preprocessor (L2CTT/L2STT)
- Global Processor (L2GBL)

Each crate contains a 64-bit VME bus (75) and a custom-built high-speed bus (*Magic Bus*, or MBus) for data-handling on an auxiliary backplane (76). The 128 bit MBus supports data rates of up to 320 Mbit/s. Figure 97 shows a schematic view of the L2CAL crate with its main components:

DPM (*Dual Port Memory*): A DPM card is used as the VME crate controller. It downloads run-time parameters and reports monitoring data to the Trigger Control Computer (TCC[1]).

SBC (*Single Board Computer*): An SBC card is used to write data to the L3 system.

FIC (*Fiber Input Converter*): In some cases additional specialized hardware for data conversion and processing is added. In the case of the L2CAL crate, the L1 input signals arrive in the form of fiber-optic cables. A special converter card (FIC) translates optical GLink signals into electrical HotLink signals (77).

Workers/Administrator (*Alpha Board*): The Alpha Boards performed the main processing step within the L2 trigger system. Their main purpose was the application of the L2 trigger algorithms (*Worker*). They also handled additional event processing and local trigger control tasks (*Administrator*). Both Worker and Administrator functionality were implemented in a single Alpha Board. A detailed overview of the Alpha Board system architecture is given in Chapter B.2. The Alpha Boards were substituted by *Beta Boards* in September of 2003 (78).

MBT (*Magic Bus Transceiver*): The MBT cards (79) receive detector data and broadcast them to the Worker/Administrator via the MBus. After preprocessing is finished, the MBT sends the output signals via two HotLink output ports to the L2 Global Processor

---

[1] TCC handles run control, downloads run-specific information, and collects monitoring data.

(L2GBL). The MBT cards also receive information regarding L1 trigger accepts, L2 trigger decisions, and system-wide initializations (*Serial Command Link Initialize*, or SCLinit).

B.2 Level 2 Alpha Processors

The overall design of the Alpha Board (Figure 98) was based on the layout of the DEC [1] PC164 motherboard (80; 81). It featured a 500 MHz Alpha CPU running under real-time Linux. In addition to the internal PCI bus several elements supporting VME and MBus interfaces were added. Figure 99 shows a schematic view of the Alpha Board. The main components are described in the following.

B.2.1 PC164 Based Design

The Alpha Board used the first commercially available 64-bit RISC processor: a 500 MHz Alpha 21164 CPU (82; 83). It executed 2-4 instructions per cycle. The 500 MHz CPU frequency was generated by a 50 MHz oscillator by means of a divide-by-10 phase-locked loop circuit.

The Alpha Board had several caches implemented, both on-chip (integrated into the CPU) and external. 8 kB data and instruction caches (Dcache and Icache, respectively) buffered the most frequently used data and instructions to speed up processing. A secondary on-chip 96 kB mixed data and instruction cache (Scache) was also used. A third level of external cache (4 MB) was not utilized.

An interface between the CPU, main memory, and the PCI bus was provided by the 21172 Core Logic Chipset (Figure 100, (84)). The 21172 Chipset consisted of the 21172-CA chip (CIA)

---

[1] Digital Equipment Corp. merged with Compaq Computer Corp. in 1998.

Figure 98. Level 2 Alpha Board with Ethernet card and hard disk drive.

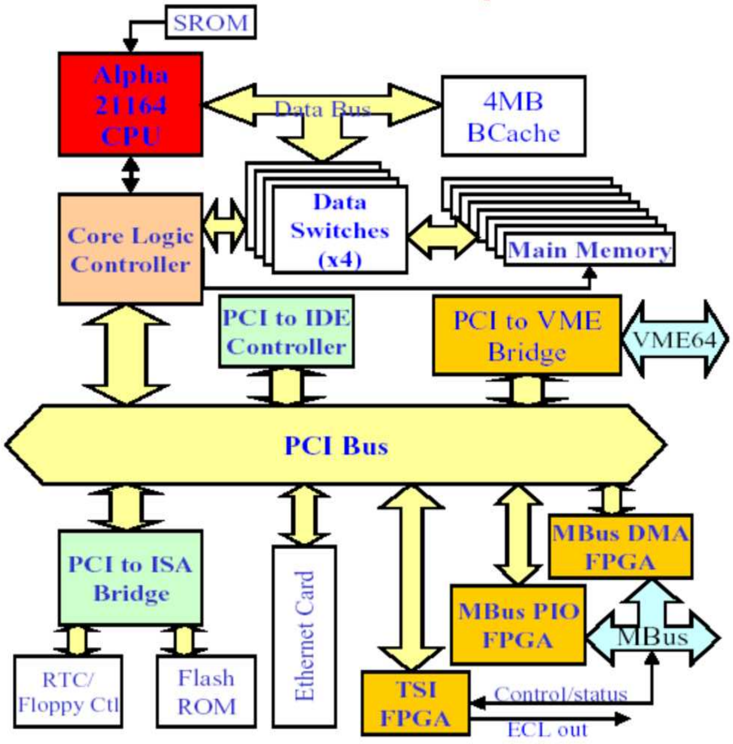

Figure 99. Block diagram of Level 2 Alpha Board.

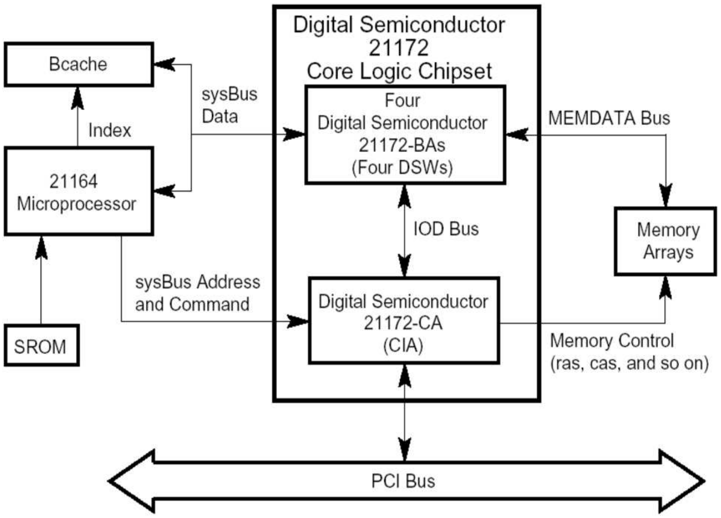

Figure 100. Block diagram of the 21172 Core Logic Chipset.

which provided the interface between the CPU and the PCI bus. It also provided main memory controlling and addressing capabilities. A set of four data switching chips (DSW) functioned as a multiplexing/demultiplexing device for main memory access. The 21172 Chipset provided data transfer rates of up to 267 MB/s (64-bit at 30 ns/cycle).

The Alpha Board carried two kinds of firmware for initial configuration. A 128 kB SROM chip was directly connected to the Icache. It contained the boot code that was loaded into the CPU at power-up, including the initialization of the PCI bus, the setting of registers in the CIA, the setting up of the various caches and memory, and finally the copying of the contents of the Flash ROM to memory. The 1 MB Flash ROM chip contained OS and task specific instructions. This included instructions to download user code via a PCI Ethernet card, a rudimentary local debugger ("Debug Monitor"), and the server for a remote debugger. The SROM chip was installed in a socket, and could therefore be programmed by using an external device programmer. The Flash ROM chip was soldered to the board, and had to be programmed in situ.

A bank of eight SIMM slots provided 128 MB of DRAM memory.

The 64-bit 33 MHz PCI bus had two expansion slots. A standard PCI Ethernet card connected to one of the PCI slots was used for remote access. Two programmable chips (PLDs) were used for PCI interrupt handling and bus arbitration.

A PCI-IDE interface chip connected a 6 GB IDE hard disk drive, which had real-time Linux installed.

A PCI-ISA bridge provided support for external devices such as a mouse, keyboard, and floppy drive. It also supported a parallel port, two serial ports, and a real time clock. The ISA bus was used to access the Flash ROM.

B.2.2 Magic Bus Programmed Input/Output

An interface between MBus and PCI bus was provided by the Magic Bus Programmed I/O chip (MBusPIO). It read and wrote data between the two address spaces and thereby provided a way of communication between different cards that were connected to the MBus. For example, a board connected to the MBus could write or read into Alpha Board memory. A programmable Xilinx XC4036EX chip (MAGICFPGA) was used for this task.

B.2.3 Magic Bus Direct Memory Access Interface

In order to boost processing time, data were transferred to and from Alpha Board memory by direct memory access (DMA), i.e. data on the MBus went directly to Alpha Board memory without involving the CPU. This *DMA engine* was implemented in two programmable chips: a Xilinx FPGA, and a Cypress CPLD.

B.2.4 VME Interface

A 64-bit PCI-VME interface was provided by the Tundra Universe II chip by mapping "windows" of VME address space to Alpha Board memory space (85).

B.2.5 TSI Interface

The TSI interface was used to receive and send additional information to the trigger system. Is was also used to monitor the state of the Alpha Board processing elements.

CITED LITERATURE

1. Arnison, G. et al.: Experimental observation of lepton pairs of invariant mass around 95 GeV/c2 at the CERN SPS collider. Phys. Lett., 126B:398, 1983.

2. Bagnaia, P.: Evidence for Z(e+e-) at the CERN ppbar collider. Phys. Lett., 129B:130, 1983.

3. Veltman, M.: Facts and Mysteries in Elementary Particle Physics. World Scientific, 2003.

4. Griffiths, D.: Introduction to Elementary Particles. John Wiley & Sons, 1987.

5. Halzen, F. and Martin, A.: Quarks and Leptons. John Wiley & Sons, 1984.

6. Quigg, C.: Gauge Theories of the Strong, Weak, and Electromagnetic Interactions. Westview Press, 1983.

7. Ellis, R. et al.: QCD and Collider Physics. Cambridge University Press, 1996.

8. Prosper, H. and Danilov, M.: Techniques and Concepts of High-Energy Physics XII. NATO Science Series, 2003.

9. Eidelman, S. et al.: Review of Particle Physics. Phys. Lett. B, 592:1, 2004.

10. Altarelli, G. and Parisi, G.: Asymptotic freedom in parton language. Nucl. Phys. B, 126:298, 1977.

11. Gribov, V. and Lipatov, L.: . Sov. J. Nucl. Phys., 15:438, 1972.

12. Dokshitzer, Y.: . Sov. J. Phys. JETP, 46:641, 1977.

13. CTEQ: CTEQ5 Parton Distributions. Eur.Phys.J., C12:375–392, 2000.

14. Carena, M. et al.: Report of the Tevatron Higgs Working Group. hep-ph/0010338, 2000.

15. Babukhadia, L. et al.: Results of the Higgs Tevatron Sensitivity Study. FERMILAB-PUB-03/320-E, 2003.

16. CDF: Properties of Jets in Z Boson Events from 1.8 TeV ppbar Collisions. Physical Review Letters, 77:448, 1996.

17. Thompson, J.: Introduction to Colliding Beams at Fermilab. FERMILAB-TM-1909, 1994.

18. General Reference Documents for Accelerators. 2002.
http://www-numi.fnal.gov/workgrps/protonwg/accel_reference.html.

19. Accelerator Concepts Rookie Books. 2003.
http://www-bdnew.fnal.gov/operations/rookie_books/rbooks.html.

20. Edmunds, D.: Run IIa Tevatron Beam Structure.
http://www.pa.msu.edu/hep/d0/ftp/l1/framework/drawings/run_iia_beam_structure.ps.

21. Edwards, T. et al.: Determination of the Effective Inelastic p anti-p Cross Section for the D0 Run II Luminosity Measurement. FERMILAB-TM-2278-E, 2004.

22. Begel, M. et al.: D0 Luminosity in Run 2: Delivered. D0 Note 3970, 2002.

23. Ferbel, T.: A Brief Description of the D0 Detector in Run II. 2004.
http://www-d0.fnal.gov/Run2Physics/WWW/templates/detector.tex.

24. Abachi, S. et al.: The D0 Detector. Nucl. Instrum. Methods Phys. Res. A, 338:185, 1994.

25. D0 Collaboration: D0 Silicon Tracker Technical Design Report. 1994.
http://d0server1.fnal.gov/projects/silicon/www/tdr_final.ps.

26. D0 Collaboration: The D0 Upgrade: Central Tracker Technical Design Report. 1999.
http://d0server1.fnal.gov/users/stefan/www/CFT_TDR/CFT_TDR.ps.

27. Adams, M. et al.: Design Report of the Central Preshower Detector for the D0 Upgrade. 1996.
http://d0server1.fnal.gov/users/qianj/CPS/doc/dn3104.pdf.

28. Gordeev, A. et al.: Technical Design Report of the Forward Preshower Detector for the D0 Upgrade. D0 Note 3445, 1998.

29. Snyder, S.: Measurement of the Top Quark Mass at D0. Stony Brook University, 1995.

30. Baldin, B. et al.: Technical Design Report of the Central Muon System. D0 Note 3365, 1997.

31. Alexeev, G. et al.: Technical Design Report of the D0 Forward Muon Tracking Detector Based on Mini-Drift Tubes. D0 Note 3366, 1997.

32. Yurkewicz, A.: Search for Evidence of Supersymmetry in the Like-sign Dimuon Channel at the D0 Experiment. Michigan State University, 2004.

33. Blazey, J.: The D0 Run II Trigger. http://niuhep.physics.niu.edu/˜blazey/rt.ps.

34. D0 Collaboration: d0reco. 2004. http://wwwd0.fnal.gov/Run2Physics/WWW/algorithm.htm.

35. Borisov, G.: Ordering a Chaos... or Technical Details of AA Tracking. 2004. http://www-d0.fnal.gov/global_tracking/talks/20030228/talk-adm-030228.ps.

36. Khanov, A.: HTF: Histogramming Method for Finding Tracks. D0 Note 3778, 2000.

37. Haas, A.: A Search for Neutral Higgs Bosons at High tanβ in Multi-jet Events from $p\bar{p}$ Collisions at $\sqrt{s} = 1960$ GeV. University of Washington, 2004.

38. Schwartzman, A. and Narain, M.: Probabilistic Primary Vertex Selection. D0 Note 4042, 2002.

39. Melnitchouk, A.: Search for non-SM Light Higgs Boson in the $h \rightarrow \gamma\gamma$ Channel. Brown University, 2004.

40. Blazey et al.: Run II Jet Physics. hep-ex/0005012, 2000.

41. Busato, E. and Andrieu, B.: Jet Algorithms in the D0 Run II Software: Description and User's Guide. D0 Note 4457, 2004.

42. Agram, J.-L. et al.: Jet Energy Scale at D0 Run II. D0 Note 4720, 2005.

43. Mrenna, S.: Event Generators. http://www.phys.psu.edu/˜cteq/schools/summer04/mrenna/mrenna.pdf.

44. Baer, H. et al.: Les Houches Guidebook to Monte Carlo Generators for Hadron Collider Physics. hep-ph/0403045, 2004.

45. Sjoestrand, T. et al.: PYTHIA 6.3 Physics and Manual. hep-ph/0308153, 2003.

46. Mangano, M.: Higher-order QCD processes via LO matrix-element MC's. http://www.wlap.org/file-archive/atlas/20040622-umwlap002-02-mangano.pdf.

47. Mangano, M.: Merging multijet matrix elements and shower evolution in hadronic collisions. http://mlm.home.cern.ch/mlm/talks/lund-alpgen.pdf.

48. Michelangelo, L. et al.: A Generator for Hard Multiparton Processes in Hadronic Collisions. hep-ph/0206293, 2002.

49. Mangano, M.: ALPGEN V1.3. http://mlm.home.cern.ch/mlm/alpgen/.

50. Maltoni, F.: Madevent: Automatic Event Generation with MADGRAPH. hep-ph/0208156, 2002.

51. Mrenna, S.: Mrenna Matched Datasets. http://cepa.fnal.gov/personal/mrenna/Matched_Dataset_Description.html.

52. Mrenna, S. and Richardson, P.: Matching matrix elements and parton showers with HERWIG and PYTHIA. JHEP05(2004)040, 2004.

53. Catani, S. et al.: QCD matix elements + parton showers. JHEP11(2001)063, 2001.

54. Private Communication with Suyong Choi (suyong@fnal.gov) and http://mcfm.fnal.gov/.

55. Ellis, K.: A critical review of vector boson + jets Monte Carlos. http://www-cdf.fnal.gov/Tevatron-Connection/QCD_Theory_Keith.pdf.

56. Ellis, K.: Method 2 at NLO. hep-ph/0405276, 2004.

57. Fisyak, Y. and Womersley, J.: D0 GEANT Simulation of the Total Apparatus Response. D0 Note 3191, 1997.

58. CERN: GEANT - Detector Description and Simulation Tool. 1993.

59. Bassler, U. et al.: Technical Description of the T42 Algorithm for the Calorimeter Noise Suppression. D0 Note 4146, 2003.

60. Choi, S. et al.: ATHENA Root Tuple Maker.
http://www-d0.fnal.gov/˜suyong/d0_private/athenaweb/athena.htm.

61. Stone, A.: Bad Runs.
http://www-clued0.fnal.gov/˜alstone/D0Work/Athena/badruns/badruns.html.

62. Verzocchi, M.: Inclusive Single EM Triggers for W/Z Analyses.
http://www-d0.fnal.gov/Run2Physics/wz/d0private/triggers/EMtriggers.html.

63. Jain, S.: Scale and Over-smearing for MC Electron. D0 Note 4402, 2004.

64. Top Physics Working Group: D0 Top Analyses and Data Sample for the Winter Conferences 2004. D0 Note 4419, 2004.

65. Chapin, D. et al.: Measurement of the $Z \rightarrow e^+e^-$ and $W \rightarrow e^\pm\nu$ Production Cross Sections with $|\eta| < 1.05$. 2005.
http://www-d0.fnal.gov/˜gardnerj/wzcross_v3.2.pdf.

66. Private Communication with Paul Telford (ptelford@fnal.gov).

67. CDF Collaboration: First Measurement of Inclusive W and Z Cross Sections from Run II of the Tevatron Collider. Phys. Rev. Lett., 94:091803, 2005.
http://www-cdf.fnal.gov/physics/preprints/index.html.

68. Heinmiller, J. and Varelas, N.: Jet Reconstruction Efficiency. D0 Note 4837, 2005.

69. Private Communication with Mathieu Agelou (agelou@fnal.gov).

70. L2 Trigger Group: L2 Web Page. 2004.
http://www.pa.msu.edu/hep/d0/l2/.

71. UIC L2 Trigger Group: L2 Alpha Board Information. 2003.
http://www-d0online.fnal.gov/www/groups/trigger/l2/online/uic_alpha/.

72. Adams, M. et al.: Level-2 Calorimeter Preprocessor Technical Design Report. D0 Note 3651, 1999.

73. Edmunds, D. et al.: Technical Design Report for the L2 Global Processor. D0 Note 3402, 1998.

74. Linnemann, J.: The Standard L2 Crate. 1999.
http://www.pa.msu.edu/hep/d0/ftp/l2/overview/l2_standard_crate.pdf.

75. VITA: VME64 Extensions for Physics and other Application. 1997.
http://galileo.phys.virginia.edu/~rjh2j/l2beta/vme/vita23d13a.pdf.

76. Baden, D. et al.: D0 Level 2 Magic Bus. 2004.
http://galileo.phys.virginia.edu/~rjh2j/l2beta/beta_docs/d0_magicbus.pdf.

77. Linnemann, J.: FIC Card - Fiber Input Converter.
http://www.pa.msu.edu/hep/d0/l2/fic.htm.

78. Hirosky, R.: The L2 Beta Project.
http://galileo.phys.virginia.edu/~rjh2j/l2beta/home.html.

79. University of Maryland D0 Level 2 Group: A Home page for the MagicBus Transceiver card.
http://www-d0online.fnal.gov/www/groups/trigger/l2/cards/MBT/index.html.

80. Miller, S. et al.: Level 2 Processor Board Technical Reference Manual. 1998.
http://galileo.phys.virginia.edu/~rjh2j/l2beta/alpha_docs/alphaboard_technical.pdf.

81. DEC: Digital Semiconducor AlphaPC 164 Motherboard. 1997.
http://www-d0online.fnal.gov/www/groups/trigger/l2/online/uic_alpha/l2alpha/.

82. DEC: Digital Semiconducor 21164 Alpha Microprocessor Hardware Reference Manual. 1997.
http://www-d0online.fnal.gov/www/groups/trigger/l2/online/uic_alpha/l2alpha/.

83. Compaq: Alpha Architecture Handbook. 1998.
http://www-d0online.fnal.gov/www/groups/trigger/l2/online/uic_alpha/l2alpha/.

84. DEC: Digital Semiconducor 21172 Core Logic Chipset Technical Reference Manual. 1996.
http://www-d0online.fnal.gov/www/groups/trigger/l2/online/uic_alpha/l2alpha/.

85. Tundra: Universe II User Manual. 1998.
http://www-d0online.fnal.gov/www/groups/trigger/l2/online/uic_alpha/l2alpha/.

VITA

In 1992, Marc Buehler earned a B.S. in Astronomy from the University of Basel, Switzerland.

In 1997 he received a M.S. in Physics from the University of Heidelberg Germany.

He was accepted into the graduate physics program at the University of Illinois at Chicago, USA 1997. Under the direction of Prof. Nikos Varelas, he received the degree of Doctor of Philosophy in Physics in 2005.